8-2023

Evaluating the Feasibility of Using Strain Measured During Sinusoidal Rate Pumping Tests to Characterize an Aquifer

Riley Blais
rblais@g.clemson.edu

EVALUATING THE FEASIBILITY OF USING STRAIN MEASURED DURING SINUSOIDAL RATE PUMPING TESTS TO CHARACTERIZE AN AQUIFER

A Thesis
Presented to
the Graduate School of
Clemson University

In Partial Fulfillment
of the Requirements for the Degree
Master of Science
Hydrogeology

---

by
Riley L. Blais
August 2023

Accepted by:
Dr. Lawrence Murdoch, Committee Chair
Dr. Scott DeWolf
Dr. Ronald Falta

ABSTRACT

Pumping tests with sinusoidal variation in pumping rate have been proposed as a method for improving aquifer characterization. These tests can interrogate a larger aquifer volume than slug tests and they can be more sensitive to small variations in drawdown. Current methods of using sinusoidal variations of rate are based on measuring pressure signals from the reservoir or aquifer, which requires access to monitoring wells. An alternative approach has been developed that measures the strain in the vadose zone instead of pressure in the reservoir. An instrument has been developed at Clemson University that can measure small strains using optical fiber sensors, and we propose that it can be used to measure strain during sinusoidal pumping tests.

The objective of this project is to evaluate the feasibility of measuring and interpreting the vertical strain in the vadose zone generated during a sinusoidal rate pumping tests to estimate aquifer and/or overburden properties. Pumping tests were performed at a site with a water table at 9 m and saturated saprolite from 9 to 30m depth. Sinusoidal pumping tests in the saprolite used different pumping amplitudes and periods while pressure was measured at three piezometers and vertical strain was measured in the vadose zone from 1 to 7 m depth. The delay time of the pressure increased linearly with distance, and it increased with the square root of the period, while the amplitude of the pressure decreased with distance and increased with amplitude. Vertical strain in the vadose zone varied with the same period as the pumping rate and the delay times were similar to those for pressures measured at similar radial distances. Delay times for the

strain increased with an increasing propagation of the strain field. The hydraulic diffusivity was estimated using delay times for pressure and strain, and the results were compared with the values estimated from a constant-rate pumping test. The hydraulic diffusivity from the constant rate test was 0.039 m^2/sec, whereas it was 0.053 (±0.05) m^2/sec and 0.035 (±0.03) m^2/sec from the pressure data and 0.08 (±0.022) m^2/sec and 0.035 (±0.001) m^2/sec from the strain data from sinusoidal tests of various periods and amplitudes. There is no statistical difference among these values. This study indicates that strain measurements in the vadose zone can be used to estimate aquifer properties during sinusoidal pumping tests.

DEDICATION

This thesis is dedicated to my parents, Ricky and Cindy Blais, my sister, Mallory Blais, and my family and friends for their continued support. This work would not be possible without their sacrifice, guidance, and motivation to continue my education in pursuit of my masters in hydrogeology.

ACKNOWLEDGMENTS

I sincerely thank my advisor, Dr. Lawrence Murdoch, for giving me the opportunity to work on this research project and for providing me with guidance throughout my time at Clemson. I am grateful for the knowledge he has shared with me within the fields of geology and hydrogeology.

I would also like to thank my committee members, Dr. Scott DeWolf, and Dr. Ron Falta for the time they spent helping develop and implement various parts of this research and provide mentorship to me.

Additionally, this work could not have been performed without the help and support of Dr. Liwei Hua, Dr. Leonid Germanovich, and other Clemson master's students.

This work was funded by the National Energy Technology Laboratory Project FE0023292

TABLE OF CONTENTS

Table of Contents (Continued) Page

LIST OF TABLES

List of Tables (Continued)

Table Page

LIST OF FIGURES

List of Figures (Continued)

Figure Page

List of Figures (Continued)

Figure Page

List of Figures (Continued)

Figure Page

List of Figures (Continued)

Figure Page

List of Figures (Continued)

Figure Page

List of Figures (Continued)

Figure Page

CHAPTER ONE: INTRODUCTION

Determining aquifer properties is essential to understanding hydrogeologic processes affecting environmental systems. Estimates of aquifer properties are generally made using pressure data measured in response to a stress caused by injecting or removing water from a well. A forward model of the response to the stress is inverted by adjusting parameters to match the observed pressure data. This approach is widely used for site characterization to help develop ground water management strategies and assess contaminated sites.

Properties of porous media can also be estimated from laboratory data, but these measurements typically represent a scale that is significantly smaller than that important to pressure changes in aquifers (Butler and Healey, 1998). As a result, properties estimated from well tests are better suited for site characterization than results from lab tests. A wide variation of well tests have been proposed, with an equally wide range of advantages and disadvantages for various applications (Kruseman and de Ridder, 1994).

Slug Tests

Slug tests are performed by rapidly changing the hydraulic head in a well and then measuring the response as the pressure changes and returns to equilibrium. In most cases, the pressure is changed by displacing a volume of water by inserting or removing a solid cylinder or bailer from the wellbore (Cooper et al., 1967; Butler, 1997). Another approach involves changing the pressure by injecting or removing air from the headspace above the well. Injecting air increases the pressure in the water much the same as

displacing water by inserting a slug. After the sudden change of the hydraulic head in the well, the water level returns back to initial conditions, either rising or falling depending on the test (Butler, 1997). The change in fluid pressure created by the displacement of water in a well is measured and analyzed using mathematical models based on the configuration of the aquifer and well (Butler, 1997). A wide range of analytical solutions are available as forward models (Butler, 1997) and they facilitate the estimation of hydraulic conductivity and transmissivity. The small volume of water displaced during slug tests make them only weakly sensitive to specific storage, however.

Slug tests are rapid, require minimal equipment, and do not require a net removal of water (Malama et al., 2016; Butler, 1997). These characteristics mean that they are less expensive to conduct than other well tests. They can provide useful results in low hydraulic conductivity formations where other aquifer tests, such as constant-rate pumping tests, may be difficult to perform due to the low required flow rates required (Butler, 1997). The ability to perform a series of slug tests at a site can provide spatial resolution in both the horizontal and vertical scale that may be important for the circumstances of the investigation (Butler, 1997). Slug tests, however, are sensitive to near-well conditions. Wells can have well skins that will cause the hydraulic conductivity of the formation to be under-estimated (Butler and Healey, 1998). The construction of a well also plays a role in the accuracy of a slug test. Monitoring wells with small casing diameters or small screen openings may artificially lower the hydraulic conductivity estimates (Butler, 1997). The relatively small changes in head in the observation well limits the pressure propagation to nearby wells (Malama et al., 2016). As a result, slug

tests only provide estimates in the vicinity of the well being tested. To achieve greater spatial resolution, a large array of wells may be needed. Slug tests are primarily used to estimate only the hydraulic conductivity because they lack the sensitivity required to measure storage (Butler, 1997). Despite the limited characterizing abilities, slug tests are important in the planning of other larger scale aquifer tests like pumping tests.

Pumping Tests

A pumping test is a well testing method in which water is pumped from a well and the subsequent drawdown in the pumping well and local piezometers is measured (Kruseman and de Ridder, 1994). There are three main types of pumping tests, (1) constant discharge, (2) constant head, and (3) recovery (Ferris et al., 1962). In a constant discharge test, the flow rate out of the pumping well is held constant and the drawdown in the pumping well and piezometers varies with time. In the constant head test, the discharge from the well varies with time while the head in the pumping well is constant. A recovery test analyzes the water level response after the well stops pumping water.

Having an understanding of the basic aquifer conceptual model prior to testing allows the proper selection of the testing method as well as the use of groundwater flow equations to estimate the hydraulic characteristics of the aquifer (Kasich et al., 2018).

Other important aspects of a pumping test that need to be considered during selection of the test are the ideal pumping rate, the testing duration, and the mathematical method for parameter estimation. Upon completion of the pumping test, the hydraulic characteristics of transmissivity, hydraulic conductivity, and storativity (or specific yield) can be estimated by fitting data to an analytical solutions (Kruseman and de Ridder,

1994). One of the first analytical solutions for the drawdown at $r = r_1$ in the vicinity of a pumping well is from Theim [1906] (Equation 1.1).

The assumptions that need to be satisfied for this method are: (1) the aquifer is confined. (2) The aquifer has an infinite areal extent. (3) The aquifer is homogeneous, isotropic, and of uniform thickness. (4) Prior to pumping, the piezometric surface is essentially horizontal. (5) The aquifer is pumped at a constant discharge rate. (6) The well is fully penetrating and screened over the whole saturated thickness. (7) The water removed from storage is discharged instantaneously with decline of head. (8) The diameter of the well is small so the storage in the well can be neglected. (9) The system is at steady state conditions, or transient effects can be ignored (Kruseman and de Ridder 1994).

$$s_1 = \frac{Q}{2\pi T}\ln(\frac{r_2}{r_1}) + s_2 \qquad \text{(Equation 1.1)}$$

where:

Q= well discharge rate [L^3/T]

T= Transmissivity of the aquifer [L^2/T]

r_1 and r_2 = distances of piezometers from the pumping well [L]

s_2 = Steady state drawdown in piezometer at $r = r_2$ [L]

Many other solutions have been developed for estimating aquifer properties. The use of each solution depends on the assumptions needed to represent field conditions. An extensive collection of methods used to evaluate pumping test data along with the necessary assumptions has been published by the Ohio EPA (Kasich et al., 2018).

Pumping tests build upon some of the shortcomings of slug tests. Pumping tests use not only a pumping well but also rely on monitoring wells. This opens the door for the wide range of analytical solutions designed for different aquifer assumptions. Pumping tests can estimate transmissivity (T) and storage properties of an aquifer, and in some cases the analyses estimate the hydraulic diffusivity, which is the ratio of transmissivity (T) and storativity (S). The use of multiple observation wells in addition to the pumping well reduces the effects of a well skin and increases the spatial resolution pumping tests compared to slug tests. Because a larger volume of water can be displaced over a longer period of time, the radial effect from the pumping test will be greater than that of a slug test. Using multiple monitoring wells helps to overcome the effects of wellbore completion like well skin. Well efficiency can be calculated separately from aquifer properties by completing a well performance test (Kruseman and de Ridder, 1994). Well performance tests determine the well losses and aquifer losses during a pumping test. It provides limited information about the aquifer itself, but rather accounts for why the observed drawdown in the pumping well is greater than what it would be in absence of well skin (Jacob, 1947). The head loss can be described using

$$\Delta h_w(t) = B(r_w^*, t)Q + CQ^2 \qquad \text{(Equation 1.2)}$$

where

$\Delta h_w(t)$ = the drawdown in the pumping well [L]

t= time since the start of pumping [T]

B= time-dependent linear head-loss coefficient [T/L^2]

r_w^*= effective radius of the pumping well [L]

Q= well discharge rate [L^3/T]

C= the nonlinear well-loss coefficient [T^2/L^5].

One common assumption in the analyses of pumping tests is that the aquifer is of infinite radial extent. This is not the case when a recharge or a barrier boundary are in proximity to the well (Kruseman and de Ridder, 1994). Boundaries will cause a drawdown pattern that is different from what would be expected theoretically. For a barrier boundary, the drawdown between the pumping well and the barrier will be greater than expected. For a recharge boundary, the drawdown between the pumping well and the recharge zone will be less than expected. To analyze these types of geometries, different solutions have been solved for which allow estimates of hydraulic properties to be calculated for one or more recharge, or barrier boundaries (Dietz, 1943; Hantush, 1959; Ferris et al., 1962; Vandenberg, 1976; 1977; Kruseman and de Ridder, 1994).

One of the biggest drawbacks to a pumping test is that there is a net removal of water, and if the aquifer is contaminated, special care must be taken to collect and

dispose of the water (Kasich et al., 2018). Similarly to slug tests, a successful pumping test requires accurate well logs to understand and account for well depths and screened intervals of the pumping and monitoring wells. This is reinforced by the use of the different aquifer solutions and the specific assumptions used by each to give reasonable estimate of aquifer properties. While a pumping test can be performed with just the pumping well and one observation well, a larger array of piezometers can achieve higher spatial accuracy for the parameter estimates.

Natural Harmonic Stresses on Aquifers

There are various natural processes that impact the hydraulic head in an aquifer, which are different from designed well tests. These processes are earth tides, ocean tides, and barometric pressure loading (Van Der Kamp and Gale, 1983; Ferris, 1952; Hsieh and Bredehoeft 1987). Each of these three processes generates a loading stress on the aquifer matrix or the fluid within. This stress causes the water pressure in the aquifer to fluctuate. The fluctuation is observable in piezometers, and there have been many studies that have worked to use passive measurements of hydraulic head caused by these forces to characterize the hydraulic properties of aquifers (Jacob, 1940; Ferris, 1952).

Tides

The gravitational forces from the sun and moon are responsible for generating tides in the ocean and on land. These tides are manifested as the rise and fall of the water level in the ocean and as crustal deformation in the solid earth. Ocean tides vary in magnitude depending on factors such as configuration of coast lines and the depth of the ocean floor (Merritt, 2004). Sea level can vary by as much as 12 meters in a day as seen

at the Bay of Fundy in Canada, but tidal variation varies globally (NOAA, 2018). Earth tides occur under the same conditions as ocean tides, however the magnitude of the change between the high and low tides is much less. Earth tides require sensitive instruments, such as tiltmeters, to measure the resulting deformation. The tides experienced by the earth have been extensively studied and include both diurnal and semidiurnal fluctuations. The fundamental tidal frequencies are generated that govern the tidal forces are shown in Table 1.1.

Table 1.1: Fundamental characteristics of tides, from Agnew (2007).

	Frequency (cycles/day)	Period	Cycle Name
1	0.9661368	24h 50m 28.3s	Lunar Day
2	0.0366011	27.3261 d	Moons Longitude: Tropical Month
3	0.0027379	365.2422 d	Suns Longitude: Solar Year
4	0.0003095	8.847 yr	Lunar Perigee
5	0.0001471	18.613 yr	Lunar Node
6	0.0000001	20941 yr	Solar Perigee

Tidal signals are composed of many different frequencies with different amplitudes. The various components that make up any cyclical signal are called harmonics. Using a Fourier Transform on the series in Table 1.1, the amplitudes of the harmonics that make up each signal was calculated (Cartwright and Tayler, 1971). Preliminary investigations revealed a total of 505 harmonics for the tidal frequencies with some studies calculating up to 27,000 harmonics due to improved measuring and computational technologies (Cartwright and Tayler, 1971; Kudryavtsev, 2004). Of all the harmonics, there are 5 harmonic components that make up approximately 95% of the

tidal potential which are listed in Table 1.2 (Melchior and Toba, 1978; Hsieh and Bredehoeft, 1987; Merritt, 2004). Small amplitude harmonics are difficult to isolate from other lesser harmonics without a high level of uncertainty or very large data set (Merritt, 2004).

Table 1.2: Primary Tidal Harmonic Components (Melchior and Toba, 1978; Hsieh and Bredehoeft, 1987)

Name of Constituent	Angular Freq. (deg/ hour)	Period (hour)
O_1	13.943	25.819
K_1	15.041	23.934
N_2	28.440	12.658
M_2	28.984	12.421

Earth Tides

The tidal effect from the sun and moon cause the surface of the solid earth to rise and fall. This rising and falling is a result of expansion and contraction of the earth's solid matrix. The expansion and contraction of the matrix decreases and increases the pore pressure in an aquifer, which has been observed in the rise and fall of water levels in observation wells (Rojstaczer, 1988b; Hsieh and Bredehoeft, 1987; Van Der Kamp and Gale, 1983). The extent of the deformation depends on the matrix and aquifer skeleton compressibility, the Poisson's ratio, and the porosity of the formation (Rojstaczer and Agnew, 1989; Van Der Kamp and Gale, 1983).

Previous studies have aimed to determine the effects on aquifer properties and water level response using earth tides (Bredehoeft, 1967). It has been shown that the frequency of water level response in a well is the same as the frequency of the aquifer stress (Cooper et al. 1965). The largest amplitude of tidal dilation, M_2, can produce water

level fluctuations of 1-2 cm in observation wells (Bredehoeft, 1967). Knowing the frequency of the harmonic earth tide signals, and the water level fluctuations, the difference in real time of these signals can be observed and calculated as phase delay or lag. Once this time delay between the M_2 signal and the corresponding water level fluctuation is calculated, the transmissivity of the aquifer can be estimated using a range of values for storage. Phase shift is not sensitive to storativity so it is possible to estimate a transmissivity within a factor of 2-4 with storativity of several orders of magnitude (Hsieh and Bredehoeft, 1987). The transmissivity can be estimated by using plots of phase shift versus $\frac{T\tau}{r_c^2}$ and phase shift vs τ where τ is equal to the period of the observed signal and r_c is the radius of the casing of the well.

The benefits to using earth tides as a means for parameter estimation in aquifers is that the frequency of earth tides has been extensively studied. The current earth tide models are very accurate and quite sensitive (Agnew, 2007). Also, there is a clear measurable response between earth tides and water level in monitoring wells (Hsieh and Bredehoeft, 1987; Cutillo and Bredehoeft, 2011; Rojstaczer and Agnew, 1989; Merritt, 2004). Despite the potential that exists in this method, the shortcomings are that there is no control over the frequency at which the signal is generated. The test is limited to the natural frequencies, so data collection times need to be span many days to analyze results spanning multiple periods.

Ocean Tides and Groundwater

The gravitational forces from the sun and the moon cause the water level in the oceans to rise and fall. This raising and lowering of hydraulic head propagates into

aquifers located both beneath the ocean and inland (Merritt, 2004). In unconfined aquifers, the water level fluctuations are a result of the movement of water via high and low head, and for confined aquifers the observed head change is a result of loading and unloading of the confining matrix (Ferris et al., 1962). As the tide rises, there is an increase in pressure head for the unconfined system, and for confined systems, the rising tide increases the stress on the aquifer skeleton (Ferris et al., 1962). The sinusoidal effect of the tides propagates inland from the coast, with decreasing amplitude and increased lag time and the distance inland increases (Ferris, 1952).

Using ocean tides to estimate aquifer properties has been shown to be a viable method since the frequency of the ocean tides has been heavily studied and the water level response in coastal aquifers follows the same periodic signal that the tide stage shows (Ferris, 1952). The time delay between the tide stage and the water level head at the inland wells (Merritt, 2004) are the variables needed to estimate the transmissivity of the aquifer using (Ferris, 1952; 1962).

$$T = 0.60 t_o S \left(\frac{x}{t_1}\right)^2 \qquad \text{(Equation 1.3)}$$

where

t_o= period of the tide stage fluctuation [L]

t_1= lag time between tide stage and water level fluctuation [T]

x= Distance from coast to observation well [L]

S= Storage coefficient [unitless]

This solution works for confined aquifers and for unconfined aquifers/ aquifers with partially penetrating wells, if the conditions are met: (1) the observation wells are far enough from the coast to not be affected by the vertical components of flow and (2) the head fluctuations in the observation wells are a small fraction of the total thickness of the aquifer (Ferris et al., 1962).

Using ocean tides to estimate aquifer properties is helpful because they can be used over a much larger area than conventional pumping tests. In addition, they can be performed at a lower cost and under simpler logistics by using the tidal stage as the input force (Rotzoll et al., 2008). The drawbacks to using ocean tides and corresponding head fluctuations are similar to the drawbacks of earth tides. The test is also limited to the coast and the natural fluctuations of the tidal stage so it could take many days/ months of recording to get a complete data set to perform an analysis. In addition, the number of monitoring wells located in costal aquifers will affect the resolution of the results.

Barometric

Barometric loading of an aquifer occurs as pressure changes in the atmosphere (Van Der Kamp and Gale, 1983). This change occurs as semidiurnal and diurnal fluctuations attributed to solar heating (Hsieh and Bredehoeft, 1987), atmospheric tides and other effects. Harmonic patterns of barometric pressure can also be seen on the scale of days to weeks as large weather systems move over the land (Hsieh and Bredehoeft ,1987). At sea level, the average air pressure is 101,325 Pascals (Pa) and this air pressure will fluctuate daily by up to several hundred Pa. During extreme conditions, the barometric pressure can drop by more than 13,000 Pa as seen during Hurricane

Wilma, which was among the largest hurricanes over the Atlantic Ocean (Kantha, 2006). As barometric fluctuations occur, the total pressure exerted on the land surface changes. In shallow, permeable unconfined aquifers, this fluctuation may have little effect, as the force exerted on the water table surface and the groundwater will be similar. For a confined aquifer, the change in barometric pressure applies a load to the water in the observation well, as well as the confining unit. The pressure on the confining unit adds a stress to the aquifer skeleton and changes the pore pressure within the aquifer. There is a difference in the pressure applied to the free surface where the full extent of the atmospheric pressure is felt and on the pressure within the aquifer which is less than the total pressure. This pressure difference pushes the water out of an observation well and into the formation, and this causes the water level in the observation well to fall. This is why there is an inverse correlation between barometric pressure and hydraulic head (Jacob, 1940; Ferris et al., 1962).

The hydraulic head response to atmospheric loading depends on the fluid flow and elastic properties of the aquifer and its material (Rojstaczer, 1988a). The ratio between the observed head change and the measured barometric pressure is called barometric efficiency (BE).

$$BE = -\frac{\Delta h}{\Delta B} \qquad \text{(Equation 1.4)}$$

where

Δh= change hydraulic head in well during a specified time interval [L]

ΔB= change in the barometric pressure head over the same time interval as Δh [L]

The barometric efficiency is used as a correction factor to remove the effects of barometric pressure on water level during pumping tests (Kruseman and de Ridder, 1994). It also can be used to estimate the storage coefficients in an aquifer. The barometric efficiency is related to the loading efficiency using the equation:

$$LE = 1 - BE \qquad \text{(Equation 1.5)}$$

where

LE= Loading Efficiency

There are dimensionless relationships between the barometric efficiency and the time delay and between the barometric pressure signal and the observed response (Rojstaczer, 1988a). These relationships are also frequency dependent. The aquifer response is broken down by frequency (Rojstaczer, 1988a). For low frequencies, the aquifer response is independent of permeability and is dependent upon the diffusivities of the confining unit and the vadose zone. For the intermediate range of frequencies, the response is independent of the fluid flow properties and is dependent upon the elastic properties of the aquifer matrix. The high frequency response is independent of the diffusivities and the elasticity, and dependent on the permeability of the aquifer. The response at high frequencies is independent of confining layer and unsaturated zone diffusivity and is strongly dependent on aquifer permeability (Rojstaczer, 1988a).

Barometric fluctuations can be used to estimate aquifer properties. They are useful because barometric fluctuations occur spatially over a large scale and if there are sufficient wells, the response can be measured to reflect that scale. They can also be

performed at a lower cost as there is no anthropogenic input to generate the fluctuations in the aquifer. The drawbacks to using barometric pressure is that the fluctuations are less predictable than ocean tides or earth tides, so the frequency response and lag time of the responses are more difficult to evaluate. Also as with all the hydraulic tests, the number of monitoring wells located in the aquifer controls the resolution of the test.

Sinusoidal Pumping/ Injection

Sinusoidal pumping tests are a form of hydraulic testing in which the well is pumped at a sinusoidal rate, either with a net removal of water, or paired with injection to have no net removal of water. Sinusoidal pumping tests are also called harmonic well tests, oscillatory well tests, cyclic well tests, or periodic well tests (Sun et al., 2015; Cardiff and Barrash, 2015; Horne and Rosa, 1997; Mehnert et al., 1999). The test originated from the idea of pulse interference tests in the oil industry. The interference tests work just as constant rate pumping tests do, changing the fluid pressure in a reservoir to estimate reservoir properties. In industry, interference tests are performed by altering the rate of pumping during production or injection into a reservoir and measuring pressure changes at other observation wells (Johnson et al., 1966). The pulse test was introduced as an alternate interference test due to its limited interruption of production. It involves a sequence of pumping and shut in cycles, while measuring the pressure change at the pumping well and pressure response in surrounding wells. The pressure response data is in the time domain. The pulse testing method creates a cyclic pressure response, which can be separated from the background pressure (Johnson et al., 1966; Kuo, 1972). This idea was expanded to harmonic pulse testing that can be performed by either:

(a) sinusoidal variation of flow, or (b) periodic multiple rates (Kuo, 1972). The flow rate and pressure response for this test are recorded but the key defining feature is that the data is processed in the frequency domain (Fokker et al., 2018). By pumping/ injecting at a known frequency, the data can be processed in at a specific frequency. This helps to isolate the generated signal from possible background noise because of other production wells or other natural harmonic signals such as those mentioned above. The frequency domain analysis of the pressure response also allows the possibility of locating heterogeneities in the subsurface (Kuo, 1972). Using the frequency and subsequently the phase lag between the flow and the observed pressure, the *kh* value (the product of formation permeability, *k*, and reservoir thickness, *h*) and the skin factor can be estimated (Kuo, 1972).

The sinusoidal technique developed for the oil industry was adapted for hydrogeological applications (Black and Kipp, 1981). Solutions were generated for a confined, non-leaky aquifer with both a point source and a line source. The analytical solution by Black and Kipp uses the ratio of the phase shift or amplitude between two different observation wells in order to estimate the hydraulic diffusivity. They did not provide a way to separate the hydraulic conductivity/ transmissivity and the storage components. New solutions have been derived that allow both diffusivity and transmissivity to be estimated (Rasmussen et al., 2003a).

The pumping flow rate can be described as

$$Q(t) = Q_1 \cos(\omega t) + Q_{ave} \quad \text{(Equation 1.6)}$$

where:

ω = the angular frequency of pumping [1/T]

Q = well discharge rate [L^3/T]

t = time [T]

The variables Q(t) (measured flow rate), ω, and t are known, and Q_1 and Q_{ave} are solved for by using the least-squares method. The pressure responses measured in observation wells are modeled using the same equation, modified using drawdown instead of volumetric flow rate.

$$s(t) = s_1 \cos(\omega t) + s_2 \sin(\omega t) \quad \text{(Equation 1.7)}$$

These two solutions are then related to each other to generate unit drawdown amplitudes per pumping amplitude and unit phase lags between observed drawdown and the flow rate (Rasmussen et al., 2003b).

$$s_o = \frac{|s|}{|Q|} = \frac{\sqrt{s_1^2 + s_2^2}}{\sqrt{Q_1^2 + Q_2^2}} \quad \text{(Equation 1.8)}$$

$$\varphi_o = \varphi_s - \varphi_Q = atan\frac{s_2}{s_1} - atan\frac{Q_2}{Q_1} \quad \text{(Equation 1.9)}$$

where:

φ_s= the phase of the observed drawdown

φ_Q= the phase of the flow rate

Once phase lag (φ_o) is calculated, the relationship:

$$\varphi_o = F(u) = arg\{K_o(\sqrt{iu})\} \quad \text{(Equation 1.10)}$$

where:

K_o = the zero-order modified Bessel function of the second kind

can be solved through inversion to find u. Solving for u allows the aquifer diffusivity (D) and transmissivity (T) to be estimated using:

$$D = \frac{\omega r^2}{u} \quad \text{(Equation 1.11)}$$

$$T = \frac{\left|K_o(\sqrt{iu})\right|}{2\pi s_o} \quad \text{(Equation 1.12)}$$

where:

r= radial distance from the pumping well [L]

Sinusoidal tests can be performed in several ways. One method is to have no net removal of water. This method uses both pumping (positive flow value) and injection (negative flow value).

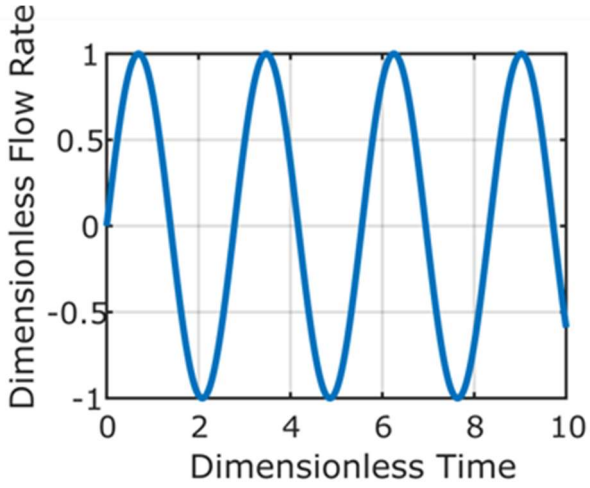

Figure 1.1: Example pumping rate during a sinusoidal pumping test with zero net pumping rate (a mean rate of 0).

Another example of a sinusoidal test is one where there is constant removal of water, with the rate fluctuating sinusoidally (Figure 1.2).

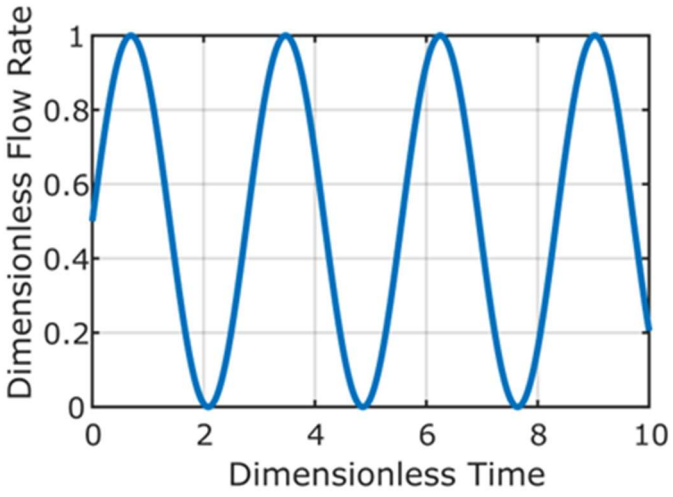

Figure 1.2: Example pumping rate during a sinusoidal pumping test with a net average rate of 0.5.

One benefit of sinusoidal pumping tests is that they can be effective down to low signal to noise ratios of hydraulic heads in monitoring wells. This is because frequency domain can be used to identify the phase lag, which is then used in (Equation 1.9). This also helps to separate the pumping signal from the naturally occurring harmonic signals. By pumping at a unique frequency separate from the known natural frequencies, the signal response observed will be independent from the other harmonics. Since sinusoidal pumping tests are analyzed in the frequency domain, the well can be continuously pumped, and measurements can start at any time during a period (although only intervals that include full periods can be analyzed). If pumping in a contaminated aquifer, under the no net removal of water test, contaminated water does not need to be transported to a waste site, they can be reinjected into the ground. A limitation of a sinusoidal pumping test is that it is hard to generate a true sinusoidal pumping rate. Just as with conventional pumping tests, the resolution of the test depends on the number and the spacing of observation wells in addition to the pumping well.

Strain

Some hydromechanical techniques use strain to characterize deformation of the subsurface. Strain is a tensor, which means it has six components. For this thesis, the vertical component of strain is the one that will be focused on. Strain can be measured, and it can be used to relate the deformation to the applied stress on a material. Strain (ϵ) is a unitless variable that is a measure of change in length compared to a reference length.

$$\varepsilon = \frac{\Delta L}{L} \qquad \text{(Equation 1.13)}$$

Strain is considered positive (+) when the body is in tension. Strain is considered negative (-) when the body is undergoing compression. For aquifers and their overburden, this tension and compression can be observed because of well testing, well pumping/injection for production purposes, and loading of the overburden. One observable example of this compression is during heavy pumping of aquifers when there is corresponding subsidence. Enough water is withdrawn from the aquifer to cause permanent deformation. As the water is removed from an aquifer the pore pressure decreases. As the pore pressure decreases, there is less support within the matrix so the effective stress increases and the matrix compresses (Davis et al., 1969). This creates tension in the overburden which can be measured as positive strain.

Vertical strain can be measured using extensometers. Extensometers measure the change in distance between a subsiding land surface and an anchor in the subsurface (Riley, 1987). Numerous extensometers exist on the market, such as wire extensometers or Differential Variable Reluctance Transducers (DVRT) (Riley, 1987; Murdoch et al. 2015). Extensometer measurements for aquifer displacement and strain begin as a borehole is drilled into the subsurface. At the bottom of the borehole, an anchor is placed which couples the sensor to the ground material. This material can be consolidated/ unconsolidated sediments or rock. A second anchor is placed either at the ground surface to measure total displacement, or within the borehole at a known height above the first anchor (Davis et al., 1969). The displacement is measured between these two anchors, and if their spacing is known, the vertical strain can be calculated.

Strain has been used to characterize different aquifer properties such as storage coefficients, vertical hydraulic conductivities, and changes in moisture load (Cleveland et al., 1992; Robson and Banta, 1970; Murdoch et al. 2015). Extensometers can provide estimates of these properties using strain. The vertical strain is related to effective vertical stress using the equation (Wang, 2000):

$$\varepsilon_{zz} = \frac{1}{C_1 E}\left[\Delta\sigma_{zz} + \alpha_B \Delta p + \alpha_T \frac{1+v}{1-v} C_1 E \Delta T\right], \varepsilon_{xx} = \varepsilon_{yy} = 0 \quad \text{(Equation 1.14)}$$

$$C_1 = \frac{1-v}{(1+v)(1-2v)} \quad \text{(Equation 1.15)}$$

where:

E= Youngs Modulus

v= Poisson's Ratio

$\Delta\sigma_{zz}$= Change in elastic normal stress in the vertical direction

Δp= Change in the pore pressure

ΔT= Change in temperature

α_B= Biot-Willis coefficient

α_T= Coefficient of thermal expansion

With the stress, the matrix compressibility can be calculated and from the compressibility, the aquifer properties can be estimated.

Problem Statement

Sinusoidal variations in rate during hydraulic well tests can be used to characterize aquifer or reservoir properties. Current methods of using sinusoidal

variations in rate are based on pressure signals from the reservoir or aquifer, but this is limited by the availability of monitoring wells. It may be possible to measure strain at shallow depths caused by sinusoidal injection or pumping at depth. Theoretical analyses are encouraging, and recent technology developments suggest that it could be possible to measure the generated strain signal at shallow depths in the field. The preliminary work is promising, but this approach has never been evaluated in the field, so the feasibility of implementing it is under investigation.

Objective

The primary objective of this research is to test the feasibility of measuring and interpreting the strain signal in the vadose zone generated during a sinusoidal pumping test to estimate aquifer and/or overburden properties such as transmissivity, storativity, or fluid distribution.

Approach

The objective of the thesis was met by installing a fiber optic strain ribbon in a borehole and measuring strain during numerous different sinusoidal pumping tests. During each test the drawdown was measured in three piezometers and the strain was measured in one borehole. These data were then analyzed to calculate the time delay between the pumping rate and the observed corresponding aquifer/ matrix responses. This data was then used to estimate hydraulic diffusivity of the aquifer.

Organization of the Thesis

The thesis is organized into five chapters. Chapter One is an introduction to well testing and periodic effects on aquifers. Chapter Two provides an overview of the project

site and experiment set up. Chapter Three summarizes the results obtained over the course of the experiments. Chapter Four describes the results and how they can be used to estimate aquifer properties. Chapter Five provides a conclusion of the findings.

CHAPTER TWO: METHODS

The principal activities of this research were to install a new optical fiber strain sensor and evaluate performance during sinusoidal pumping tests. This required developing equipment and techniques for packaging and deploying an optical fiber sensor, and for pumping water from a well at a precisely controlled variable rate and measuring the flow rate from the pump and the pressures in nearby monitoring wells.

Numerical and field experiments were performed to test the viability of using a fiber optic strain ribbon and interpreting the strain signal measured in the vadose zone during sinusoidal-rate pumping to estimate aquifer properties.

Equipment

The equipment developed for this investigation consists of a system to pump water from a well at variable rate, and a sensor system to measure strain during pumping.

Pumping System

A system was developed to pump water from a well at a variable rate. The system uses a Berkeley JP Composite Series downhole pump model B5P4JP05231 with a downhole check valve (Figure 2.1). The pump is 4-inch in diameter and was installed in the well at a depth of 75 feet below ground surface.

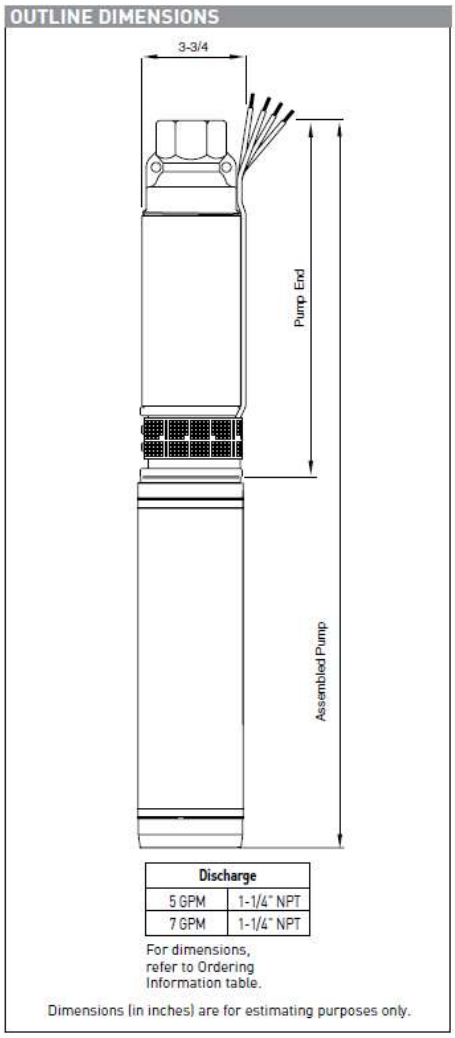

Figure 2.1: Berkeley pump schematic

The pump motor is powered by 220 VAC and rate of the pump is controlled by altering the frequency of the AC power using a variable frequency drive (VFD). The system uses an ATO model GK3000 VFD, which is designed for ½ horsepower, single-phase 220 VAC power. A 1000W step-up transformer (SEYAS AT-1000) was used to convert the 120V power available at the field site to 220V. The output of the VFD is controlled by a DC input voltage generated with a Tektronix AFG1022 Arbitrary

Function Generator. The function generator was configured to create a 0-5 volt sinusoidal signal with adjustable amplitude and period. The sinusoidal voltage generated by the function generator is converted to a variable frequency by the VFD, which in turn results in a flow rate at the downhole pump that varies as a sinusoidal function of time.

Flow rate was measured using a paddlewheel-type flow meter (Omega Engineering FP-5600) in the discharge hose from the downhole pump (Figure 2.2). The flow meter has a flow velocity range of 0.3 to 20 feet per second with an accuracy of ±1%. The flow meter was mounted in a ¾-inch Schedule 80 PVC pipe, which resulted measurable flow rates from 0.5 gallons per minute (gpm) to 34 gpm. The output of the flow meter was an amplified square voltage pulse. The pulse was converted to a flow rate using a conversion factor for a ¾-inch Schedule 80 PVC pipe, which is 583.19 pulse/gal, according to the manufacturer calibration specs. The calibration factor was verified in the field.

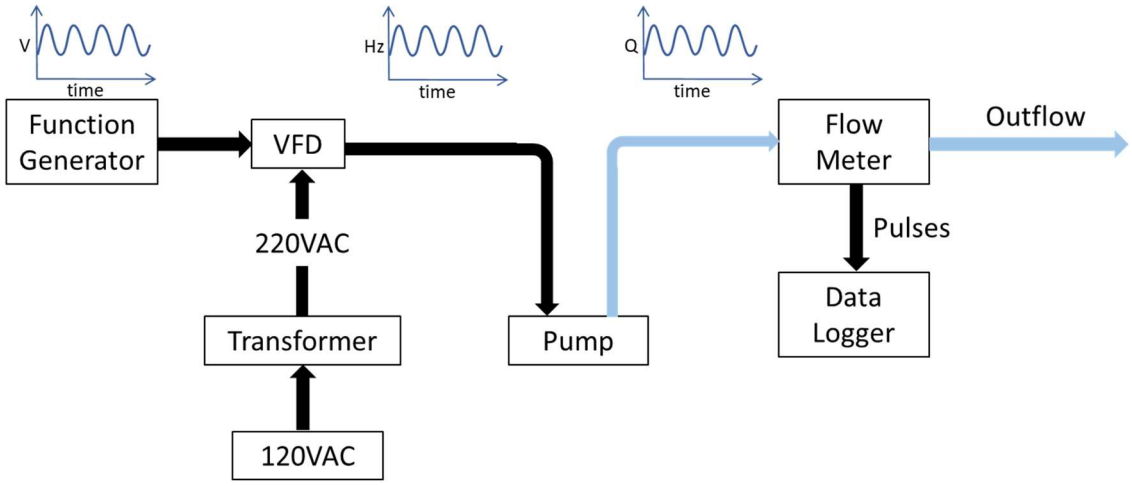

Figure 2.2: Schematic of the pumping system for flow rate control.

Strain measurements using CMPI

Strain in the subsurface was measured using a method called Coherence-length-gated Microwave Photonics Interferometry (CMPI), which was developed at Clemson University (Hua et al., 2017). The method measures strain along a single-mode optical fiber with internal broadband reflectors. Prior to this project, applications of CMPI to field settings were limited, so methods for deploying sensors in the field were unavailable. As a result, this project included a task to design and package optical fiber sensors used by CMPI for field deployment.

Coherence-length-gated Microwave Interferometry

The Coherence-length-gated Microwave Interferometry (CMPI) method measures the displacement between pairs of weak reflectors along an optical fiber using an electronic interrogator and Michelson interferometer reference. The system uses microwave modulated low coherence light as the probe, which is injected into the sensing fiber. The backscattering from the weak reflectors is recorded in the microwave frequency domain through down conversion. The microwave spectrum is further processed to obtain the distributed strain signals.

The CMPI methods use communication-grade, 250-micron-diameter, single-mode optical fiber with an acrylate coating and a glass core 9 microns in diameter. Reflectors are fabricated by focusing the beam of a femtosecond laser onto the core of the fiber. This modifies the refractive index over a small region within the core, which is designed to create an imperfection that reflects approximately -35 to -45 dB of light. Each reflector returns a small fraction of the light from the laser, so many reflectors can be used before

the outgoing signal strength is diminished. However, the strength of the reflection is much greater than the reflections from Raleigh scattering, which increases the signal to noise ratio compared to measurement methods that use Raleigh scattering (e.g. Distributed Acoustic Sensing).

CMPI is implemented using an interrogator and reference interferometer. The interrogator includes a microwave source and detector, a laser, an electro-optic modulator, and a photodetector (PD). The light from the laser source is intensity-modulated by a microwave signal using an electro-optic modulator (EOM). The modulated light is launched into the sensing fiber, and the reflections are detected by the PD. The demodulated signal is received by the microwave detector, which measures the amplitude and phase of the signal at the modulation frequency. After the microwave source sweeps through the designated microwave bandwidth, the S_{21} spectrum is obtained, which is used to read the sensing signal. The resulting data are processed to determine the strain using methods described in (Hua et al. 2017, 1-4; Hua et al. 2020, 1-9).

An external optical fiber Michelson Interferometer (MI) with arm length difference of 15 cm is used as a reference. The MI is sealed in a metal tube and suspended in a borehole (Figure 2.3) to minimize the optical path difference (OPD) change. The deformation experienced by the sensing fiber is independent of the reference fiber, so the MI acts as a stable reference.

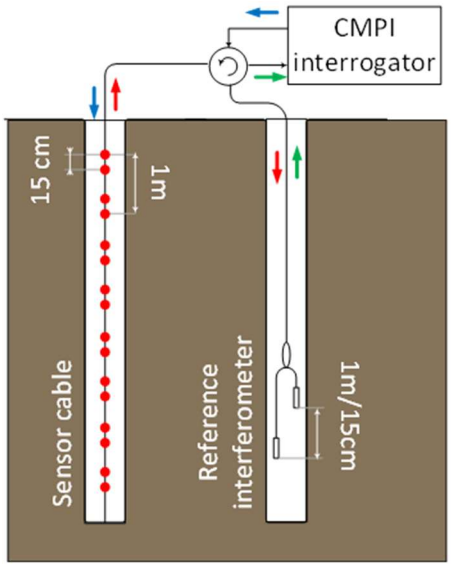

Figure 2.3: Conceptual model cross section of the sensor cable and reference interferometer in the field

Strain Ribbon

The tensile strength of the 250-micron diameter optical fiber used to measure strain with CMPI is approximately 100kpsi (0.69 GPa), which is strong enough to limit breakage during careful handling in the lab, but it is too weak for field applications. This problem occurs for all applications of optical fibers, and it has resulted in a variety of methods of packaging fiber into reinforced cable. Some reinforcement consists of a polymer coating, or buffer, that increases the diameter of the fiber to 900 microns. This produces tight-buffered optical fiber, which is stronger than the 250-micron-diameter fiber, but it remains too fragile for many field applications. Another cable design consists of multiple, tight-buffered fibers wrapped in braided Kevlar and coated in polymer. This is called "tactical" optical fiber cable. Tactical cable provides significant tensile and

bending strength and it can protect optical fiber during many routine field applications, including in the shallow subsurface. Optical fiber armored in stainless steel tubing is also available to protect fiber under more severe conditions downhole.

Protecting optical fibers can be at odds with strain sensing. Most standard optical fiber cables protect fiber by decoupling it from external strains, which is the role of the Kevlar braid in tactical cable, for example. However, using optical fiber as a strain sensor requires that it is coupled to the formation, and it also requires that the strain field in the formation is unaltered by the presence of the fiber. For example, one possibility is to put optical fiber in a borehole and then fill the borehole with cement grout that bonds to both the fiber and the formation. This could be effective where the borehole is in competent rock with an elastic modulus similar to that of cement grout ($E \sim 10$ GPa). However, if the borehole is in unconsolidated sediment or saprolite ($E < 0.1$ GPa) the cement grout would be a stiff inclusion, and this would likely cause the strain measured by the fiber to be less than the strain in the formation.

A method of packaging the optical fiber was developed that addresses the dual problem of protecting the fiber and coupling it to the formation. The approach is to encase the 250-micron fiber in a thin, flat strip of material that is strong enough to offer protection, but compliant enough to transfer strain. Optical fiber packaged in a long, flat strip of material will be called a "strain ribbon."

Borehole Completion

The strain ribbon developed for this project was coupled to the formation using friction. This was accomplished by placing the ribbon along the axis of a borehole. A

polyethylene sleeve extending the length of the borehole was then inflated and filled with sand to press the ribbon against the borehole wall (Figure 2.4). The elastic modulus and density of the sand filling the sleeve are similar to that of the saprolite at the field site. Matching the elastic modulus and density limits the perturbations in the strain field caused by the sand-filled borehole.

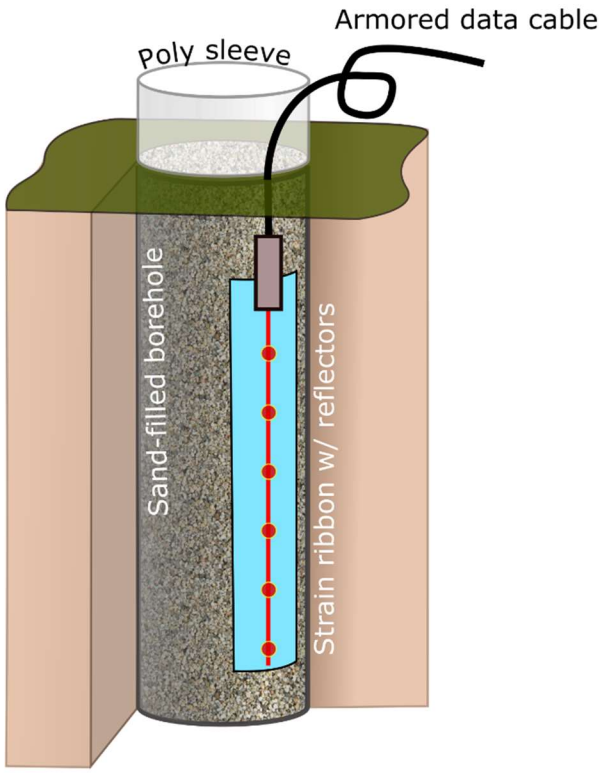

Figure 2.4: Perspective view of strain ribbon wellbore completion.

Conditions for slip

The strain ribbon is designed to couple the optical fiber to the formation through friction. We assumed that the frictional strength between the ribbon and the formation is:

$$\tau = (\sigma_n - p)\mu \qquad \text{Equation 2.16}$$

where:

σ_n = the normal stress (positive is compression)

p = the pore pressure in the formation

μ = the coefficient of friction between the ribbon and the formation

The normal force is assumed to be created from the weight of the sand in the polyethylene sleeve. Assuming the strain at the wall is negligible and the diameter of the sleeve is large enough to limit bridging, the normal force on a vertical wall is

$$\sigma_n = \frac{\nu}{1-\nu}\gamma_s d \qquad \text{Equation 2.17}$$

where:

γ_s = the unit weight of the sand

ν = Poisson's ratio

d = depth

The problem of slip between the ribbon and the formation was analyzed using a force balance, which gives the critical strain gradient in the direction of the ribbon that can cause slip:

$$\frac{d\varepsilon}{dz} = wC_T\tau \qquad \text{Equation 2.18}$$

where:

C_T = the axial compliance (strain/axial force) of the ribbon,

w = the width of the ribbon.

It follows that the strain gradient that would cause slip increases as a linear function of depth:

$$\frac{d\varepsilon}{dz} = \frac{\nu}{1-\nu} wC_T\mu\gamma_s d - wC_T\mu p \qquad \text{Equation 2.19}$$

Polyester film strain ribbon

The strain ribbon used in this investigation was formed by laminating optical fiber between two strips of transparent polyester film. The film is 140 microns thick, and is coated with a strong contact adhesive (ASTM D3330 peel strength of 15.3 N/cm according to the manufacturer). The film is available in rolls and is marketed as 3M™ Super Bond Film Tape 396.

A strain ribbon was created by adhering the optical fiber to the center line of one piece of film and then bonding them to another piece of film. The adhesive sides of both films contacted the fiber and each other to form a single strip with the optical fiber along the center axis. Prototypes and short ribbons were created manually to establish proof-of-concept, but this process was only capable of creating ribbons up to 1 m long. The films could become misaligned or wrinkled, or the tension in the two sides of the film could be unequal, which caused the ribbon to bend or buckle. A packaging device was

developed to avoid some of these problems. The device contains two spools of the polyester film along with a spool of optical fiber containing reflectors. The polyester films are passed through rollers and pressed together as the fiber is aligned along their centerline. The assembled ribbon is then wound on a spool (Figure 2.6). Strain ribbons up to 10 m long were created with the packaging device, and it would be possible to create even longer ribbons.

Light is transmitted from the laser in the interrogator to the strain ribbon through a tactical optical fiber cable. A fusion splice is used to couple optical fiber in the tactical cable to the fiber in the ribbon. The splice is particularly fragile, so it is encased in a block of epoxy and reinforced with aluminum.

Data was developed to evaluate conditions that could cause slip of the polyester ribbon using Equation 2.19. The ribbon was put in a loading frame to measure displacement as a function of axial load (Figure 2.5). These data show that the strain is a linear function of applied load. The data in Figure 2.5 were measured using a ribbon that was 2.5 cm, but the width of the ribbon used in the field is $w = 5$ cm. As a result, the compliance of the ribbon used in the field is half that measured in Figure 2.5, so the compliance of the ribbon used in the field is $C_T = 45$ me/N. The unit weight of the sand used in field deployments is 18000 Pa/m, and Poisson's ratio is assumed to be between 0.25 – 0.4. The coefficient of friction between the polyester film and sand was measured in the laboratory to be in the range $0.2 < m < 0.3$.

The pore pressure where the ribbon was deployed at the field site is negative because the ribbon is above the water table. A negative pore pressure will increase the

shear stress required to cause slip, which will improve performance. However, it is possible that pressures in the vadose zone could reach zero if the water table were to rise significantly, or if there was extensive infiltration. Accordingly, pressure was set to $p = 0$ in Equation 2.19 to provide a conservative estimate of the strain gradient that could cause slip.

The results (Figure 2.5) indicate that the strain gradient that would cause slip increases from zero at the ground surface to 0.01 1/m at approximately 2 m depth and 0.05 1/m at 10 m depth. The strain gradients expected to occur during pumping tests will be evaluated in the following pages, but they are expected to be much less than 0.01 1/m. As a result, this analysis indicates that friction should keep the strain ribbon coupled to the formation.

a.)

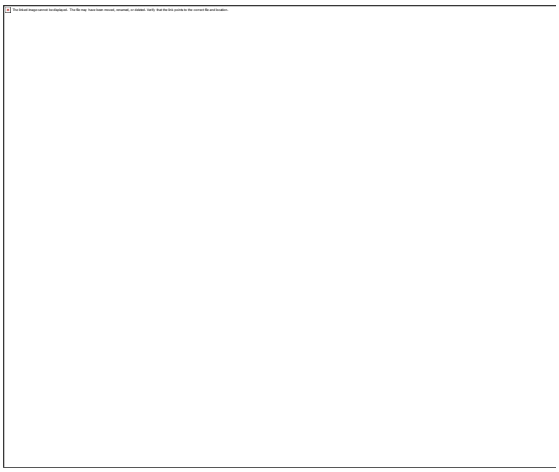

b.)

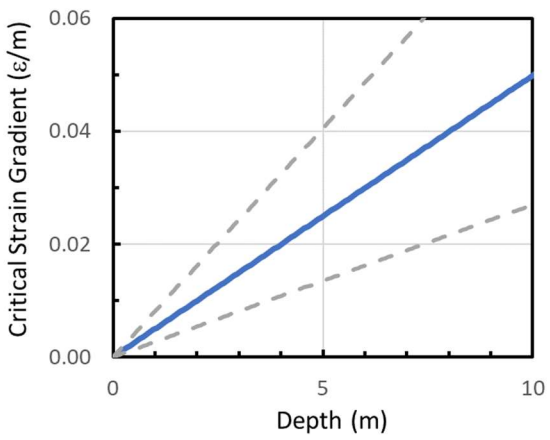

Figure 2.5 a.) strain as a function of applied axial load for two-layer, 2.5 cm wide polyester ribbon. b.) Critical strain gradient as a function of depth using the range of

parameters given in text (dashed line) and using the average values of parameter (solid line).

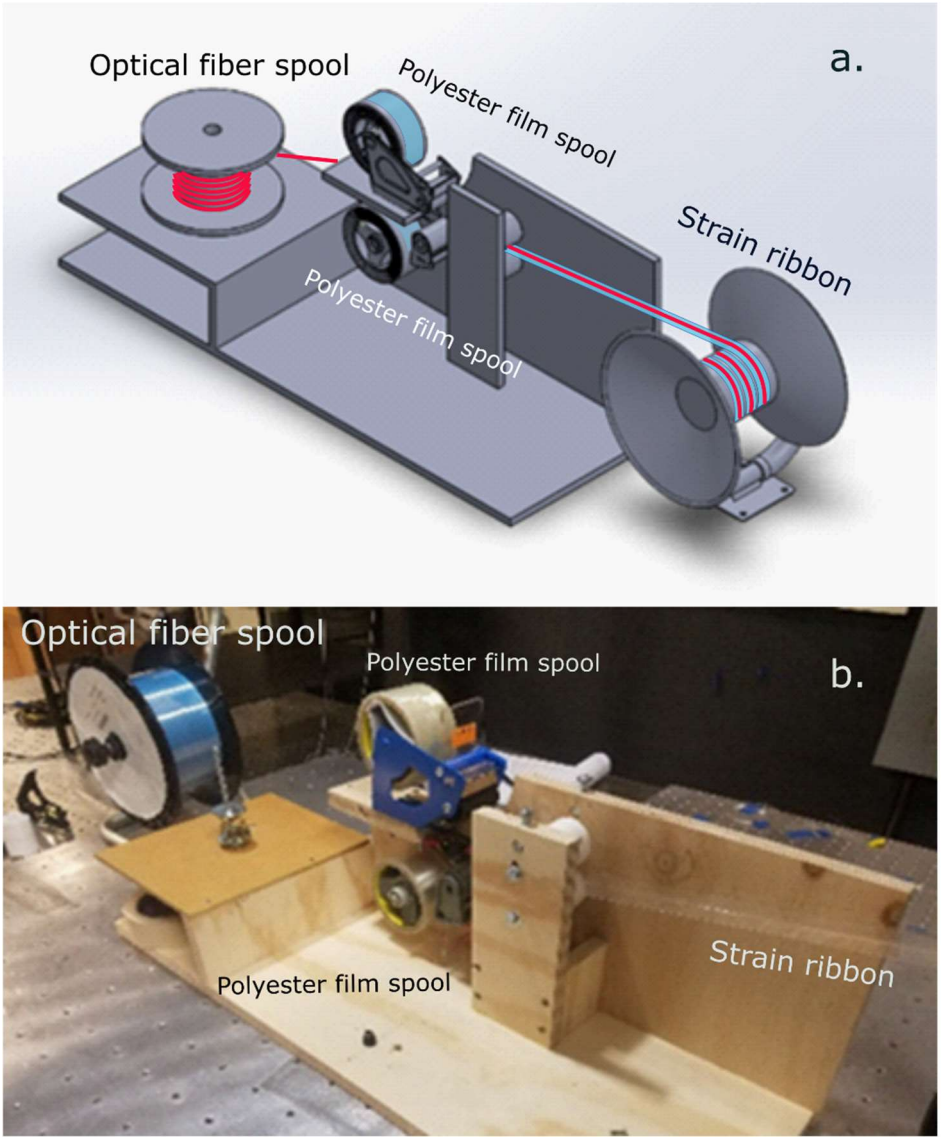

Figure 2.6: Device for creating a strain ribbon by laminating an optical fiber between two pieces of polyester film. a.) design; b.) prototype.

Field Deployment of Strain Ribbon

The strain ribbon was deployed at the field site in a four-inch-diameter borehole. The borehole was drilled using a Geoprobe drill rig and a solid stem auger. The borehole was drilled to 7.6 m below the surface, which is above the water table at 9 m depth. The augers were removed, and the depth of the open hole was verified by lowering a weighted tape into the hole.

The strain ribbon and polyethylene sleeve were attached to a weight and arranged on opposite sides of the borehole. The sleeve was folded along its axis to create a bundle approximately 5 cm in diameter. The weight was then lowered into the borehole and this pulled the strain ribbon and the folded sleeve down with it. The ribbon was directed over a roller at the top of the hole to limit the potential for sharply bending the ribbon as it curved downward into the hole (Figure 2.8a). The sleeve was directed into the borehole manually (Figure 2.8b).

a.) b.)

Figure 2.7: Polyethylene sleeve being prepared for installation in the borehole. a: Tubing meaning measured. b: Tubing being folded.

The polyethylene sleeve was inflated with approximately 5kPa air pressure after it was lowered to the bottom of the borehole (Figure 2.8). The open sleeve was filled with dry, well-sorted, medium- to fine-grained sand. To avoid bridging, sand was poured slowly, and the depth to the top of sand was measured with each 50-pound bag of sand added. The sleeve was then pressurized to between 5 and 10 kPa for approximately 1 minute to compact the sand before another bag of sand was added.

a.) b.)

Figure 2.8: Installation of the polyethylene tubing in the borehole. a.) Strain ribbon (transparent) passing over a roller at the top of the borehole. Folded polyethylene sleeve is the white band at the top of the image; b.) Close up of the borehole with the transparent strain ribbon and the folded polyethylene sleeve.

c.)

Figure 2.8c: Polyethylene sleeve is pressurized using a shop-vac pushing the strain ribbon onto the borehole wall.

The data cable from the strain ribbon was attached to the interrogator and data acquisition system during deployment. Data that indicated the strain ribbon had broken could be obtained in real time as the break occurred. This allowed us to identify and revise procedures and designs that resulted in fiber breakage.

Data Collection and Storage

For each pumping test experiment, there were three different measurements that were recorded: water pressure, strain, and flow rate. The water pressure in monitoring wells and the pumping well was measured using Onset HOBO U20 Series transducers. Each monitoring well was equipped with a U20L-04 data-logging pressure transducer capable of measuring pressure head over a span of 4 meters with a typical error of ±0.4

cm and a resolution of 0.14 cm. The pumping well used a U20L-02 logging transducer capable of measuring pressure head of up to 30.6 m with a typical error of 3.0 cm and a resolution 0.41 cm. The larger error in the transducer used in the pumping well was deemed acceptable because of the relatively large head change in the well during the pumping tests. Hydraulic head was monitored continuously at the site at a sampling rate of one reading per minute in the monitoring wells and two samples per minute in the pumping well. The water level data were manually collected one day after each test, or every 15 days when no tests were being conducted. When redeployed into a well, a minimum of one day was allotted for the transducer to generate a baseline signal before another test was performed.

Data from the paddle wheel flowmeter was measured and stored in the field on a Campbell CR1000 data logger. The data logger was programmed to count the number of pulses every 10 seconds resulting in an accuracy of ±0.1 pulse per second. The data was collected immediately following the termination of the pumping test and the pulse count was converted to a flow rate using:

$$Flow\ Rate\ (Q) = \frac{\frac{Pulses}{time}}{583.19\frac{Pulses}{gallon}} \qquad \text{Equation 2.20}$$

Site Description

The field site used for this research is at the Clemson University Simpson Station in Pendleton, SC (34.670018, 282.729311). The site is a 0.25 ha subsection of a 12-ha

pasture used for grazing cattle. The primary vegetation is fescue grass (*Festuca arundinacea*).

Geology and Hydrogeology

The site is underlaid by the Caesar's Head granite, which is a biotite-granitoid gneiss, at a depth of approximately 30 m (Murdoch et al. 2006). Saprolite derived from the gneiss occurs from approximately 2.5m to 30m depth. The hydraulic conductivity of the saprolite is $2.4x10^{-5}$ m/s at 3m depth (Murdoch et al. 2006). Constant-rate pumping tests indicate the hydraulic conductivity is an order of magnitude less, approximately $1.3x10^{-6}$ m/s, in the saturated zone below 10m depth. The upper 1.5 to 2.5m is a poorly structured clay to sandy clay loam soil, which has been mapped as the Cataula sandy loam (Soil Survey Staff). The soil is tight, with a hydraulic conductivity of less than 10^{-9} m/s, according to measurements made using a Guelph permeameter (Murdoch et al. 2006).

The depth of the water table is approximately 9 m. The hydraulic head gradient indicates groundwater flow is to the northeast toward Little Garvin Creek, which is 500 m east of the site. Big Garvin Creek is 800 m west of the field site.

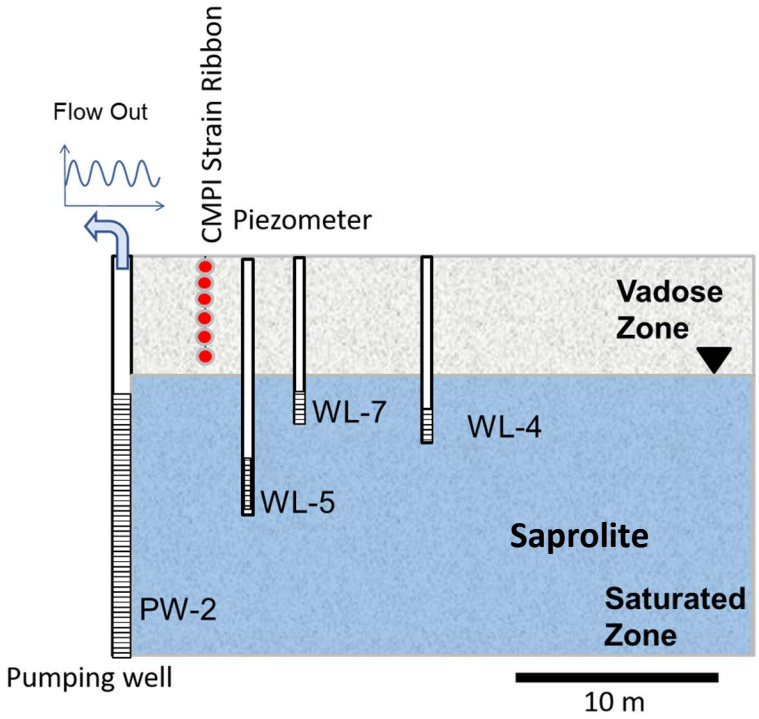

Figure 2.9: A conceptual model of the subject field site including the pumping well (PW-2), the CMPI strain ribbon, and the piezometers.

Wells and Sensors

The field site includes several dozen borings and sensors that have been used for a variety of projects, but only a subset of wells, piezometers, and strain sensors were used for this investigation (Figure 2.10). Groundwater well PW-2 was used for pumping, and piezometers WL-4, WL-5, and WL-7 were used to monitor hydraulic head. Well PW-2 was drilled to approximately 30m depth, which is the depth to top of competent rock. The borehole was drilled using an 8-inch diameter air rotary bit. The filter pack extends from the bottom of the borehole to 10m below ground surface, with the intent to capture then entire saturated zone. Bentonite was used to seal the annulus above the screen zone,

and the remaining annulus was filled with a neat cement grout. The casing and screen are made from 4-inch diameter flush-joint PVC pipe. The slots in the well screen are 0.010 inch wide. Each piezometer (WL-4, WL-5, and WL-7) was installed using a 4-inch outer diameter solid -stem auger. WL-4 was installed to a depth of 15.3 m and is completed with 2-inch PVC casing and screen. It is screened from 13.8 m to 15.3 m with a total screen length of 1.5 m. WL-4 is located 20.9 m from PW-2. Well WL-5 is 21.1-m deep and is completed with 2-inch PVC pipe. It is screened from 18.1 m to 21.1 m with a total screen length of 3.0 m. WL-5 is 6.7 m from PW-2. Well WL-7 is screened from 11.39 m to 13.45 m with a screen length of 1.5 m, and it is completed with 1 ½-inch PVC casing and screen. WL-7 is 9.1 m from PW-2.

The piezometers were equipped with Onset HOBO U20L-04 pressure transducers, which have a span of 0 – 4 m and a resolution of 0.14 cm. They were programmed to measure pressure every one minute during each pumping test.

Strain was measured at SR-2, which is 4.4m from PW-2. The strain ribbon at SR-2 was built with reflectors spaced 15 cm apart with the midpoint of the reflectors at depths of 1.0 m, 1.85 m, 2.7 m, 4.4 m, 5.25 m, and 6.95 m.

Flow rate data were logged with a Campbell CR-1000 located on the western edge of the field site. The interrogator and data acquisition system for the CMPI system were housed in the building to the east of the field site (Figure 2.10).

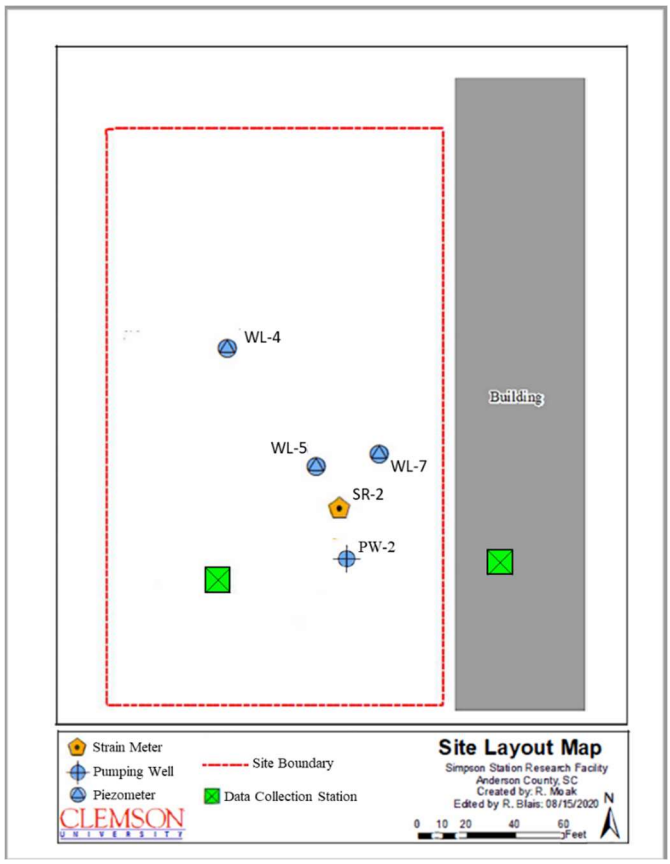

Figure 2.10: A map of the field site at Clemson University Simpson Station showing the locations of the pumping well, piezometers, strain ribbons, and other features of the site.

Numerical Analysis

A numerical model of deformation during sinusoidal-rate pumping was developed to help plan the field tests. The model assumes fully coupled poroelasticity in 2-D axisymmetric geometry configured to represent the field site. The governing equations are solved using the finite element method using COMSOL Multiphysics 5.4.

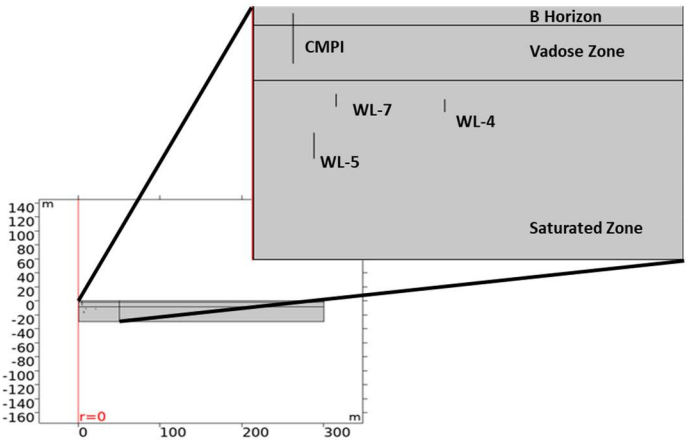

Figure 2.11: Geometry used in the COMSOL model including the area of interest, with labels for the location of the CMPI, and each of the three observation wells (WL-4, WL-5, WL-7).

The model geometry is shaped like a circular prism, 300 m in radius and 30 m high, which is simulated by assuming axial symmetry. The 300m radius is assumed to be long enough so the boundary has no effect on the processes in the vicinity of the well. The 30 m height of the model represents the saprolite, so the top of the model is the ground surface, and the bottom is the contact between saprolite and gneiss. The model includes three internal zones.

The model requires boundary conditions for fluid flow and stresses on the solid. The top of the model is bounded by no-flow and stress-free conditions representing the ground surface. The bottom of the model is bounded by no-flow and a roller boundary (zero normal displacement) representing unfractured gneiss below the saprolite. Uniform and constant heads and roller conditions were assumed on the outer boundary. A uniform mass flux was used to simulate pumping along the full length of the well screen (10-30 m below the surface). A sinusoidal pumping rate of with an amplitude of 2.5 gallons per

minute with a period of 30 minutes were used in the simulation. Table 2.1: Material and Fluid Properties contains values for the material and fluid properties that were specified for the simulations. These values have been calculated and compiled for the field site from previous well and lab tests.

Table 2.1: Material and Fluid Properties

Hydraulic Properties				
Soil Horizon	Hydraulic Conductivity (K):		9.30E-07	m/s
	Permeability (*k*):		9.50E-14	m^2
Saprolite	Hydraulic Conductivity* (K):		9.30E-06	m/s
	Permeability (*k*):		9.50E-13	m^2
	alpha_vanG* (a)		0.006	1/cm
	n_vanG*		1.3123	dim
	ThetaS*		0.5956	% vol
	ThetaR*		0.0000	% vol
Water	Fluid Density (r):		1000	kg/m^3
	Dynamic Viscosity (m):		1.00E-03	Pa*s
	Gravitational Constant (g):		9.81	m/s^2
Elastic Properties				
Soil Horizon	E_Soil		1.00E+08	Pa
	*v*_Soil		0.3	dim
	G_Soil		3.85E+07	N/m^2
Saprolite	Vadose	E_Vad	1.00E+08	Pa
		*v*_Vad	0.25	dim
		G_Vad	4.00E+07	N/m^2
	Saturated	E_Sat	1.00E+08	Pa
		*v*_Sat	0.25	dim
		G_Sat	4.00E+07	N/m^2

The mesh used was user controlled, with a finer mesh located in the area of interest (0-50 m radially) with a maximum element size of 0.5 m. Beyond the area of interest, a coarser triangular mesh was used with a maximum element size of 15.9 m.

The solid mechanics was governed by

$$\frac{\partial \sigma_{ij}}{\partial x_j} = 0 \qquad \text{Equation 2.21}$$

where σ_{ij} is the total stress tensor and repeated subscripts are summed based on the Einstein convention. The total stresses are related to strains using Hooke's Law

$$\sigma_{ij} = 2G\varepsilon_{ij} + \lambda\varepsilon_{kk}\delta_{ij} - \alpha_b P\delta_{ij} \qquad \text{Equation 2.22}$$

where G is the shear modulus, λ is the Lame parameter, ε_{kk} is volumetric strain, δ_{ij} is kroniker delta and α_b is the Biot-Willis parameter.

The fluid flow was modeled assuming conservation of mass

$$0 = \nabla \cdot (\rho_w q) + \rho_w S_w \alpha_b \frac{\partial \varepsilon_{kk}}{\partial t} + \rho_w \left(C_m + \frac{\phi S_w}{K_f} \right) \frac{\partial P_c}{\partial t} \qquad \text{Equation 2.23}$$

where ρ_w is density of water, q is the volumetric flux vector of water, S_w is water saturation, C_m is specific moisture capacity, ϕ is porosity, K_f is the bulk modulus of water, and P_c is capillary pressure. The water saturation is

$$S_w = S_e(1 - S_R) + S_R \qquad \text{Equation 2.24}$$

where S_e is the effective saturation and S_R is the residual water saturation. Darcy's Law gives

$$\mathrm{q} = -\frac{k_i k_r}{\mu}(\nabla P_c - \rho_w g \nabla z) \qquad \text{Equation 2.25}$$

where k_i is the intrinsic permeability and k_r is the relative permeability and μ is water viscosity. The effective saturation is (van Genuchten, 1980)

$$S_e = [1 + (\alpha P_c)^n]^{-m} \quad \text{Equation 2.26}$$

and the relative permeability is (van Genuchten, 1980)

$$k_{rl} = S_e^{\frac{1}{2}}\left[1 - \left(1 - S_e^{\frac{1}{m}}\right)^m\right]^2 \quad \text{Equation 2.27}$$

The numerical model was run in two steps. The first step was steady state to develop initial conditions for the water content. Pumping was not conducted during this time step. The second step was transient and included the sinusoidal variation in flux. The duration of the simulation was 43,000 seconds to simulate 12 hours of pumping. A total of 720 time steps were used so that the resolution of the output was one sample per minute, enough to ensure that each wave in the sinusoidal output was characterized.

Field Experiments

Field experiments at the field site were performed to observe the frequency and amplitude response of the strain to the flow rate. The strain data were measured as well as water levels in the pumping and monitoring wells.

Calibration

The pumping system was calibrated to establish a relationship between voltage output from the VFD and flow rate. This was achieved by changing the voltage from 2.0V to 5.0V in increments of 0.5 V. Each voltage was held for five minutes, and the rate measured by the flowmeter was averaged over that time. The data were nearly linear, and they were characterized with a best fit line. The flow rate was also manually verified using a graduated five-gallon bucket during each test.

Constant Rate

The maximum and minimum limits of the voltage inputs of the VFD were determined from the calibration experiment. It was found that any voltage input below 1.8V would result in zero flow. This set the maximum and minimum value that could be used. A constant rate test was performed at the midpoint between 1.8V and 5V, which was 3.44V. The achieved flow rate was 3.28 gpm. This rate was held for 6 hours as the water level and strain were recorded.

Sinusoidal Variation

Sinusoid-rate tests were conducted using different amplitudes and periods.

Amplitude Dependent Tests

The first round of tests evaluated different amplitudes of pumping rate. Amplitude change was determined as a percentage from test 1 (Table 2.2). The purpose of this series of tests was to evaluate the strain as a function of amplitude and to evaluate the lower limit of strain amplitude that could be evaluated. By incrementally decreasing the amplitude of the pumping rate, the resulting strain and hydraulic head amplitudes would also decrease. This also decreased the signal to noise ratio of the strain and water level.

Table 2.2: Variable amplitude testing conditions

Test	Flow Rate (gpm)			Voltage Input (V)		Period (min)	Pumping Duration (hrs.)
	High	Low	Average	High	Low		
1	5.46	0.35	3.15	5.00	1.8	30	6
2	4.64	1.67	3.21	4.5	2.3	30	6
3	3.96	2.52	3.25	3.9	2.9	30	6
4	3.78	2.88	3.33	3.8	3.1	30	6
5	3.54	3.1	3.33	3.6	3.3	30	6
6	3.41	3.17	3.3	3.5	3.4	30	6

The first pumping test used the maximum and minimum voltage inputs that the function generator could produce. This resulted in an average flow rate of 3.15 gpm with a maximum flow rate of 5.46 gpm and a minimum flow rate of 0.35 gpm. A sinusoid was fit to all the data (outlined in data analysis section) and amplitude of the best fit sinusoid was taken as the average amplitude. For Test 1, the average flow rate amplitude was 2.45 gpm. Test 2 was designed to have a flow rate amplitude of 50% of Test 1. The best fit amplitude was 1.46 gpm, which was 57% of the amplitude of Test 1. The best fit amplitude of Test 3 was 0.7 gpm, which was 28% of Test one. The best fit amplitude of Test 4 was 0.43 gpm, which is 17% of Test 1. The best fit amplitude of Test 5 was 0.21 gpm, which is 9% of test one. The least flowrate amplitude was 0.1 gpm during Test 6, which was 4% of Test 1.

Period Depended Tests

The second round of tests varied periods over 15, 30, and 60 minutes while using a consistent amplitude determined by the input voltage range of 1.8-5 V (Table 2.3). The goal of these experiments was to evaluate a period dependence on aquifer parameters.

Table 2.3: Variable period test conditions

Test	Period (min)	Flow Rate (gpm)			Pumping Duration (hrs.)
		High	Low	Average	
1	15	5.31	0.3	3.12	6
2	30	5.46	0.35	3.15	6
3	60	5.32	0.56	3.17	12

The pumping duration was chosen so there would be at least 6 periods available for the analysis. The pumping periods needed to be long enough so that multiple periods of pumping would not be performed prior to the first period reaching the strain sensor, making the evaluation of time delay difficult, and (2) wouldn't be so long that the frequency generated from the VFD and function generator would became unstable and produce an improper sinusoid. Condition 1 was a limitation because of the data processing technique used and the dependence of looking at the data in the frequency spectrum. This will be covered in depth in the data processing section.

Data Processing and Analysis

Each pumping test generated 6 unique files, which were identified using a file naming system that followed the form "MM.DD.YYYY_DataType". Each sensor or instrument had an independent clock, which was synchronized to local time between each test. All time data was converted to Unix time, or seconds since 00:00:00 January 1st,

1970 at UTC. Unix time was used because it converted all date and time data into a single scalar value which simplified processing.

MATLAB was used to process and plot the data. Plots of the original data were inspected for anomalies, such as missing data or abnormal values due to testing procedures or data collection errors. If there was a major problem with the data, the results that were measured were archived, and the test was repeated.

Pressure and strain data varied approximately as sinusoids, and these data were analyzed to determine the frequency, magnitude, amplitude, and time delay. For each series of sinusoidal data, a fast Fourier transform (FFT) was performed and plotted as a magnitude spectrum plot. The inputs required for the FFT were the detrended data vector and the sample rate frequency in Hz. For all the water level data, the HOBO data loggers recorded at a rate of 1 sample per minute with a resulting frequency of 1/60 Hz. The CMPI recorded data at three different frequencies among the tests, 0.1 Hz, 0.2 Hz, and 0.5 Hz. The FFT was applied to the collected data to verify that the applied periodic pumping rate was observable in the measurements taken. The output of the FFT would show any other harmonics affecting data besides the generated frequency as barometric fluctuations or earth tides. The results of the FFT were plotted as a periodogram.

The next step in processing the data is to obtain the amplitude and delay of all the sinusoidal data. This was done by generating a best fit sinusoid to the data. The first hour from each pumping test was omitted to reduce the transient effect from the start of pumping. The remaining time during the pumping test was assumed to be steady periodic flow. The data vector was then detrended to remove remaining signal drift. A

Vandermonde matrix was constructed for the sine and cosine components of the best fit. Then, using the least squares approximation, a sine wave is generated that most closely fits the data.

The best fit sinusoids are calculated for the flow rate from the well, hydraulic head, and distributed strain all independently. Each sinusoid is verified manually to ensure the best fit is reasonable. To calculate lag time, the difference in phase between flow rate and the observed signals is calculated. The result is a phase lag is in radians and is converted to degrees. To convert from degrees to time, Equation 2.28 is used.

$$\emptyset_o = \frac{|\varphi_Q - \varphi_s|}{\omega} \qquad \text{Equation 2.28}$$

where

$\emptyset_o$= phase lag [T]

φ_Q= the phase of the pumping rate [degrees]

φ_s= the phase of the measured signal (strain or pressure) [degrees]

ω= pumping frequency [360/T]

Using the phase lag, pumping frequency, and distance from the pumping well, the hydraulic diffusivity is estimated following the relationship which specifies the relationship in Equation 2.29 (Rasmussen et al., 2003a)

$$\emptyset_o = arg\left\{K_o\left(r\sqrt{\frac{i\omega}{D}}\right)\right\}$$ Equation 2.29

where

$\emptyset_o$= Phase lag [T]

K_o= the zero-order modified Bessel function

r= the distance from the pumping well [L]

ω= pumping frequency [2p/T]

D= Hydraulic diffusivity [L^2/T]

Equation 2.29 can be rewritten to get

$$\emptyset_o = F(u) = arg\{K_o(\sqrt{iu})\}$$ Equation 2.30

where u is the principal unknown. The equation is then solved for u by inversion:

$$u = F^{-1}(\emptyset_o)$$ Equation 2.31

The inverse function is approximated using a fifth-order logarithmic polynomial:

$$\ln(u) = \sum_{j=0}^{5n} c_i(ln\emptyset_o)^i$$ Equation 2.32

where c_i = [-0.12665, 2.8642, -0.47779, -0.16586, -0.076402, 0.03089].

With the phase lag known, *u* can be solved for and then aquifer diffusivity (D) can be found using:

$$D = \frac{\omega r^2}{u}$$ Equation 2.33

An alternate method to estimate hydraulic diffusivity from the time delay during a sinusoidal pumping test in a uniform confined aquifer relating to the period, after some approximation (Streltsova, 1988) is

$$t_L = C_s\sqrt{\lambda r^2} \qquad \text{Equation 2.34}$$

where

t_L = time delay

r = the radial distance between pumping well and measuring point

λ = the period of the sinusoidal wave

C_s = a constant related to the hydraulic diffusivity where

$$C_s = \sqrt{\frac{1}{4\pi \mathrm{D}}} \qquad \text{Equation 2.35}$$

This can be rewritten to

$$D = \frac{\lambda r^2}{4\pi t_L^2} \qquad \text{Equation 2.36}$$

Both methods used by Rasmussen and Streltsova are compared as part of this investigation.

CHAPTER THREE: RESULTS

Results of this study include pressure and strain data derived from numerical models and pumping tests conducted in the field. Pressure was measured at three piezometers, and strain data was measured as a function of depth using a strain ribbon in the vadose zone. Results from the numerical model include constant rate and sinusoidal pumping tests with simulated strain and pressure in the vadose zone and the aquifer.

Numerical Model

Two simulations were performed, one representing a pumping test utilizing a constant pumping rate of 3.4 gallons per minute (Figure 3.1) and one representing a sinusoidal rate pumping test ranging from 0 to 3.4 gallons per minute with a one-hour period (Figure 3.2:). A square wave was used to represent the constant rate pumping test and a sinusoid wave was used to represent sinusoid rate pumping test.

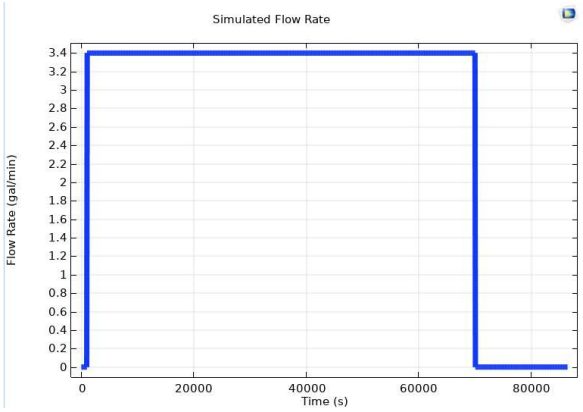

Figure 3.1: The flow rate of groundwater at the well screen as a function of time during a constant-rate pumping test followed by recovery at t = 70,000s.

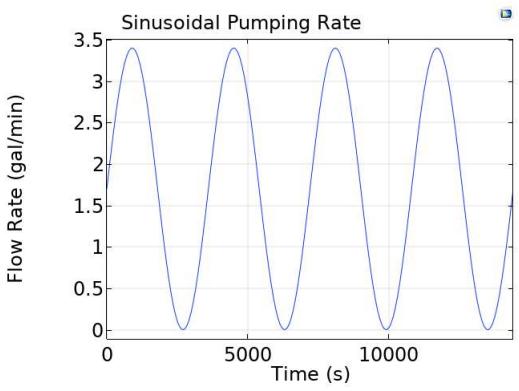

Figure 3.2: The flow rate of groundwater at the well screen as a function of time during sinusoidal pumping with a period of one hour.

The pump causes a pressure perturbation that propagates outward and upward from the well screen with time. This causes the pressure to drop sharply in the vicinity of the well screen (r = 5m, z = 3m) when the pump is turned on, but the rate of decrease is slower at greater radial distances (Figure 3.3 and Figure 3.4). For example, the pressure is essentially static during the first 5ks at the Low 20m Radial location. The pressure near the water table increases slightly at early times in response to a poroelastic effect similar to the Nordburgum effect, but then it decreased starting at approximately 20ks.

At 70,000 seconds, the flux across the well screen was reduced to zero (0) to simulate the pump being shut off. When this occurs, the simulated pressure in the aquifer begins to rapidly increase for the first 10,000 seconds before slowing down as the model returned to steady state conditions.

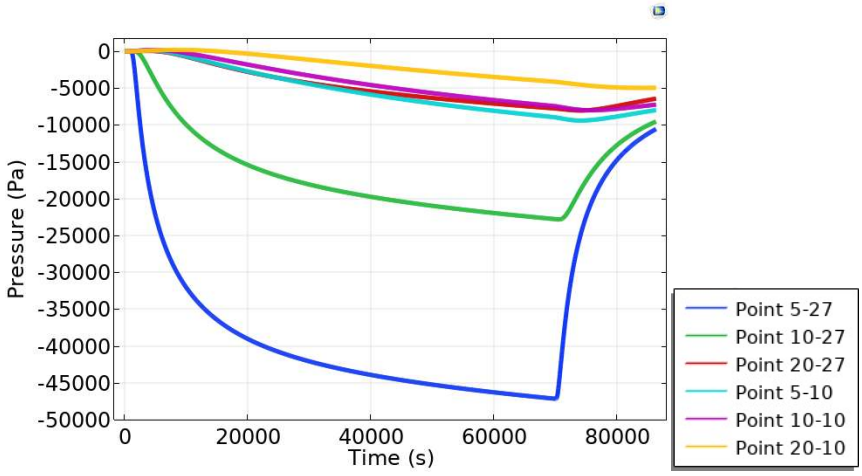

Figure 3.3: Pressure change at selected locations as functions of time during simulation of a constant-rate pumping test using model described in Chapter 2. The first number in the point name is the radial distance from the pump and the second number is the depth below ground surface (i.e. Point 10-27 is located 10m from the pump and 27m below ground surface).

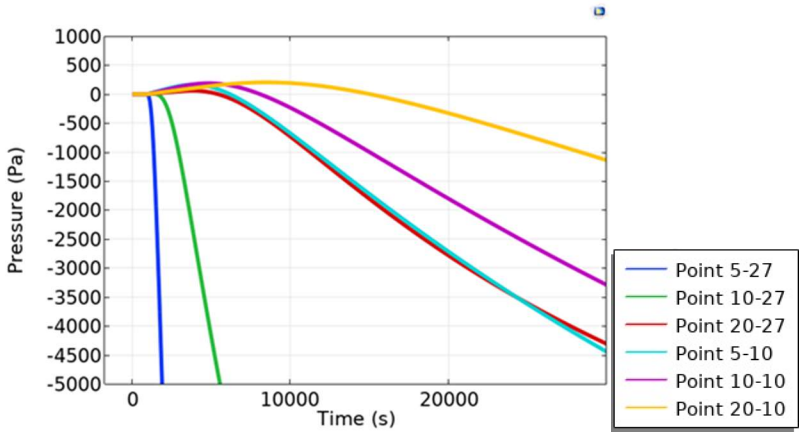

Figure 3.4: Pressure change at selected locations as functions of time during simulation of a constant-rate pumping test using model described in Chapter 2.

The strain increases during pumping, but once the pump is turned off, the strain begins to decrease back to zero. This same pattern was expected for the shallow strain (Figure 3.5), however, once the pump was cut off, the strain increased rapidly.

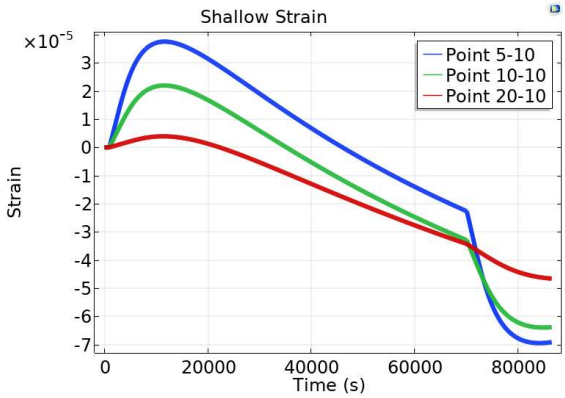

Figure 3.5: Strain at selected locations as functions of time during simulation of a constant-rate pumping test using the model described in Chapter 2.

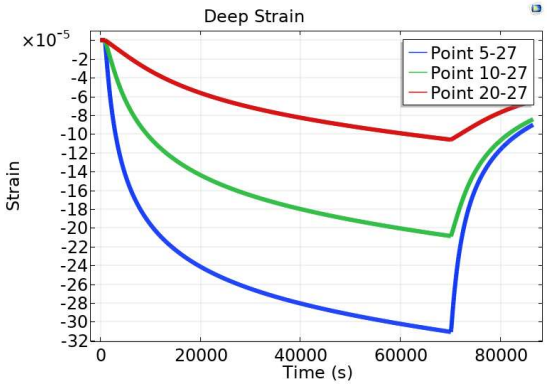

Figure 3.6: Strain change at selected locations as functions of time during simulation of a constant-rate pumping test using the model described in Chapter 2.

When the pumping simulation was initiated at time 0, the pressure at all six locations began to decrease (Figure 3.7). The three locations designated “low”

experienced the greatest pressure decrease. Additionally, as those points increased in radial distance from the well screen, the magnitude of the pressure drop decreased. The same trend is seen for the three points located 10m below the modeled ground surface. Within the calculated pressure signal, there are variations in the pressure response similar to a sinusoidal wave.

The signals observed during the sinusoidal rate pumping (Figure 3.7) are very similar in shape to the pressure signals observed from the constant rate pumping test (Figure 3.3). It is important to notice that the sinusoidal signature observed in Figure 3.7 follows the same basic shape of the pressure curve (Figure 3.3).

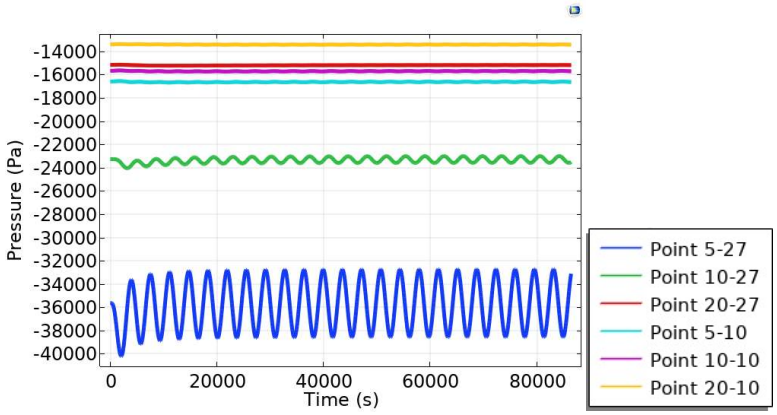

Figure 3.7: Pressure signals at six points during model of sinusoidal pumping in the aquifer. “Low” locations are located 3m off the bottom of the boundary, “high” locations represent points located along the top of the aquifer, approximately 10m below ground surface.

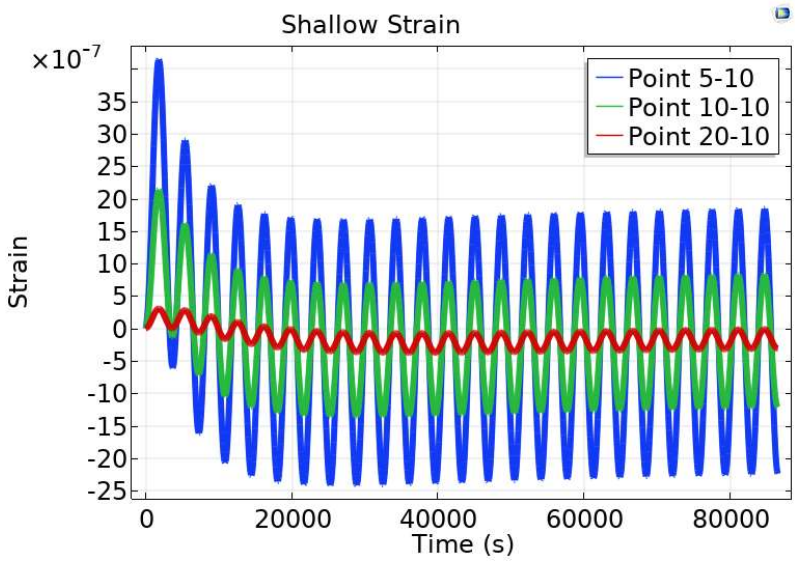

Figure 3.8: Simulated vertical strains in the shallow subsurface during sinusoidal pumping test.

Field Experiments

Nine pumping tests were performed during the field experiment. One test used a constant pumping rate, whereas the other eight used a pumping rate that varied as a sinusoidal function of time with different amplitudes and periods.

Constant Rate Pumping Test

A baseline pumping test was conducted on March 22, 2020. The pumping test lasted for 6 hours at a rate of 3.3 gallons per minute (Figure 3.9). Drawdown was recorded in the three piezometers, and strain was measured along the strain ribbon. Barometric pressure data was not removed from the hydraulic head (drawdown) data.

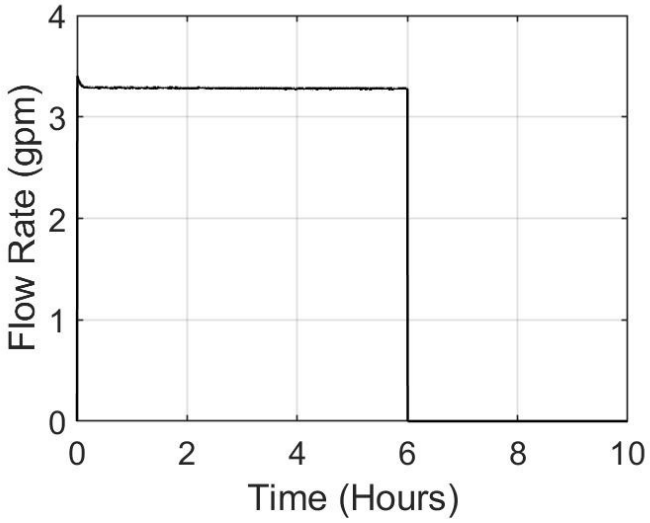

Figure 3.9: Flow rate measured during the constant-rate pumping test.

Pressure Data

The greatest rate of drawdown increase occurs soon after the pump is turned on, and the rate slowly drops until the pump is turned off at hour 6 (Figure 3.10). The drawdown drops sharply when the pump is turned off and pressure recovery begins. The greatest drawdown was 0.55m at WL-5. The maximum drawdown was 0.1m at WL-7 and 0.05m at WL-4.

The drawdown at WL-5 increases sharply at a rate of approximately 1 m/min during the first 0.5 hour of pumping. The drawdown rate slows significantly between 0.5 to 1.5 hours of pumping, and the drawdown rate is approximately 0.05 m/min (decreasing slowly with time) during the last 3 hours of the test.

The drawdown at WL-7 is slow to change at the start of pumping, in contrast to the rapid initial drawdown at WL-5. The drawdown increases sharply after 15 minutes of pumping, however, and then the rate decreases gradually until the end of pumping,

reaching a maximum of 0.1 m. The drawdown at WL-4 follows a similar pattern, except the early period of slow drawdown is even longer and the maximum drawdown (0.05 m) is even less than at the other two piezometers.

The blue bands mark the time when the maximum drawdowns occur in each piezometer. The maximum drawdowns in WL-7 and WL-4 appear to lag slightly behind the drawdown in WL-5. The lag is approximately 4 to 16 minutes (in WL-7 and WL-4 respectively).

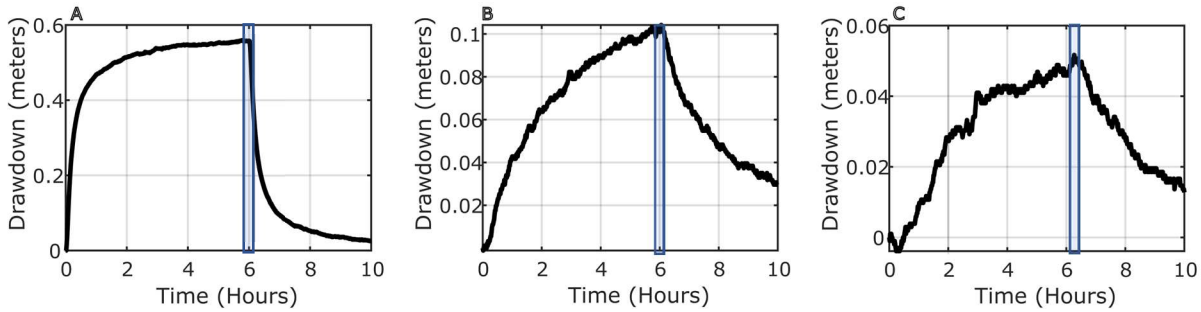

Figure 3.10: Drawdown measured at WL-5 (A), WL-7 (B), and WL-4 (C) during the constant rate pumping test. The blue boxes on each figure represent the peak drawdown at each piezometer.

The drawdown curves are marked by small fluctuations of up to a few cm in amplitude over periods of tens of seconds to tens of minutes or longer (Figure 3.10). The peaks are subtle in the data from WL-5, but they are more apparent in the data from WL-7. The peaks are even more apparent in data from WL-4 where they have amplitudes of one to a few mm of head, which is a larger fraction of the total drawdown than in data from the other piezometers.

The fluctuations in drawdown could be a result of small changes in the pumping rate, fluctuations in the barometric pressure, or other factors. The pumping rate was

measured with a flow meter and it is remarkably steady (Figure 3.9). The drawdown data was measured with a sealed transducer. A fluctuation is noticeable in all three drawdown curves at approximately hour 3. The consistency of this fluctuation across all three piezometers is likely related to changes in barometric pressure during the test.

The (Neuman, 1974) solution for an unconfined aquifer was selected to estimate the hydraulic properties from the observed drawdown. The Neuman solution assumes the aquifer is unconfined, homogeneous and anisotropic, the pumping well is fully penetrating, and storage in the well is neglected. The aquifer at the study site is an unconfined saprolite aquifer. The screened section of the pumping well is 18.3m long which spans most of the approximately 20m saturated zone of the aquifer. The drawdown measured in the three (3) piezometers, WL-5, WL-7, and WL-4 were fit to a type curve using the Neuman Solution on AQTESOLV v4.5. The solution that fits all data from all three piezometers gives an estimate of the aquifer properties (Table 3.1).

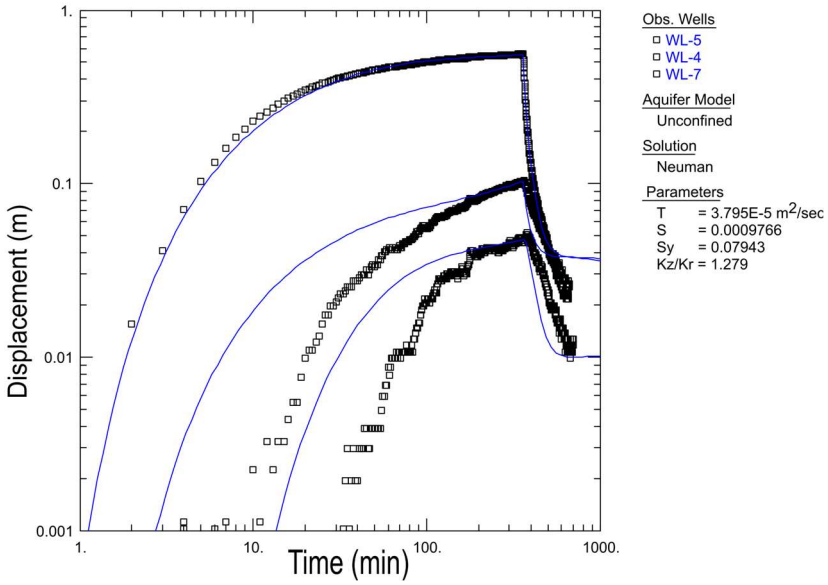

Figure 3.11. Neuman type curve overlaying drawdown (displacement) data in the three monitoring wells. WL-7 has the greatest drawdown, and WL-4 has the least drawdown.

Table 3.1: Aquifer parameters estimated from the constant rate pumping test using the Neuman solution.

Transmissivity (T) [m^2/s]	$3.8x10^{-5}$ ($\pm 7.7x10^{-7}$)
Storativity (S)	$9.7x10^{-4}$ ($\pm 1.3x10^{-5}$)
Specific Yield (S_y)	0.08 ($\pm 1.9x10^{-3}$)

The hydraulic diffusivity of a confined aquifer is estimated using

$$D_h = \frac{T}{S} \qquad \text{Equation 3.1}$$

Substituting the values of *T* and S from the Neuman Solution into the equation gives $D_h = 0.039$ m^2/sec. A well-defined confining unit is absent from the vicinity of the well, so storage change will be affected by drainage or filling of pores at the water table. In general, storage change caused by pore drainage or filling will occur in addition to

storage change from water and aquifer compressibility, so (Equation 3.1) could be viewed as

$$D_h = \frac{T}{S + S_p} \qquad \text{Equation 3.2}$$

where S_p is the contribution to storage from pore drainage. The magnitude of S_p will increase with the duration of a well test because more time will be available for pores to drain. Likewise, S_p may increase with the period of a sinusoidal well test. Values of S_p will approach the specific yield, S_y, during long well tests, so S_y will serve as an upper bound on S_p. Using the value of S_y estimated from the Neuman solution gives a lower estimate of the hydraulic diffusivity of $D_h = 4.8 \times 10^{-5}$ m^2/sec.

Strain Data

Strain was measured in the vadose zone using the strain ribbon and was recorded between sensor pairs at six locations below ground surface: 1m, 1.85m, 2.7m, 4.4m, 5.25m, and 6.95m (Figure 3.12 and Figure 3.13).

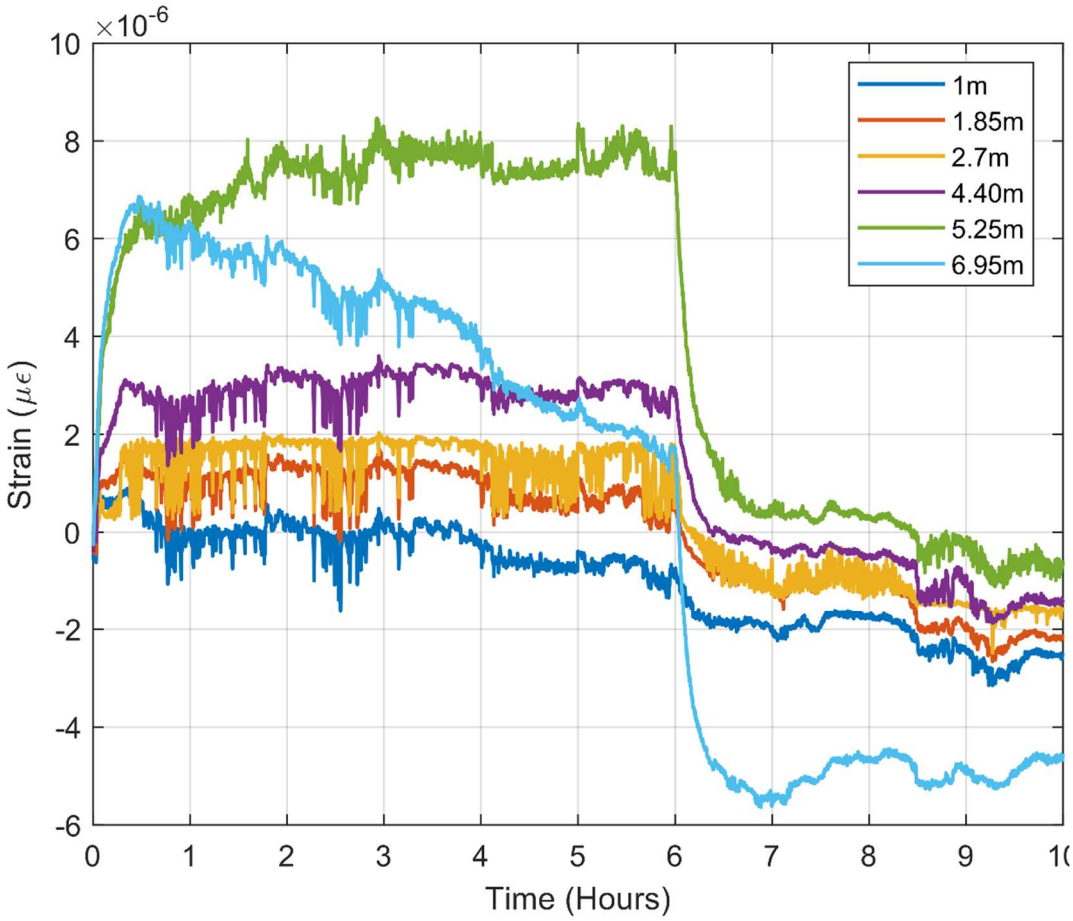

Figure 3.12. Strain between reflector pairs measured as a function of depth and time in the vadose zone during a constant-rate pumping test. Depths indicated on the legend are the midpoint between reflector pairs separated by 15 cm. Pumping was conducted from 0-6 hours. No correction for barometric pressure.

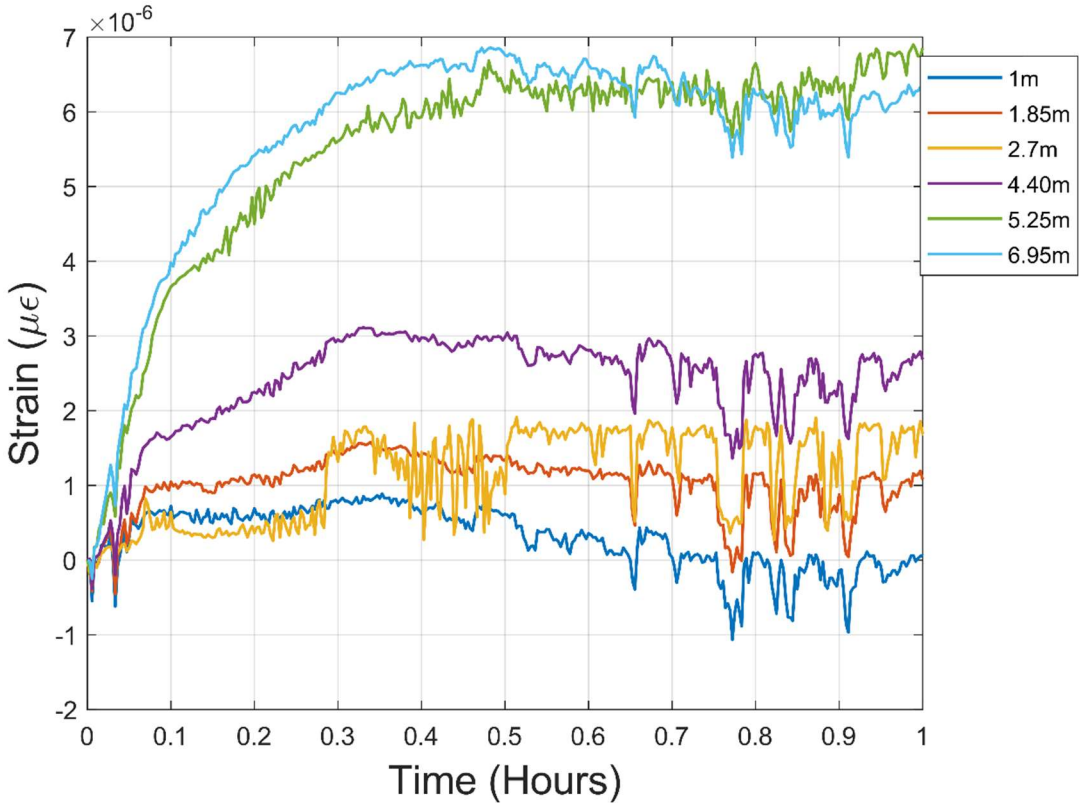

Figure 3.13: Strain measured during the first hour of the constant rate pumping test shown in Figure 3.12.

The general pattern of vertical strain follows the pattern of drawdown. The strain increases (becomes tensile) when the pump starts and the strain rate is greatest during the first 6 minutes (0.1 hr in Figure 3.13). This is when the rate of drawdown near the well was the greatest. The strain rate is greatest at the deepest reflector pair (0.01 me/s at 6.95 m) and it slows progressively upward to 0.002 me/s at the upper two reflector pairs at 1.85 and 1 m depth (Figure 3.13). The rate of increase of the strain slows after 6 minutes (0.1 hr) and the strain reaches maximum values at $0.5 < t < 2$ hr. The greatest strain is 7 me at a depth of 5.25 m and the maximum strain decreases upward to approximately 1 me at the shallowest sensor at 1 m depth (Figure 3.12 and Figure 3.11).

The magnitude of the strain response during the first half hour of pumping is greatest at the greatest depth (6.95 m), but then the magnitude at 6.95 m starts to decrease while the magnitude at the overlying sensor pair (5.25 m) continues to increase. The maximum strain reached by the 6.95 m sensor pair is approximately 7 me at 0.5 hr, whereas the maximum at 5.25m is 8 me a few hours later. Interestingly, the strain at 6.95m steadily drops from 7 me at t = 0.5 hr to 2 me at the end of pumping at t = 6 hrs.

When pumping is stopped at t = 6 hr (Figure 3.12) the strain abruptly decreases, but the rate of decrease slows with time just as it did during pumping. The strain continues to become more compressive through hour 10 as the pressure in the underlying aquifer recovers from pumping (Figure 3.10).

The exception is at the 6.95m sensor where the strain increases slightly during recovery, so the response of the deepest sensor, at 6.95 m, is anomalous during both pumping and recovery. Pressure changes in during pumping and recovery in the underlying aquifer will propagate upward into the vadose zone, but the distance that the pressure changes will be limited by the low relative permeability of the partially saturated saprolite. It seems likely that pressure changes associated with pumping and recovery reach the sensor at 6.95 m depth, but not the overlying sensor, and this accounts for the anomalous behavior.

High frequency fluctuations are common in all the strain records, with fluctuations of +/- 0.5 me occurring over time periods of minutes or longer. On many occasions, the fluctuations at all the sensors are similar (e.g. between 0.7 and 0.9 hrs in Figure 3.13). Increasing barometric pressure will compress the vadose zone, while

decreasing pressure will cause the vadose zone to expand. It seems likely high frequency fluctuations that occur in multiple sensors are a result of barometric pressure fluctuations. Barometric pressure is known to fluctuation on time scales of seconds to minutes in response to wind gusts, but it also fluctuates over time scales of many hours in response to diurnal variations. Gradual increases in barometric pressure during pumping could account for the slight decreases in strain.

Strain is roughly linearly correlated to barometric pressure and it is possible to remove many of the effects of barometric pressure using a linear correction factor (Murdoch et al. 2015). This correction is done routinely, but barometric pressure measurements are unavailable during the time of the test so no correction was done.

Sinusoidal Pumping Tests

Eight pumping tests utilizing a sinusoidal flow rate were performed between March and June 2020 during the testing period. All tests performed involved pumping the well for at least 6 hours while monitoring pressure and strain. The pumping tests were categorized into two series: variable amplitude pumping tests (Tests 1-6) and variable period pumping tests (Tests 1, 7, and 8).

Variable Amplitude

Each test used a period of 30 minutes (0.5 hours) and the amplitudes ranged from 0.12 gpm to 2.5 gpm (Table 3.2 and Figure 3.14). The flow rate amplitudes in the periodic tests were varied around a mean flow rate of 3.3 gpm, which was the flow rate used in the constant rate pumping test.

Table 3.2. Amplitude and period of the flow rate during tests 1 through 6.		
Test	Flow Rate Amplitude (± gpm)	Flow Rate Period (minutes)
1	2.5	30
2	1.5	30
3	0.7	30
4	0.5	30
5	0.25	30
6	0.12	30

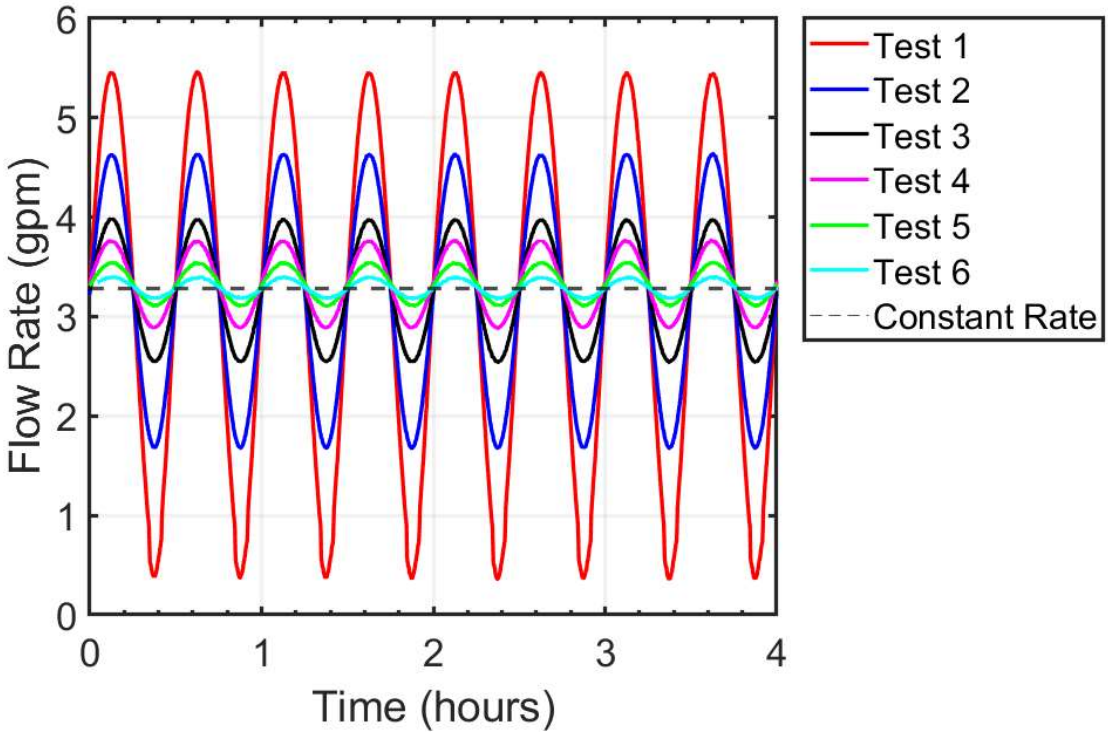

Figure 3.14: Flow rate with time measured with a flowmeter during the six variable amplitude pumping tests. The flow rate during the constant-rate test (dashed) was the mean of the sinusoidal rates.

Pressure Response

The pressure response for each test, Test 1 through Test 6, was measured in the three piezometers: WL-4, WL-5, and WL-7 (Figure 3.15). The first hour of the test was discarded to avoid the large transients that occur early in the tests.

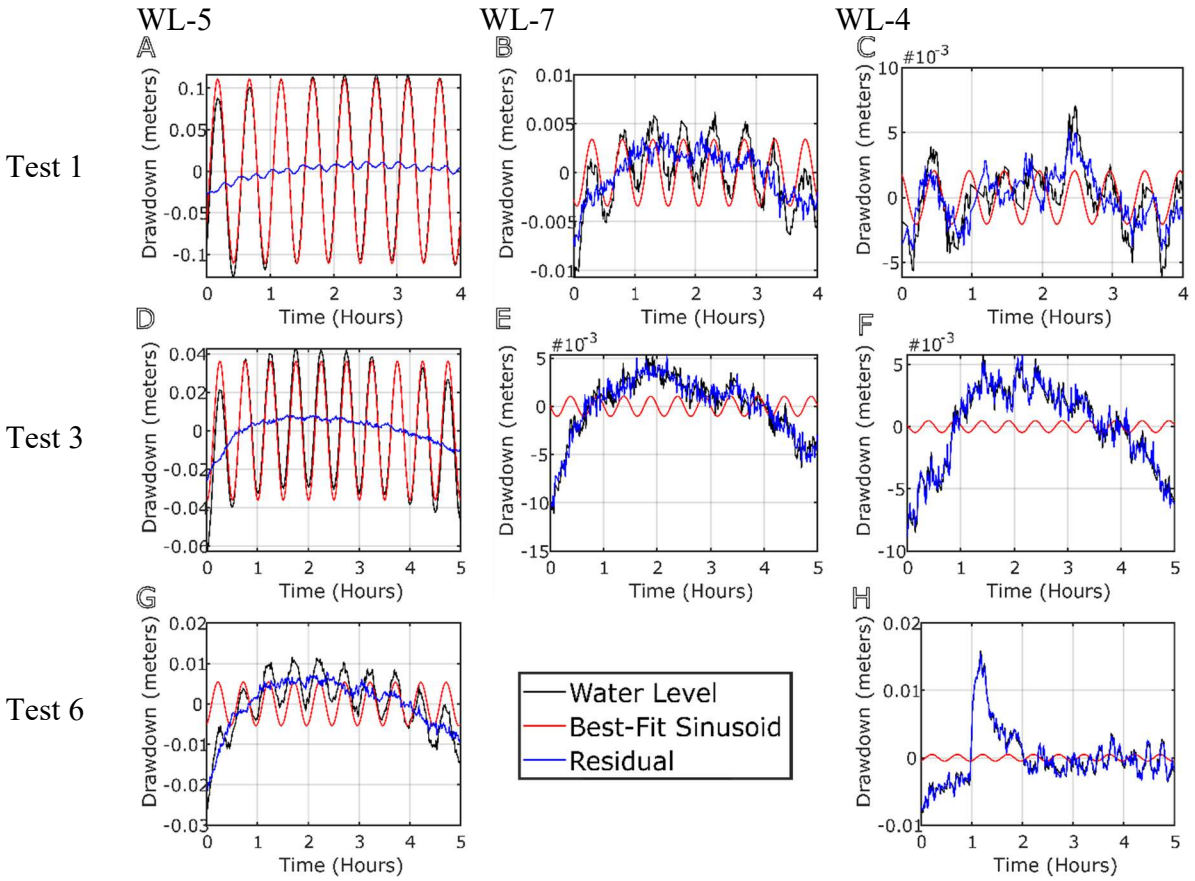

Figure 3.15: Drawdown observed in the three piezometers for Test 1 (Q =±2.5 gpm), Test 3 (Q = ± 0.7 gpm), and Test 6 (Q = ±0.12 gpm) as functions of time. Data from the first hour of pumping (first two periods) was omitted. Field data (black), best-fit sinusoid (red), residual (blue). The plot for WL-7 for Test 6 is omitted because the transducer was inadvertently not deployed prior to the start of the test.

A signal with the same period as the pumping rate was observed at each of the monitoring wells. The amplitude of the periodic pressure response largest in WL-5 for

each of the three tests, and in general the amplitude of the pressure response decreased with the amplitude of pumping and distance from the pumping well.

The variation of drawdown during Test 1 ($Q = \pm 2.5$ gpm) was +/- 0.1 m at WL-5, but it was ±0.003 m at WL-4 and ± 0.002 m at WL-4, which are further from the pumping well than WL-5. The variation in drawdown dropped in proportion to the pumping amplitude. For example, the pumping rate amplitude was $Q = \pm 0.12$ gpm during Test 6, which is 1/20 of the amplitude during Test 1. The variation of drawdown at WL-5 dropped from +/-0.1m during Test 1 to +/- 0.005 m during Test 6, a reduction by a factor of 1/20. The drawdown at WL-4 varies erratically in the range of +/- 0.001m and there is a sharp increase and fall in drawdown, but these variations appear to be unrelated to the 0.5 hr period of pumping.

The drawdown data were analyzed using a Fast Fourier Transform (FFT) to determine the magnitudes of the different spectral components. This process identifies the dominant periods that make up the drawdown signal (Figure 3.16).

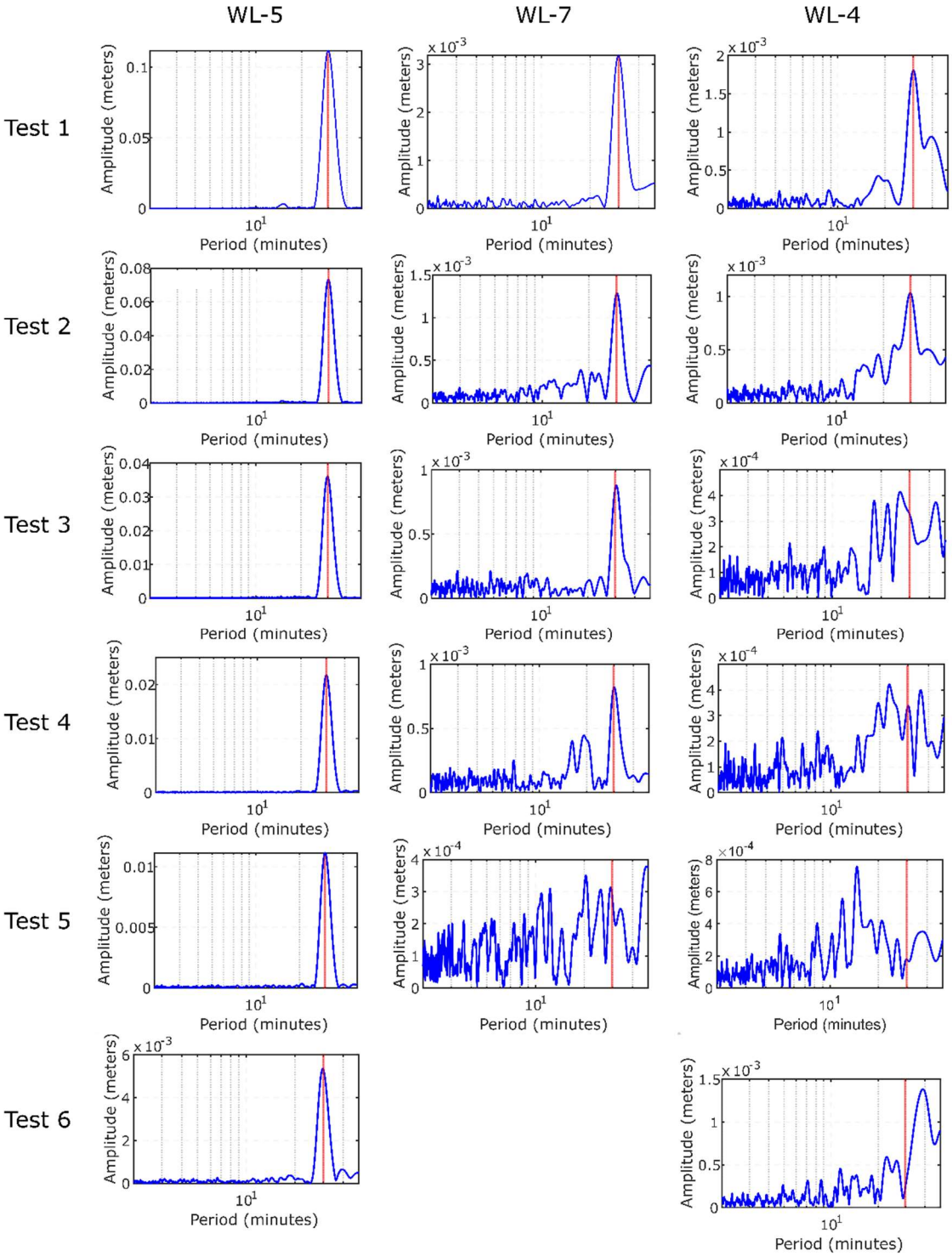

Figure 3.16: Magnitude spectra of the drawdown during the six variable rate pumping tests. The pumping period for each test was 30 minutes. The red vertical line represents the period of the pumping.

A period of 30 minutes has the largest magnitude in the spectra of all three piezometers for Tests 1 and 2. Amplitudes for the 30-minute period decrease with pumping rate, and the amplitudes for the 30-minute period at WL-4 for Tests 3 through 6 are less than the amplitudes at other periods. There is a secondary peak at 30 minutes during Test 4 at WL-4, but a discernable peak at 30 minutes is absent at WL-4 during the other tests. The amplitude of the 30-minute period is greater than background at WL-7 for all but Test 5. During Test 5, there is secondary peak at approximately 28 minutes, which is flanked by slightly larger peaks with periods of 20 and 45 minutes.

The results of the Fourier transform indicate that noise of 0.4 to 0.8 mm amplitude occurred in the range of periods similar to the 30-minute pumping period and was apparently unrelated to pumping. In some cases, there are signals with periods similar to the pumping period, but their periods are different enough so they appear unrelated to pumping. For example, at WL-4 during Test 6 the dominant signal has a 38-minute period and 1.4 mm amplitude, and during Test 4 there are peaks at periods of 22 min and 36 min, along with a peak at 30 min (Figure 3.16). I reviewed the spectra and was unable to identify any periods other than 30 minutes that appear consistently, so I conclude the other periods are noise that is unrelated to pumping. Variations in barometric pressure could cause the small variations in hydraulic head that appear as noise in the spectra.

Table 3.3. Amplitudes and delays of the hydraulic head, P_h, in different piezometers during periodic tests of different pumping amplitudes.

Tests # +/- pumping amplitude	**Piezometer, radial distance (m)**	**P_h, Amplitude (m)**	**P_h, Lag Time (min)**
Test 1 ±2.5 gpm	WL-5, 6.7	0.11	7.4
	WL-7, 9.1	0.003	15.1
	WL-4, 20.9	0.002	24.6
Test 2 ±1.5 gpm	WL-5, 6.7	0.073	7.6
	WL-7, 9.1	0.0013	16.1
	WL-4, 20.9	0.0008	N/A
Test 3 ±0.7 gpm	WL-5, 6.7	0.036	7.5
	WL-7, 9.1	0.001	14.9
	WL-4, 20.9	N/A	N/A
Test 4 ±0.5 gpm	WL-5, 6.7	0.021	N/A
	WL-7, 9.1	0.001	13.7
	WL-4, 20.9	N/A	N/A
Test 5 ±0.25 gpm	WL-5, 6.7	0.010	7.55
	WL-7, 9.1	N/A	15.5
	WL-4, 20.9	N/A	N/A
Test 6 ±0.12 gpm	WL-5, 6.7	0.005	8.0
	WL-7, 9.1	N/A	N/A
	WL-4, 20.9	N/A	N/A

During Test 1, the lag time ranges from 7.4 min at the closest piezometer, WL-5 (6.7 m), to 15.1 min at WL-7 (9.1 m), and 24.6 min at the furthest piezometer, WL-4 (20.9 m). The lag time is largely unaffected by the magnitude of pumping, however. At WL-7 the lag ranges from 13.7 to 15.5 min, but variation appears to be unrelated to the pumping rate (Table 3.3). Similar results occur in data from WL-5.

In contrast to the lag time, the amplitude of the drawdown decreases with both radial distance and the magnitude of the pumping rate. The effect of distance is illustrated during Test 1 when the amplitude decreases from 0.11m at WL-5(6.7 m) to

0.002 m at WL-4 (20.9 m). The head amplitude decreases approximately in proportion to the pumping amplitude. The smallest amplitude that can be detected is limited by the resolution of the instrument (<0.001 m).

Strain Response

Vertical strain was measured at six locations along a vertical line at approximately 4.4m from the pumping well. Vertical strain in the vadose zone varies as a sinusoidal function of time with a 30-minute period (Figure 3.17). The first hour of data was omitted to reduce the effects of transients and the amplitude and time delay of the strain data were estimated using the same least-squares fitting approach applied to the pressure data. The magnitude of strain variations during Test 1 is approximately 2.5 με at 6.95m below ground surface and it decreases upward to approximately 0.2 με (200 ne) at a depth of 1.0 m. Trends and noise levels in the data vary between the sensors. The noise level is less than 10 ne in sensors at 6.95m and 4.40m, but it is 20 to 40 ne at sensor 2.7 m and 1m (Figure 3.17).

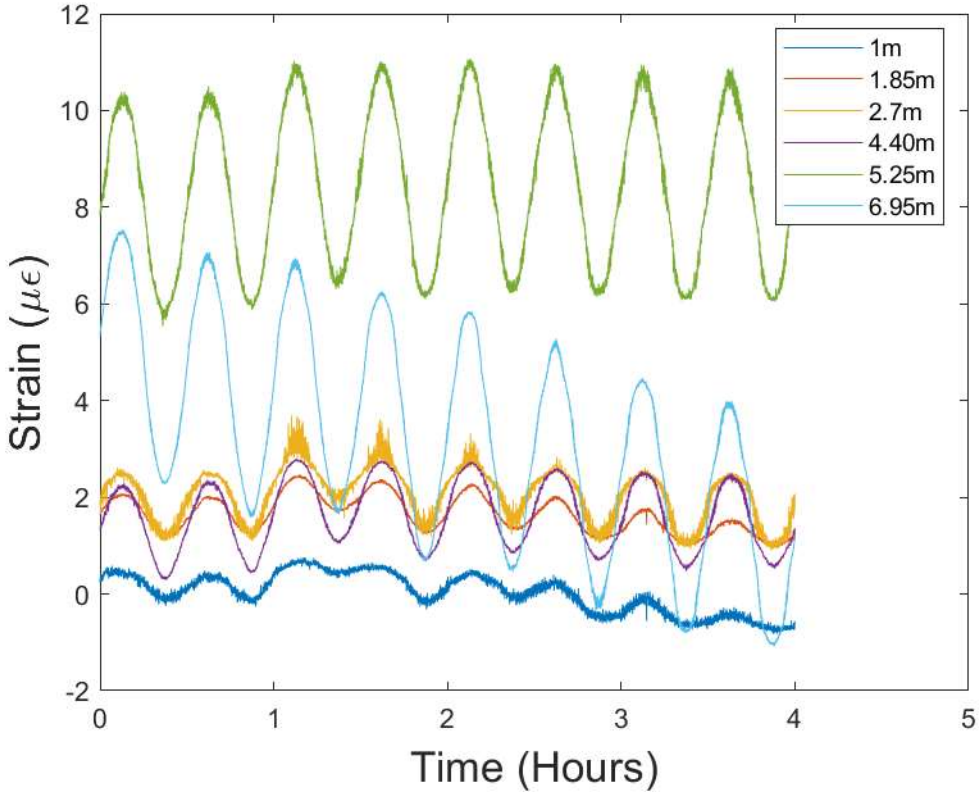

Figure 3.17: Strain measured at different depths during pumping Test 1. Data from the first hour of pumping (first two periods) was omitted. Strain is offset by arbitrary amounts. No correction for trend or barometric pressure.

The strain signal at each sensor includes small fluctuations of approximately ±10 ne (Figure 3.18).

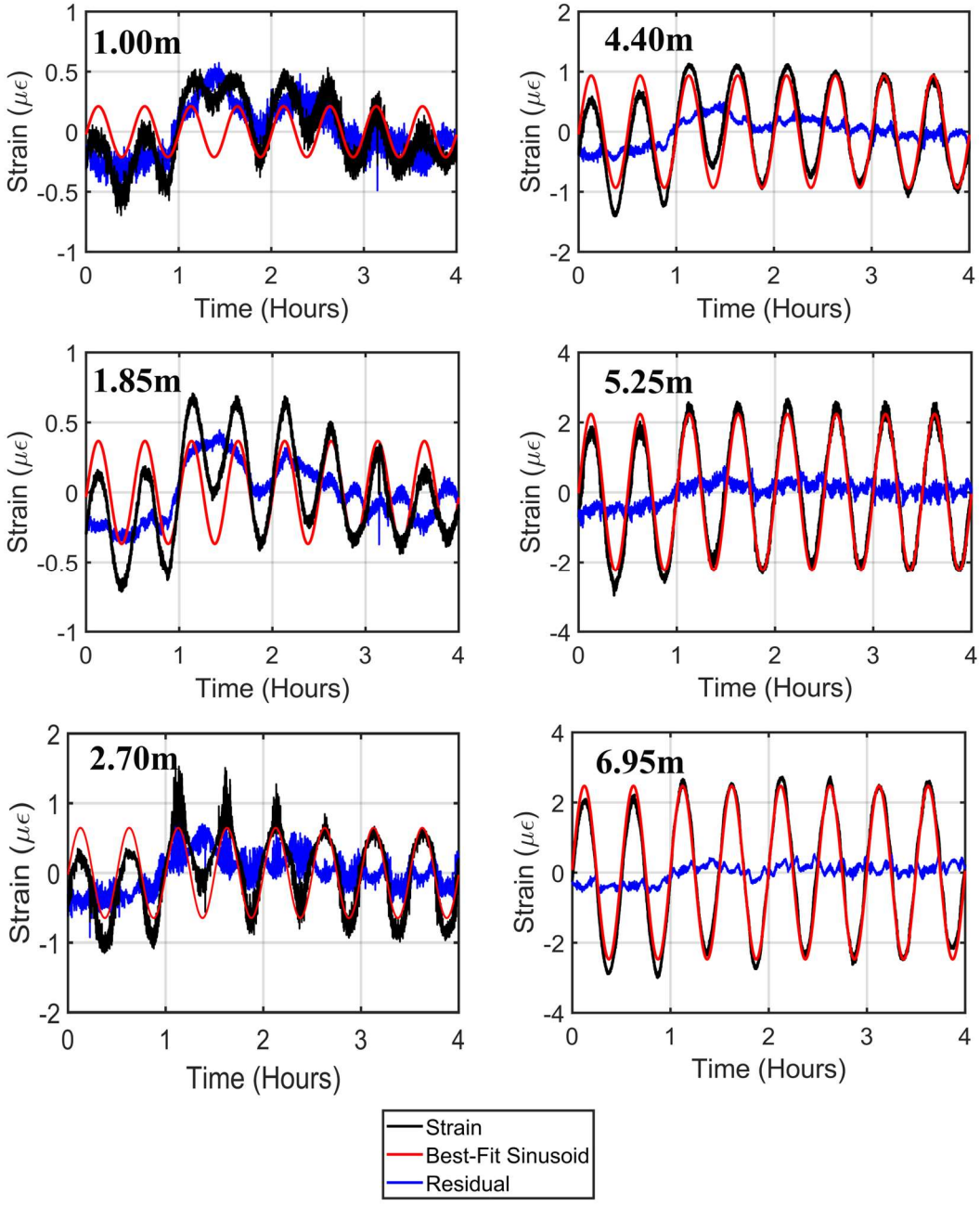

Figure 3.18: Vertical strain during Test 1 (rate, +/- 2.5 gpm). Depths to the midpoints of the sensors on the left. Field data (black), best-fit sinusoid (red), residual (blue).

The amplitude of the strain increases with depth and pumping rate, and these effects are illustrated with selected examples from three depths and three tests that used different pumping rates (Figure 3.19). The strain appears as nearly a pure sinusoid at the highest pumping rate and deepest strainmeter (Figure 3.19). In this case, the amplitude of the sinusoid is approximately 2 me and the residual resulting from noise in the strain signal is a few tenths of a me. The ratio of signal to noise increases as the pumping rate decreases. In Test 6, the strain variations are minor and difficult to discern from the background strain.

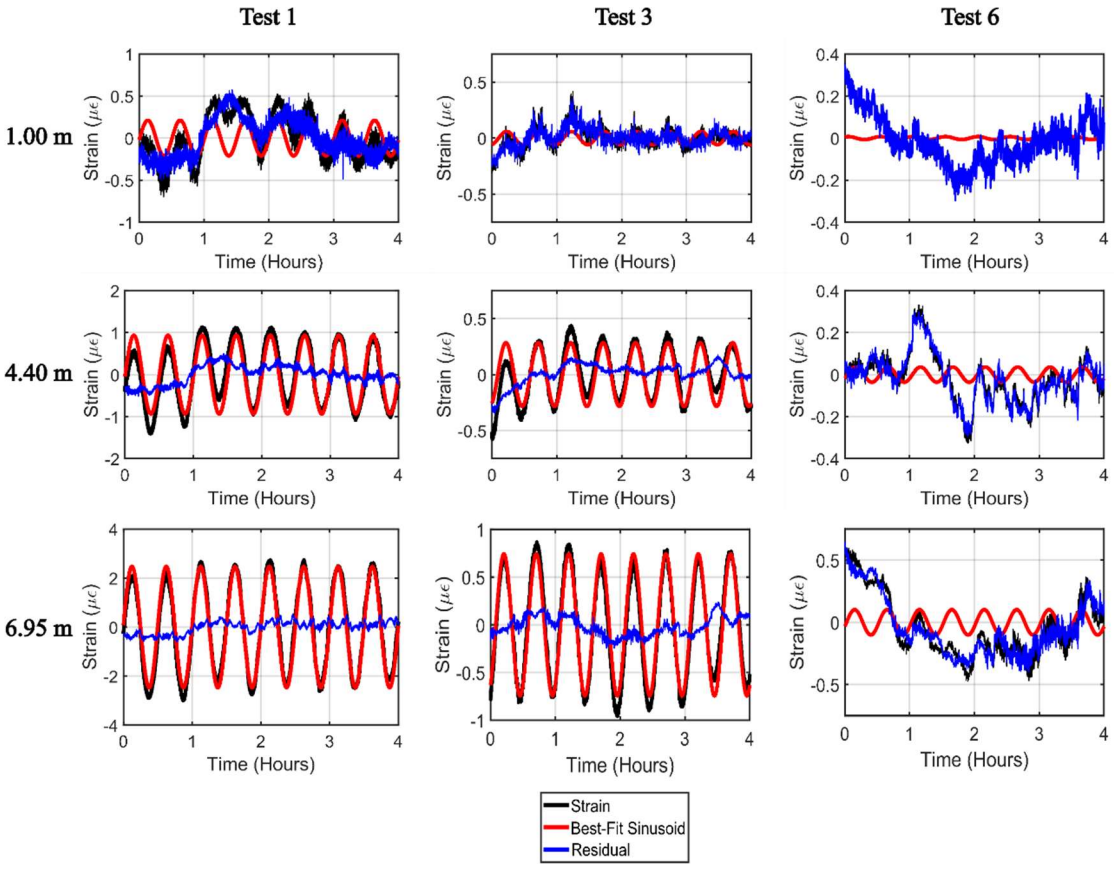

Figure 3.19: Strain response in the vadose zone during Test 1, Test 3, and Test 6 at depths (below ground surface): 1.0m 4.4m, and 6.95m. Field data (black), best-fit sinusoid (red), residual (blue).

A Fourier transform of the strain data was performed to calculate the magnitude spectra and this indicates that the maximum amplitude occurs in most cases at a 30 minute period, which is the period used at the pumping well (Figure 3.20). The amplitude increases with depth, and when the pumping rate is low there are peaks at periods less than 30 minutes that are larger than the peak at 30 minutes at the shallowest sensors. For example, during Tests 4, 5 and 6 there are peaks in the range of 10 to 30 minutes that are greater than the peaks at 30 minutes at the shallowest few sensors. Nevertheless, the peaks at the shallow sensors are readily identified in the spectra. This indicates that a Fourier transform should be capable of identifying the magnitude of the signal at the pumping period at all depths.

The amplitude spectrum during Test 6 includes a wider range of periods than in the other tests (Figure 3.20). There are multiple peaks of 0.02 to 0.04 me in the range of 15 to 40 minutes during Test 6. This noise in the signal is probably a result of strain caused by variations in barometric pressure. The amplitudes at 30 minutes at the lowest three sensors are greater than 0.04 me, and they are clearly discernable above the noise. However, strains at the shallowest three sensors at 30 minutes are of the same magnitude as the noise. Indeed, scrutiny of the spectrum from Test 6 indicates that all the peaks in the vicinity of 30 minutes are shifted slightly from 30 minutes, and the shift is greatest in the data from the shallow sensors. This is probably because the barometric pressure causes strains over a broad band of periods and this causes small shifts in the phase of the signal induced by the pumping test.

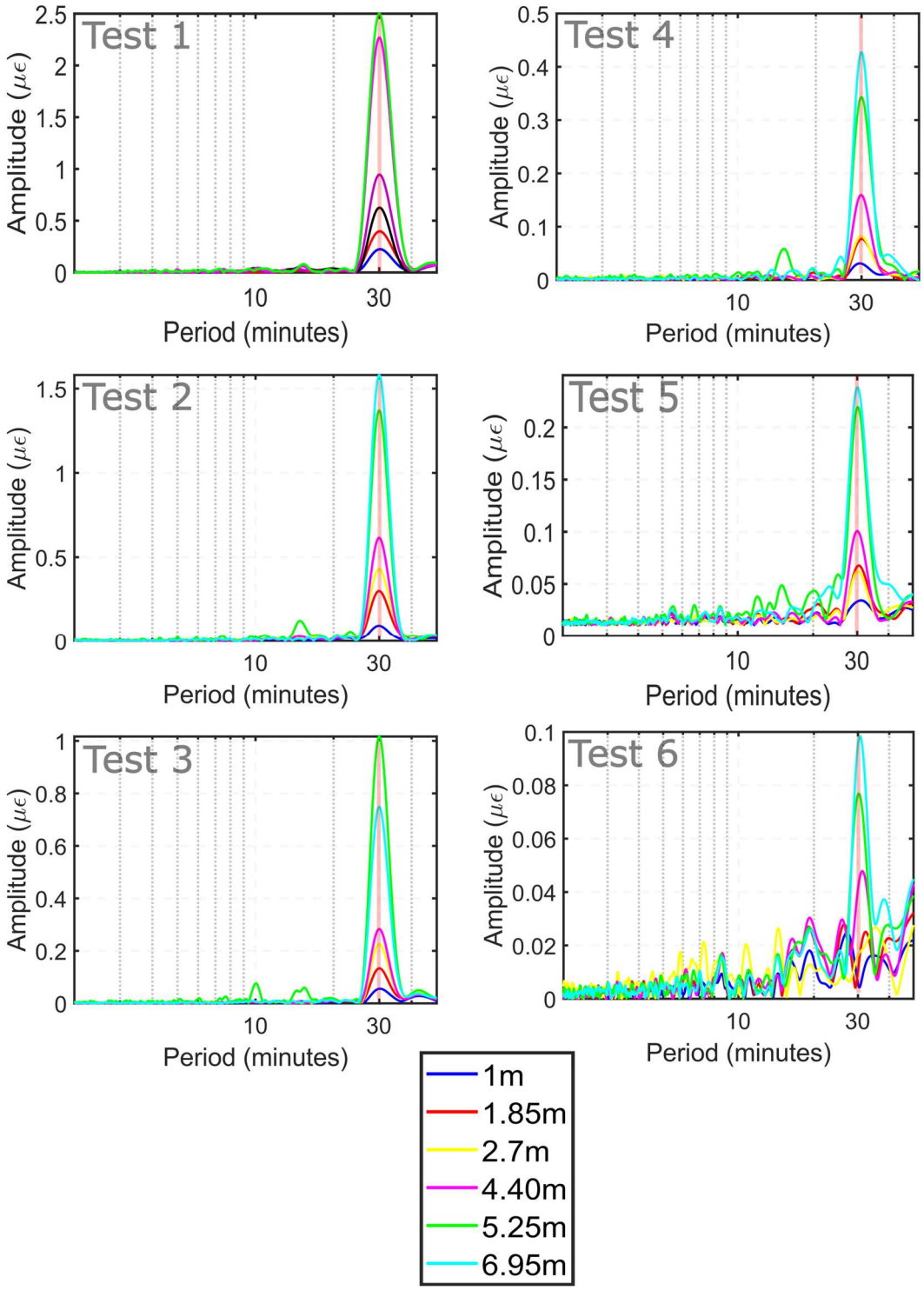

Figure 3.20**:** Magnitude spectra of the strain at each sensor pair during the six variable rate pumping tests. The pumping rate had a period of 30 minutes. The vertical red line represents the pumping period.

A summary of the strain analysis indicates that amplitude increases as the depth of the sensor pair increases (Figure 3.21). The amplitude is a linear function of depth down to 4.4 m and the gradient increases with the pumping rate. For example, the amplitude above 4.4 m increases at a gradient of 0.25 me/m for a pumping rate 2.5 gpm, and 0.14 me/m for a pumping rate of 1.5 gpm, and the gradient progressively decreases with the pumping rate. Between 4.4m and 5.25m depth there is a sharp increase in gradient that occurs during each test. Below this jump, the gradient of the amplitude is similar to the slope at shallow depth.

The time delay time is roughly 5 minutes, but it decreases with depth, and is largely independent of pumping rate (Figure 3.21). The gradient of the delay is approximately -0.11 min/m. The vertical delay velocity of the strain is the inverse of the gradient and is 9 m/min at this location.

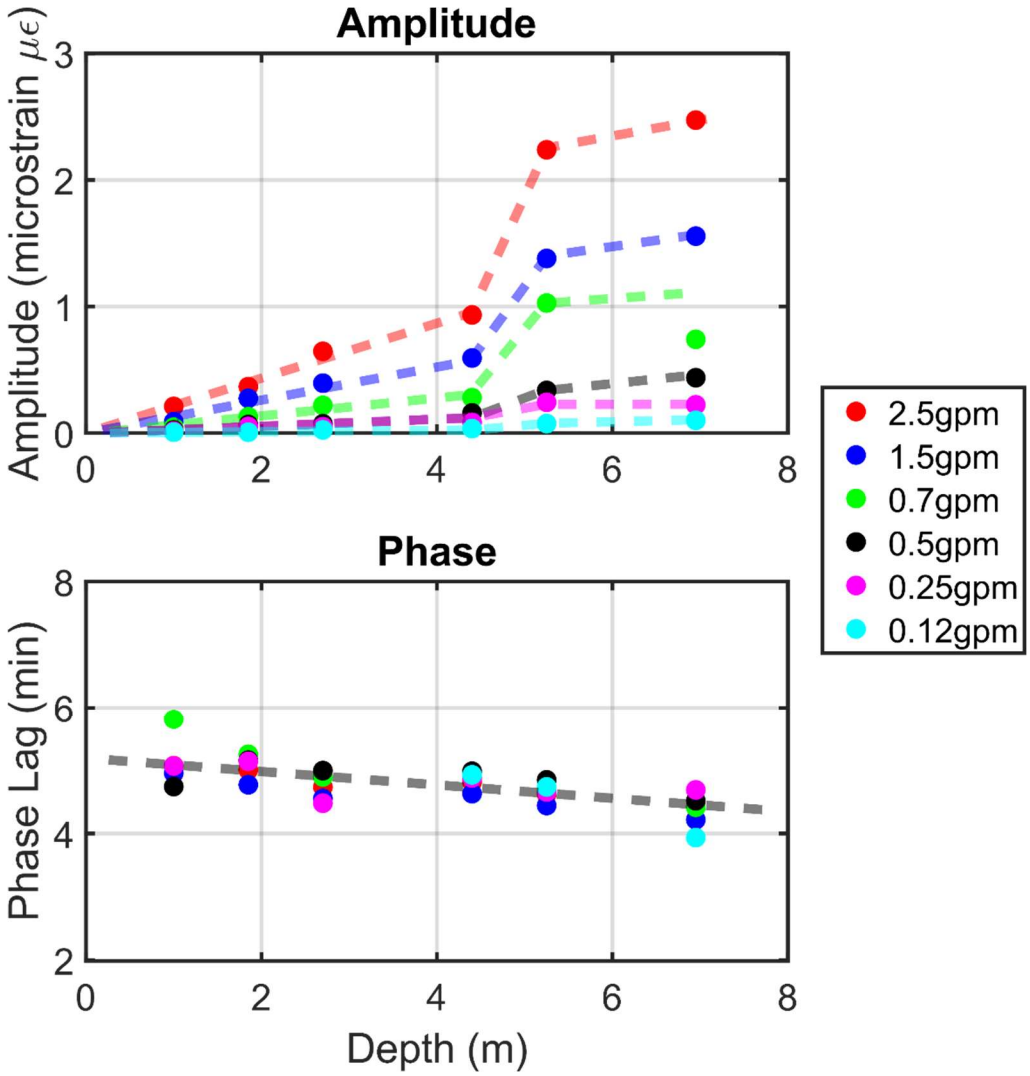

Figure 3.21: Amplitude and time lag as functions of depth for the six different periodicity tests (Test 1 through Test 6). Best fit line of the time lag for all 6 tests is y=-0.11(m/min)x(min)+5.2(min)

Variable Period

Three pumping tests were conducted using a sinusoidal rate at different periods and a flow rate amplitude of 2.5 gpm. (Table 3.4 and Figure 3.22).

Table 3.4: Flow rate amplitude and period during variable period sinusoidal pumping tests

Test	Flow Rate Amplitude (± gpm)	Flow Rate Period (minutes)
1	2.5	30
7	2.5	15
8	2.5	60

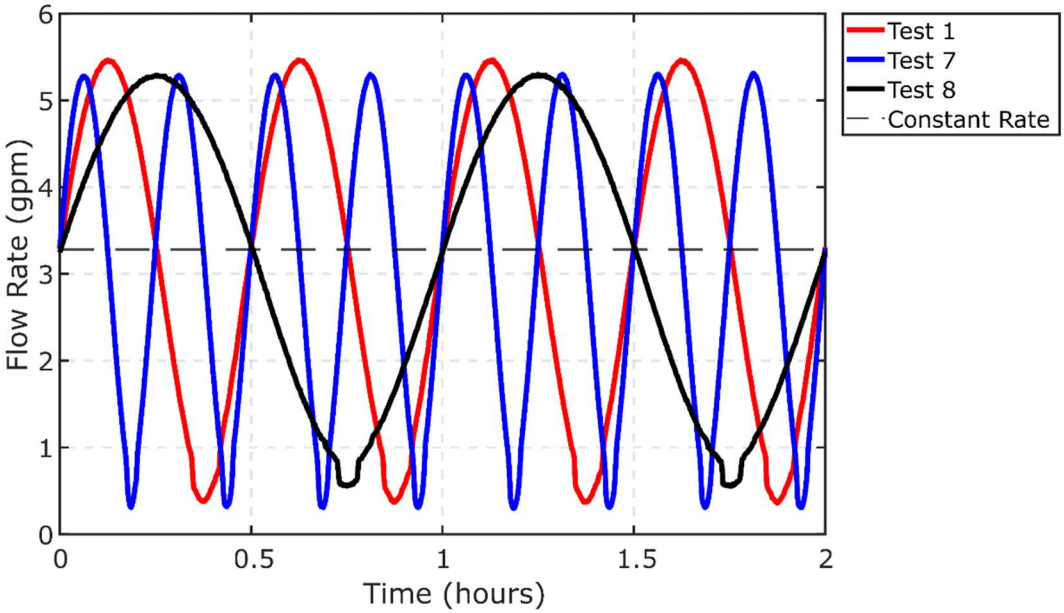

Figure 3.22: Flow rates measured with a flow meter during the three variable period pumping tests. Test 1 (red line) has a period of 30 minutes, Test 7 (blue line) has a period of 15 minutes, and Test 8 (black line) has a period of 60 minutes. The constant rate test (3.3 gpm) is also shown (black dashed line) for reference.

The flow rates were varied around a mean flow rate of 3.3 gpm, which was the flow rate used in the constant rate pumping test. The rates varied as nearly a sinusoidal

function of time, but there were slight deviations from a pure sinusoid at the low end of the rates. This occurred because at flow rates below one gallon per minute the pump and the flow meter are both at their lower limit of operation.

Pressure Response

The magnitude of drawdown increases with the period of the pumping rate, and decreases with distance from the well (Figure 3.23). There was an unknown pumping issue at approximately 1.4 hrs into Test 7 and this caused the drawdown to decrease unexpectedly. A clear sinusoidal response occurs at WL-5 during all three periods, and sinusoidal response is evident at WL-7. The sinusoidal response at WL-4 is clear in the time series from Test 8 with a period of 60 minutes, but it is obscured by noise during tests with shorter periods (Figure 3.23).

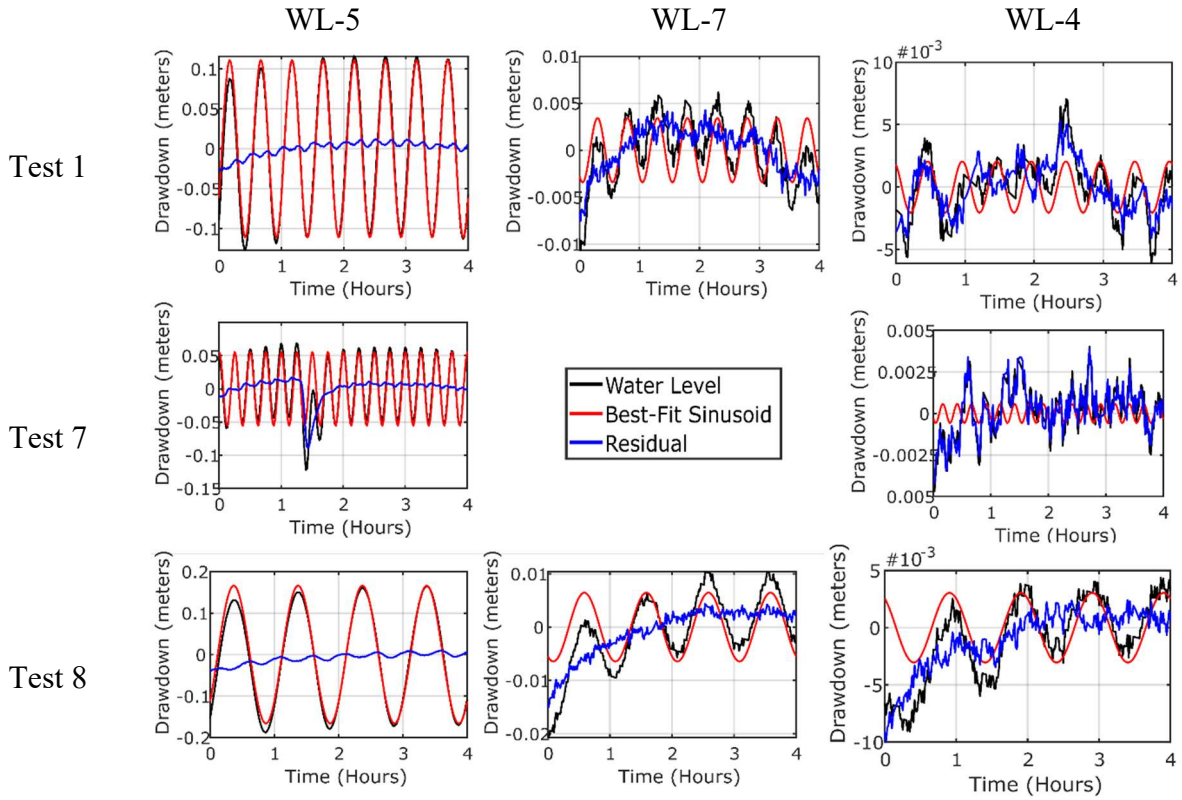

Figure 3.23: Drawdown the three piezometers for Test 1 (period = 30 min), Test 7 (period = 15 min), and Test 8 (period = 60 min). Observed head (black), best fit sinusoid (red), residual (blue). No data were recorded at WL-7 during Test 7. Field data (black), best-fit sinusoid (red), residual (blue).

The dominant period in the amplitude spectra of the pressure is the same as the pumping rate in all cases, except during Test 7 at WL-4 (Figure 3.23 and Figure 3.24). The largest amplitude during that test is 6×10^{-4} m at 18 min, and a slightly smaller amplitude occurs at a 15-minute period. The amplitudes during Test 7 at WL-4 are small (smaller than the reported accuracy of the transducer) and the largest amplitude is probably created by variations in barometric pressure. Nevertheless, there is a relatively well defined peak at the pumping period (Figure 3.23).

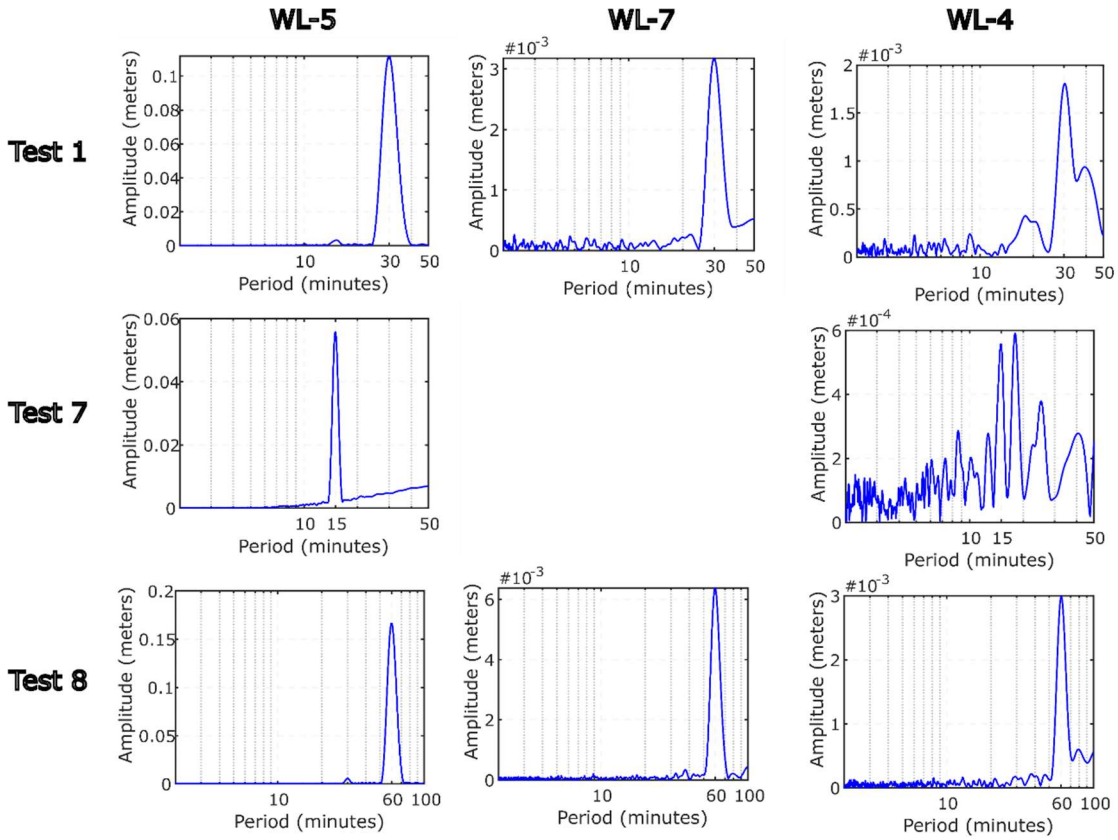

Figure 3.24: Magnitude spectrum plots of the drawdown in during the three variable period pumping tests. The pumping rate had a period of 30 minutes (Test 1), 15 minutes (Test 7), and 60 minutes (Test 8). No data were recorded at WL-7 during Test 7.

The time delay increases with distance from the pumping well, from 7.4 minutes at r = 6.7 m to 25 min at r = 20.9 m during Test 1 (Table 3.5). This gives an average gradient of the delay of 1.2 min/m. The horizontal velocity, v_{ph}, of the pressure is the inverse of the gradient, so the horizontal velocity is 0.8 m/min for the 30-minute period, l = 30 min. The gradient is steeper (approximately 2.2 min/m), and the velocity of the pressure is slower, 0.44 m/min for l = 60 min. The effect of the period on the velocity can be addressed by defining

$$\xi_\varepsilon = v_{\varepsilon h}\sqrt{\lambda} \qquad \text{(Equation 3.3)}$$

gives $3.1 < \xi_p < 5.2$ where the variation occurs in data from the different piezometers but variations in are $< \xi_p$ independent of the pumping period (Table 3.5).

Table 3.5. Amplitude and period of pressure measurements, and associated variables during periodic pumping tests of different periods.

Period, 1 (min)	Well	*r* (m)	P_h Amplitude (m)	P_h, Lag Time (min)	Velocity, v_{ph} (m/min)	$\xi_p = v_{ph}$ sqrt(l) (m/min$^{1/2}$)
15	WL-5	6.7	0.05	9.5	1.34	5.2
15	WL-7	9.1	N/A	N/A	N/A	N/A
15	WL-4	20.9	N/A	N/A	N/A	N/A
30	WL-5	6.7	0.11	7.4	0.91	5.0
30	WL-7	9.1	0.003	15.1	0.60	3.3
30	WL-4	20.9	0.002	24.6	0.85	4.7
60	WL-5	6.7	0.17	10.1	0.66	5.1
60	WL-7	9.1	0.006	23.1	0.39	3.1
60	WL-4	20.9	0.003	42.2	0.50	3.8

The lag time increases with distance from the pumping well, from 7.4 minutes at 6.7 m to 24.9 min at 20.9 m during Test 1. This gives an average gradient of 1.2 min/m. The horizontal velocity of the pressure is the inverse of the gradient. This gives a horizontal velocity of 0.8 m/min for the 30-minute period. The gradient is steeper (approximately 2.2 min/m), and the velocity of the pressure is 0.44 m/min for the 60-

minute period. The lag time during the 15-minute period test of 9.5 minutes is assumed to be an error resulting from the pressure transducer but is included for reference.

Strain Response

The effect of varying the pumping period on the strain is similar to the effect on the drawdown: increasing the period increases the amplitude of the strain and increases the ratio of signal to noise (Figure 3.25). This result is also apparent in the magnitude spectra, which are dominated by peaks at the pumping period (Figure 3.26)

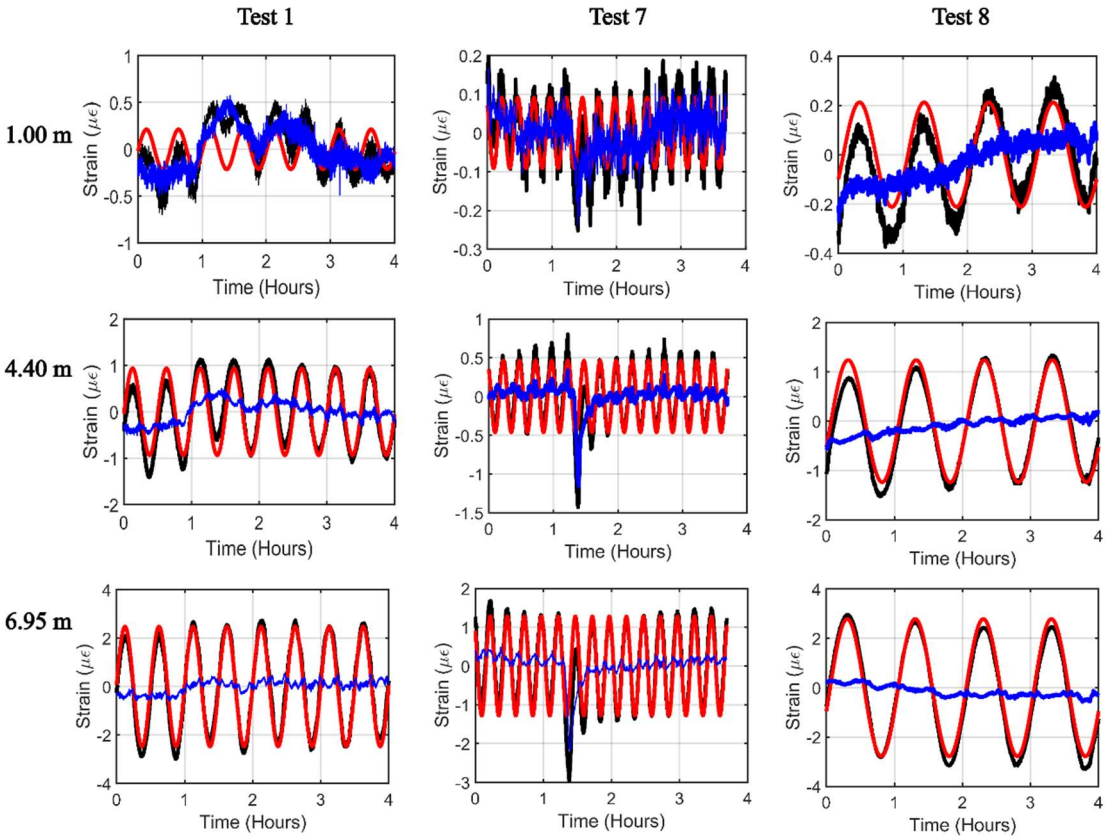

Figure 3.25: Strain response in the vadose zone during Test 1, Test 7, and Test 8 at depths (below ground surface): 1.0m 4.4m, and 6.95m. Field data (black), best-fit sinusoid (red), residual (blue).

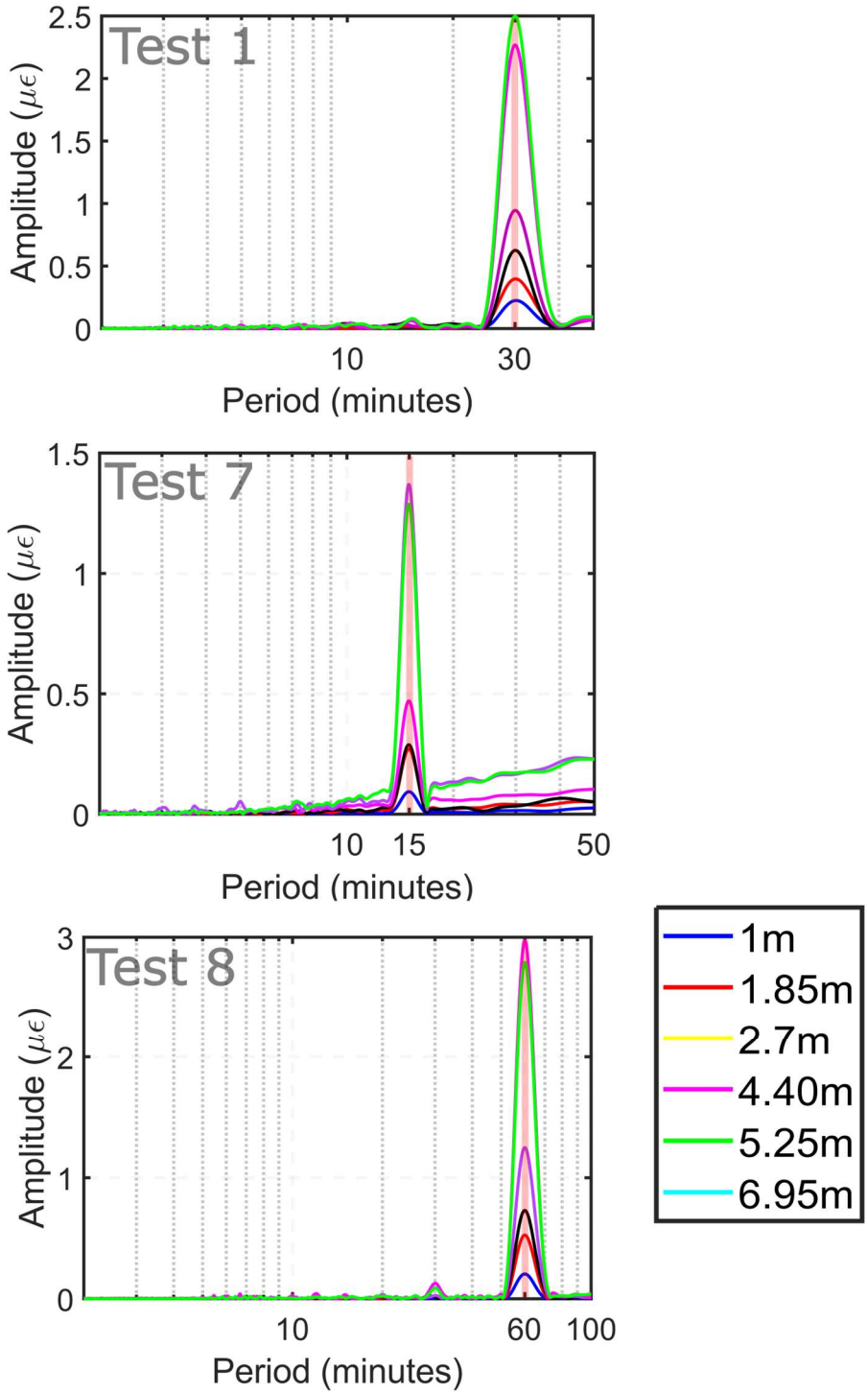

Figure 3.26: Magnitude spectrum plots of the strain at each sensor pair during pumping tests with different periods (Test 1 [30 min], Test 7 [15 min], and Test 8 [60 min]). The vertical red line represents the pumping period.

Table 3.6. Amplitudes and lag times of the strain during pumping tests of different periods.

r = 4.4m	Depth (m)	e_v Amplitude (με)	e_v, Lag Times (min)	Average Lag Time (min) +/- range (min)	Velocity, v_{eh} (m/min) +/- range (m/min)	$\xi_\varepsilon = v_{eh}$ sqrt(l) (m/min$^{1/2}$)
Test 7	1	0.09	3.49			
l=15 min	1.85	0.26	3.46			
	2.7	0.3	3.37			
	4.4	0.46	3.44			
	5.25	1.4	3.34			
	6.95	1.28	3.27	3.4 +/- 0.11	1.3 +/- .03	5.0
Test 1	1	0.21	5.07			
l=30 min	1.85	0.36	5			
	2.7	0.64	4.73			
	4.4	0.93	4.81			
	5.25	2.23	4.62			
	6.95	2.47	4.43	4.8 +/- 0.23	0.92 +/- 0.05	5.0
Test 8	1	0.21	7.54			
l=60 min	1.85	0.52	7.55			
	2.7	0.72	6.86			
	4.4	1.23	7.07			
	5.25	2.97	6.67			
	6.95	2.78	6.22	7.0 +/- 0.44	0.63 +/- 0.10	4.9

The amplitude of the strain response increases with the pumping period (Figure 3.27). The response is particularly well developed at the lower sensors where amplitude increases from approximately 1.4 mϵ to 2.9 mϵ as the period increases from 15 to 60 min. The amplitude decreases upward for the tests that used different pumping periods

(Figure 3.27) in a pattern that resembles the pattern from the tests conducted with different pumping amplitudes.

The time delay increases from 3.4 ± 0.11 min for a pumping period of 15 minutes to 7 ± 0.44 min for the 60 minutes period (Figure 3.27) and it follows that the horizontal velocity of the strain decreases from v_{eh} = 1.3 ± 0.03 m/min to v_{eh} = 0.63 ± 0.1 m/min over that range of periods.

The product of the strain velocity and the square root of the period

$$\xi_{\varepsilon} = v_{\varepsilon h}\sqrt{\lambda} \qquad \text{(Equation 3.4)}$$

is essentially constant at 5.0 m/min$^{1/2}$ (Table 3.6), which is similar to upper end of the range of values for the pressure (Table 3.5).

The time delay increases with depth, and the gradient in the vertical delay increases with the pumping period (Table 3.6). This indicates that the upward vertical velocity, v_{ev}, of the strain also decreases with the pumping period, but it is significantly faster than the horizontal velocity. For example, for a 15-minute pumping period the vertical velocity is roughly 25x faster than the horizontal velocity (v_{ev} = 33 m/min) and it slows as the period increases but it remains 7x faster (v_{ev}= 5 m/min) than v_{eh} for the 60-minute pumping period (Table 3.6).

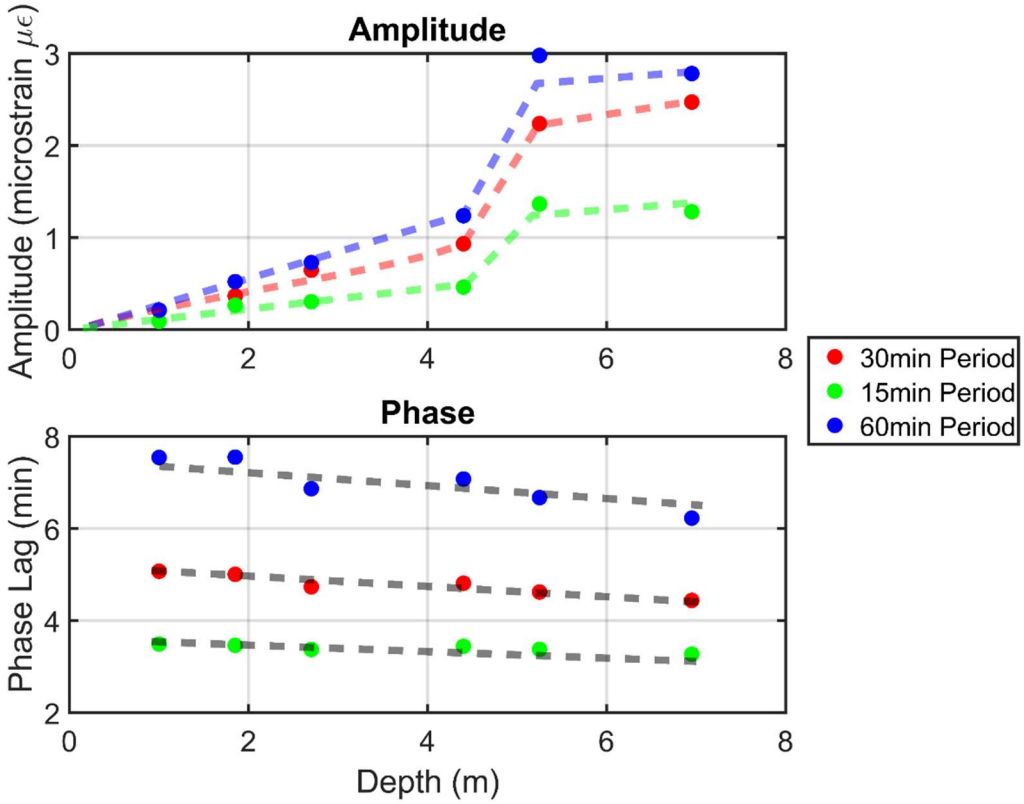

Figure 3.27: Amplitude and lag time of the strain during Test 1 (red), Test 7 (green) and Test 8 (blue). The gradients of the time delays are: -0.03 min/m (15 minutes); -0.1 min/m (30 minutes); -0.21 (60 minutes).

CHAPTER FOUR: DISCUSSION

This research demonstrated that distributed vertical strain could be measured in the vadose zone during a periodic pumping test using the newly developed CMPI optical fiber measurement system. The strain in the vadose zone shares important similarities with the pressure in the underlying aquifer. They both vary periodically with the same period as the pumping rate, and the amplitudes of both pressure and strain increase with the pumping rate. The lag times of both the pressure and strain increase with distance from the well and with the period of the pumping rate.

The amplitude and lag times of pressure in an aquifer during periodic pumping tests are commonly analyzed to estimate properties of aquifers (Rasmussen et al., 2003a), and the similarity between pressure and strain suggests that it may also be feasible to estimate aquifer properties using strain data.

Table 4.1: Summary of D_h values calculated using delay time of pressure (P), strain at 6.95 m (S1), strain averaged over all depths (S2), calculated using either the Rasmussen (R) or Streltsova (S) solutions. D_h also estimated from a constant rate pumping test (PC). Values in parentheses are standard deviations.

			Diffusivity [m^2/s]		
Pumping Test	Location	id	Neuman	Rasmussen (R)	Streltsova (S)
Constant Rate	All Piezometer		0.039		
Test 1 30-minute period	WL-5	P		0.051	0.031
	WL-7	P		0.03	0.023
	WL-4	P		0.033	0.028
	Average (std dev)			0.036 (0.011)	0.027 (0.004)
	Strain @ 6.95m	S1		0.01	0.042
	Strain average	S2		0.082 (0.01)	0.036 (0.003)
Test 7 15-minute Period	WL-5	P		0.011	0.01
	WL-7	P		0.181	0.119
	WL-4	P		-	-
	Average (std dev)			0.096 (0.12)	0.065 (0.07)
	Strain @ 6.95m	S1		0.07	0.038
	Strain average	S2		0.062 (0.004)	0.035 (0.001)
Test 8 60-minute period	WL-5	P		0.071	0.033
	WL-7	P		0.027	0.02
	WL-4	P		0.023	0.019
	Average (std dev)			0.040 (0.026)	0.024 (0.008)
	Strain @ 6.95m	S1		0.153	0.042
	Strain average	S2		0.109 (0.03)	0.034 (0.02)
	Constant Rate	D	**0.039**		
	Ave (std dev) A	P		**0.053 (0.05)**	**0.035 (0.03)**
	Ave (std dev) B	S1		**0.078 (0.07)**	**0.041 (0.002)**
	Ave (std dev) C	S2		**0.08 (0.022)**	**0.035 (0.001)**

To evaluate this suggestion, pressure and strain lag time data were compiled from three periodic tests that used different periods (Test 1, Test 7, and Test 8) and analyzed to calculate D_h in Table 4.1 using the solutions from Rasmussen et al. (2003; Equation 2-18)

and from Streltsova (1988; Equation 2.21). D_h was calculated using lag time at each piezometer, and these data were averaged, and it was also calculated using strain measured at the bottom sensor pair on the strain ribbon (at 6.95 m depth) and using average time delay of the strain over the six sensor pairs (Table 4.1). The strain lag time decreased with depth, so D_h calculated using the average is less than D_h calculated using the strain at the bottom of the vadose zone. The hydraulic diffusivity estimated by fitting data from all three monitoring wells measured during a constant rate pumping test to the Neuman (1973) solution served as a baseline.

The average hydraulic diffusivity across all tests using pressure data and the Rasmussen solution is 0.053 (0.05) m^2/s, where the standard deviation is given in parentheses. The average D_h value using pressure and the Streltsova solution is 0.035 (0.03) m^2/s, which is less than that calculated using the Rasmussen solution but the two average values are withing one standard deviation of each other so the null hypothesis that there is no significant difference between the means was tested using a two-tailed, paired Student t-test. The result of comparing the two means is $p = 0.10$, so we would accept the null hypothesis assuming a critical value of $p = 0.05$.

There is no statistical difference between D_h calculated using pressure (P-R or P-S) and values calculated using time delays from strain, assuming $p < 0.05$ is a significant difference (first two rows in Table 4.2) except for between P-S and S2-R where $p = 0.03$. The case with the most significant difference between D_h values ($p = 0.02$) is between *S1* (strain averaged over the different locations) and P-CRS (pressure during constant rate test that analyzed the three piezometers simultaneously). This low p value occurs

because the three values determined using strain are remarkably consistent ($\sigma = 0.001$), and only one value of D_h for P-CRS is used. However, the average value of D_h from *S2* is only a few percent different from the D_h value from P-CRA, so this approach for comparing results to D_h from a constant rate test may be too conservative. An alternative approach is to use the values of D_h determined by analyzing data from the three monitoring wells during the constant rate tests individually. This gives a value of D_h for each of the three piezometers. *p* values were calculated using this dataset and the results are in column P-CRI in Table 4.2. All the values of D_h calculated using pressure or strain from the periodic tests are essentially the same as D_h values calculated from the constant rate test, according to p values determined using P-CRI in D_h Table 4.2 (rightmost column).

Table 4.2. Summary of average and standard deviations of Dh from pressure (P) and strain at 6.95m (S1) and average strain (S2) lag time calculated using solutions in Rasmussen (R) and Streltsova (S). P-CR is calculated from pressure data measured during a constant-rate tests in upper three rows. P values giving probability comparing means of different data sets in lower six rows. Bold fonts highlight $p < 0.05$, grey font highlights $p > 0.1$.

	P-R	P-S	S1-R	S1-S	S2-R	S2-S	P-CRA	P-CRI
average	0.053	0.035	0.078	0.041	0.083	0.035	0.039	0.070
std dev	0.055	0.035	0.072	0.002	0.021	0.001		0.056
P-R		*0.05*	0.63	0.53	0.28	0.37	0.48	0.69
P-S			*0.42*	0.68	**0.03**	0.98	0.78	0.40
S1-R				0.47	0.91	0.41	0.45	0.89
S1-S					*0.07*	**0.04**	0.34	0.46
S2-R						*0.06*	*0.07*	0.40
S2-S							**0.02**	0.44

Analysis of a Pressure and Strain While Pumping a Well at a Sinusoidal Rate

The data analyzed above indicates that delay times of strain in the vadose zone are similar to the delay of pressure in the underlying aquifer at the same radial distance (Table 3.5 and Table 3.6), and this leads to similar estimates of D_h (Table 4.1 and Table 4.2) . That result suggests that under the conditions of the field test, strain measured in the vadose zone could be used to estimate D_h in the underlying aquifer, but the field data are only available for the vertical component of strain measured at one radial distance so the generality of this result is unclear. Simulations were conducted of an idealized representation of the field site to further evaluate this effect.

Simulations used two rectangular domains in axial symmetry where the physics in each domain are related, but different. The lower domain includes fluid flow through porous media and deformation coupled through poroelasticity and it represents the aquifer. The upper rectangular domain is the vadose zone. It includes elastic deformation, but the fluid pressure is assumed to be constant. This is justified for short well tests because the relative liquid phase permeability in the vadose zone would limit upward pressure diffusion from the aquifer, and the air phase would create a highly compressible pore fluid that would limit pressure changes due to deformation. We have conducted simulations where fluid pressure in the vadose zone is allowed to change as represented by the Richards equation. Results of the model using Richards equation shows that pressure changes in the lower part of the vadose zone can be affected by pressure changes in the underlying aquifer, but those changes are small and limited to the lower few meters so they will be ignored here.

The thickness of the aquifer and vadose zones are both 10 m, which is similar to the field site, and the lateral extent is 10 km, which is large enough to eliminate effects of lateral boundaries. Other boundary conditions for the fluid and displacements are standard and summarized in Figure 4.1.

The well is represented using a boundary condition that includes wellbore storage. This is accomplished by assuming water volume is conserved in a wellbore of finite volume, where the diameter is assumed to be 0.0762 m based on field conditions. The hydraulic head is assumed to be uniform over a fully penetrating well screen, and the head in the well bore is above the top of the screen so the change in head is equal to the change in storage in the well bore.

The pumping rate varies periodically, starting with a pumping stage followed by an injection stage of equal rate, but opposite sign (Figure 4.2). This gives a net pumping rate of zero after every completed sinusoidal cycle of pumping and injection. Changes in wellbore storage cause the flowrate leaving the wellbore and entering the aquifer to be less than the pumping or injection rate, particularly early in a pumping or injection cycle (red line in Figure 4.2). The hydraulic head in the well drops with time during the pumping cycle and reaches a minimum at the end of the pumping stage. It then increases and reaches a maximum at the end of the injection stage (blue line in Figure 4.2).

The pumping rate and wellbore pressure are both sinusoids with the same period, and in the absence of wellbore storage the wellbore pressure will lag behind the pumping rate by $3\pi/2$, or 3/4 of the period, λ (Streltsova, 1988). This difference in time occurs because the head in the well drops whenever the pumping rate is positive, so the peak

pressure occurs at the end of the pumping stage. Wellbore storage causes the flow at the well screen to lag behind the flow from the pump (Figure 4.2), and this causes the wellbore pressure to lag further than $3\pi/2$ behind the pumping rate. This causes problems when using the pumping rate as a reference for the delay time. The pressure head in the wellbore can be easily measured in the field, so it will serve at the baseline time for calculating time delay in both the simulations and the field data analysis.

The pressure and strains vary periodically at reference points in the aquifer and vadose zone (Figure 4.3). The signs of the pressure and most of the strains are generally similar, so an increase in pressure occurs with an increase in strain, which implies that the strain is becoming increasingly tensile at an overlying point. The exception is the vertical strain, which decreases when the pressure increases. The delays of pressure and strain components all increase with distance from the well, and this is manifested by a delay in the time when the maxima or minima occur in the time series (Figure 4.3). Even though they share similar general characteristics, the shapes, magnitudes and delays of each strain component are distinct from each other and from the pressure (Figure 4.3).

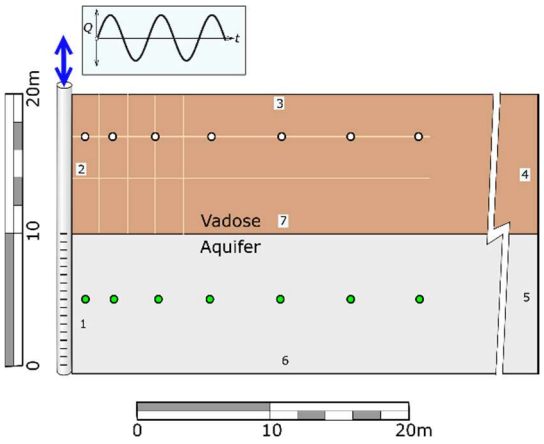

Figure 4.1. Conceptual model of simulation in axial symmetric coordinates with a well at the axis. Pressure analyzed in the aquifer. Pressure assumed constant in vadose. Strain occurs everywhere and is coupled to the fluid pressure in the aquifer. Light colored lines in vadose zone are section lines used for plotting. White circles are locations of strain and green circles are location of pressure time series. Boundary conditions for pressure and mechanics: (1) periodic flux as shown in inset from wellbore with storage, normal traction equal to pressure; (2) zero normal displacement (roller); (3) zero normal traction (4) roller @ r = 10km (5) roller, specified head @ r = 10km (6) no flow, roller (7) no flow, continuity.

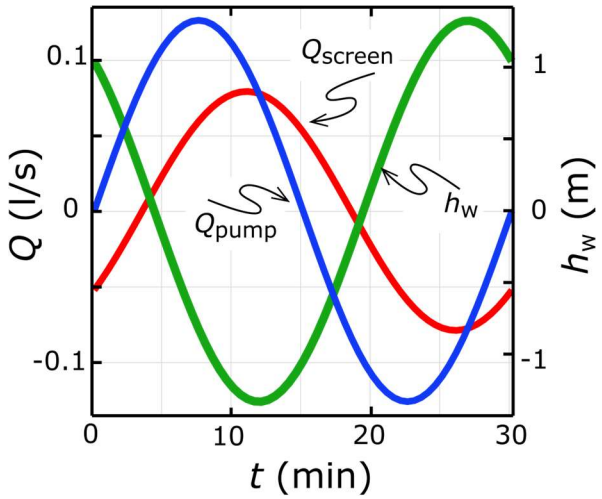

Figure 4.2. Flowrate and pressure at the wellbore. The flowrate pumped from the well (Q_{pump}) is a sinusoid with zero net rate. The flowrate through the well screen (Q_{screen}) is exchanged between the well and the aquifer. It differs from the Q_{pump} because of wellbore storage.

The strain tensor field at the end of the injection stage, ranges from roughly -10 με to 1 με and each component forms a unique pattern (Figure 4.4). The maximum strains are in the lower left corner, slightly above the well screen, and they decrease upward and radially within approximately 5 m of the well. In the mid-distance of $5 < r <$ 15m, the strains decrease in approximately a horizontal direction (the contours are

roughly vertical). At larger radial distances the strains decrease downward. Both the vertical and radial strains, and the horizontal average strain change sign with distance (the thick red line is zero strain, but the sign of the circumferential strain is positive throughout the domain in Figure 4.4.

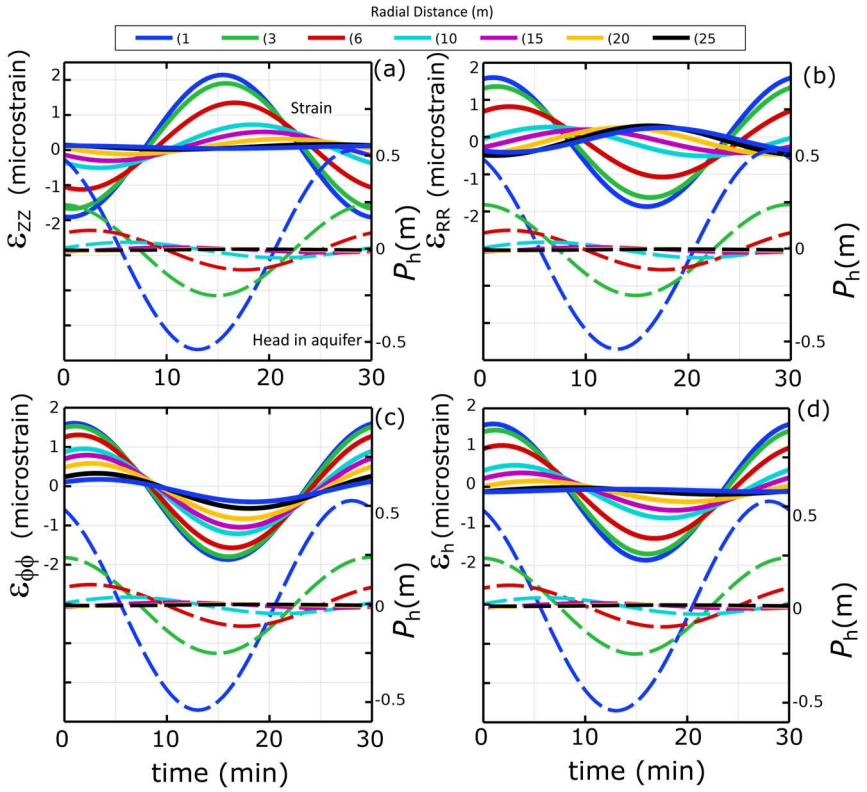

Figure 4.3. Strain components (solid lines) at reference points at different radial distances indicated by color in the vadose zone (z = -3m) and hydraulic heads (dashed lines) in the aquifer (z = -15m) at radial distances indicated by color. Sinusoidal pumping with a period of 30 min. Reference points in Figure 4.1.

A unifying pattern emerges that appears to persist in the strain field throughout a sinusoidal well test (Figure 4.4). In general, there are four regions in the vadose zone where the direction of decreasing strain are consistent, whereas the direction of decreasing pressure is always horizontal away from the well in the aquifer (Figure 4.5).

Strain decreases upward in the Near Well region, whereas it decreases in a horizontal direction in the Shallow and Mid-Distance regions. Strain decreases downward in the region that is far from the well (Figure 4.5).

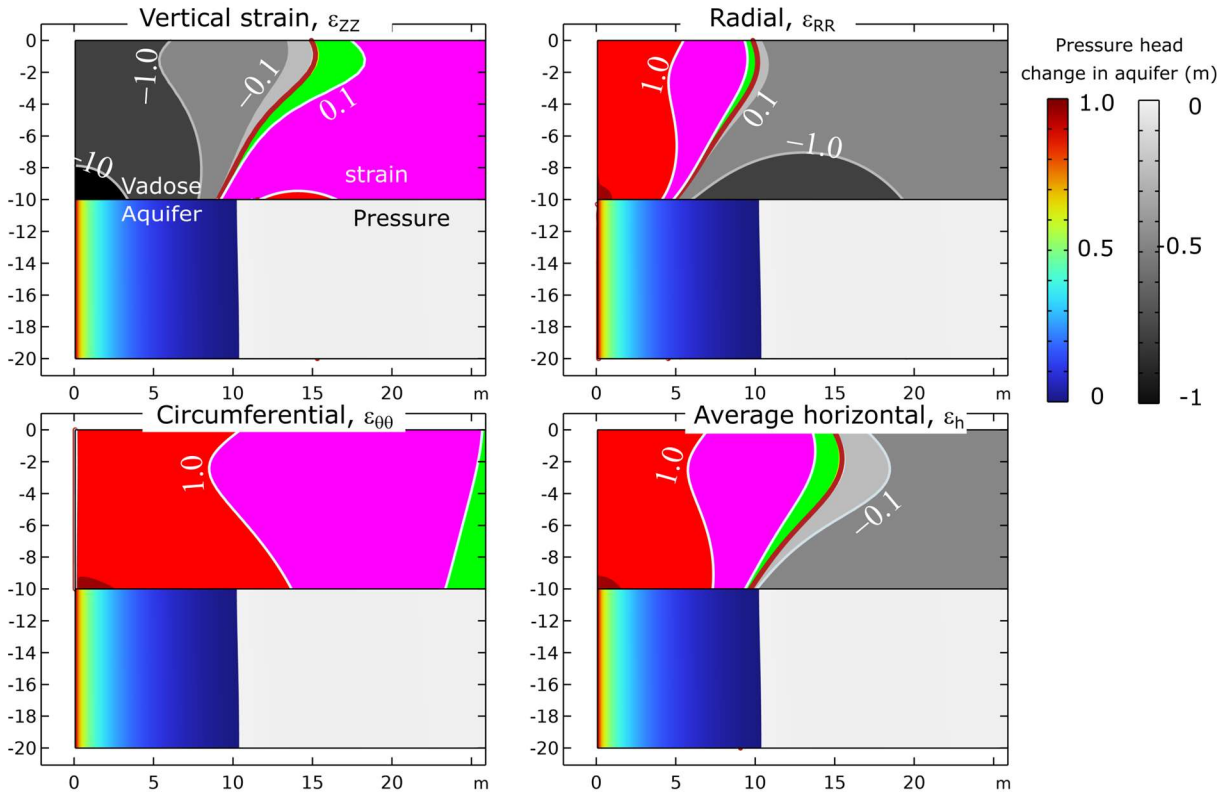

Figure 4.4. Strain components in the vadose zone (labeled in units of microstrain) and hydraulic head change in the aquifer in cross-section at the end of the injection stage of a sinusoidal cycle. Negative strain is compression and is shown in grey tones, positive strain is tension and shown as colors. Sinusoidal pumping with a period of 30 min.

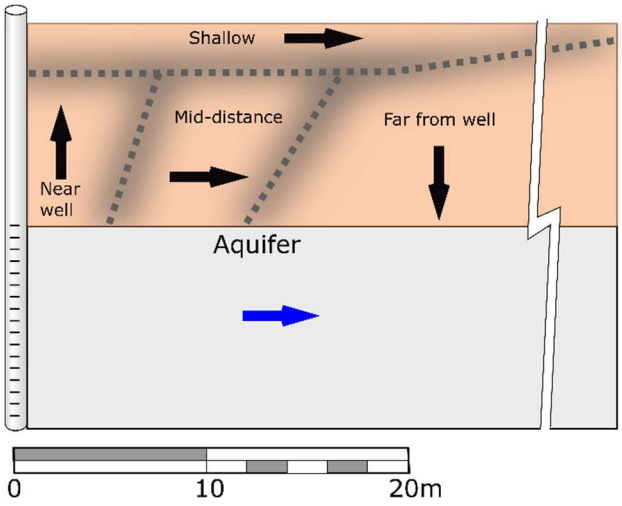

Figure 4.5. Conceptual model of regions of different hydraulic head and strain gradients in the vadose zone and aquifer. Arrows show direction of decreasing strain (black) or hydraulic head (blue).

Delay times

Phase delays of the strain components in the vadose zone were calculated using a Fourier transform. The phase of the pressure at the well face was taken as zero and phases were converted to time delay following the pressure. A half period was added to the phase of ε_{zz} to facilitate plotting with the other strains.

The delay of the pressure increases as a roughly linear function of distance from the well (blue lines in Figure 4.6). The delay of the vertical and average horizontal strains, ε_{ZZ} and ε_h, at shallow depth (3m) in the vadose zone are non-linear functions of distance, but they cross the delay of the pressure at two locations and they are generally within 20 percent of the delay of the pressure within 25 m of the well (Figure 4.6a). The delay of the circumferential strain $\varepsilon_{\phi\phi}$ is

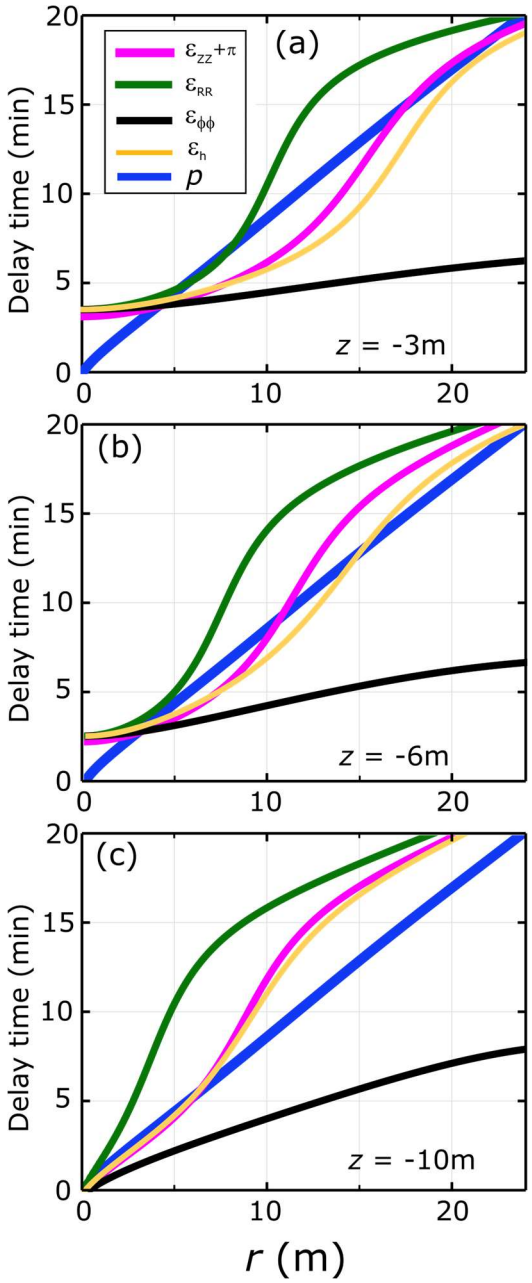

Figure 4.6. Delay time of the strain and pressure behind the pressure in the well along horizontal lines at different depths. Pressure measured at mid-height in aquifer. (a) strain at 3m depth and (b) strain at 6m depth. (c) strain at 10m depth, which is the bottom of vadose zone. Sinusoidal pumping with a period of 30 min.

significantly less than, and the delay of the radial strain ε_{RR} is significantly greater than the pressure delay. This suggests that the pressure delay in the aquifer could be estimated to within roughly 20 percent using the delay of ε_{ZZ} or ε_h measured at shallow depth in the vadose zone.

The delays of the ε_{ZZ} and ε_h are similar to the delay of p at mid-depth and near the bottom of the vadose zone in proximity to the well, although at $r > 8$m the delays for those strains at the bottom of the vadose zone exceeds that of the pressure (Figure 4.6b and c). The simulation used here assumes the pressure change in the aquifer is isolated from the vadose zone, whereas in most cases a pressure change in the aquifer is expected to propagate upward into the overlying vadose zone. This will affect the strains in the vadose zone, particularly at the bottom of the vadose zone. The strains shown in Figure 4.6c do not include this effect.

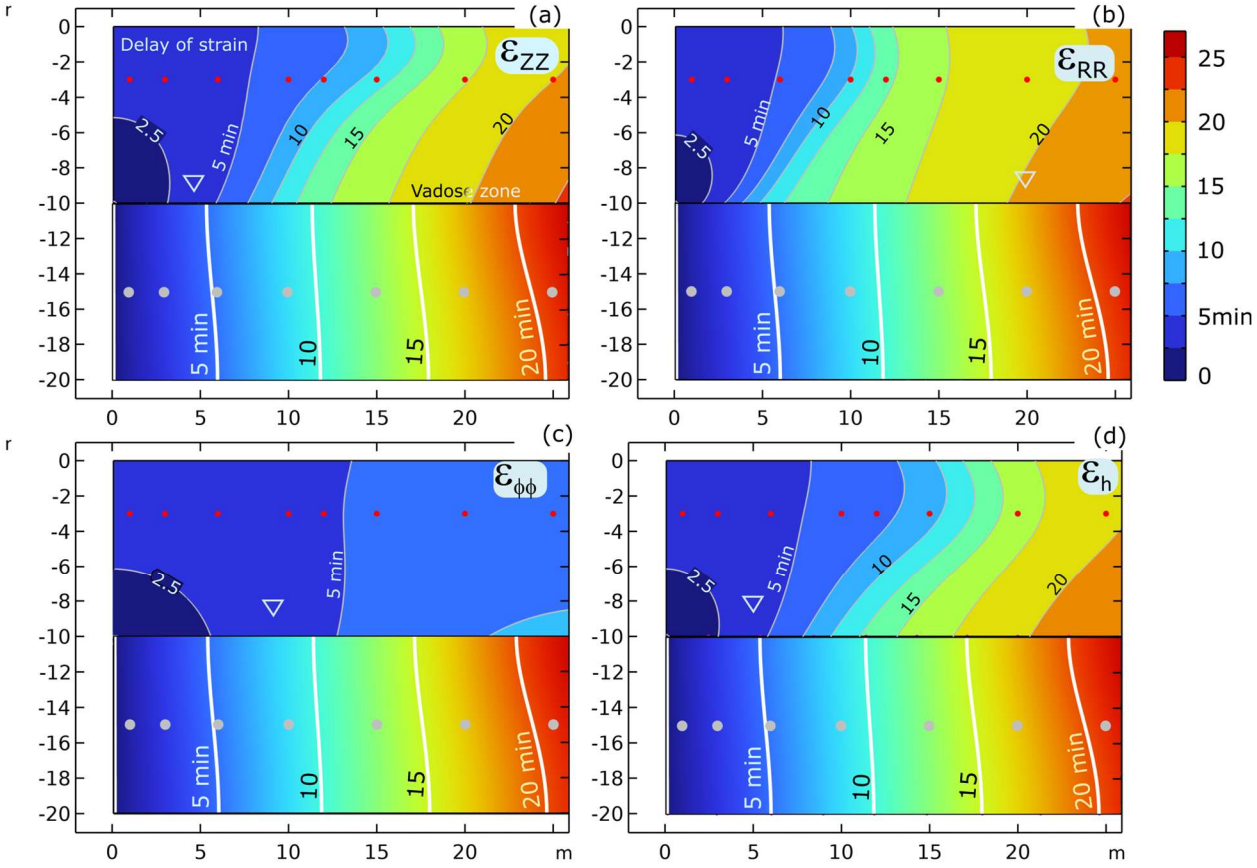

Figure 4.7. Delay of the pressure and different strain components in minutes behind the pressure at the well face for simulations that used a period of 30 min. Delay of strain in the vadose zone with filled contours, delay of pressure in aquifer with color flood. Dots are locations of time series in Figure 4.1.

Phase velocity

The patterns of the delays of the strain components are broadly consistent, but each one is distinct from the others (Figure 4.7). The delays generally increase upward and horizontally from a point in the vadose zone closest to the well screen (r = 0.1, z = -10m). This gives rise to upward phase velocities within a few meters of the well (Figure 4.7). Contours of the delays are roughly vertical in the range of 6 < r <10m, and they

curve upward and outward away from the well at greater radial distances (Figure 4.7 and Figure 4.8).

The phase velocity of the strain is normal to the contours shown in Figure 4.7, and this supports the general conceptual model in Figure 4.5. The horizontal phase velocity of the pressure is 1.2 m/min, according to Figure 4.6. This is slightly larger than was observed in the field (0.9 m/min). The horizontal phase velocity determined using delay measurements of strain in the vadose zone will be within approximately +/- 20% of the phase velocity of the pressure. At $3 < r < 6$ m from the well, the delay times of the strain at shallow depth are essentially the same as the delay times of the pressure in the underlying aquifer. This explains the similarity in delay times, and D_h values, between the vertical strains at $r = 4.4$m and the pressure in the field data (Tables 3.5 and 3.6).

The upward velocity of the ε_{zz} is approximately 3 m/min at $r = 2$m, and it increases to 6 to 9 m/min at $r = 4$m. It is downward at -0.6 m/min at $r = 14$m. The delay is slightly variable, but essentially independent of depth at $r = 8$m (Figure 4.8). Velocity is the inverse of the gradient in Figure 4.8, which implies that the phase velocity is large, and it changes sign at $r \sim 8$m.

Implications

The simulations explain the field data and provide some insights into relationships between pressure and strain. In general, but the time delay of ε_{zz} and ε_h are similar (within 20%) of the delay time of the pressure in the underlying aquifer (Figure 4.6 and Figure 4.7). ε_{zz} can be measured using a strain ribbon and the CMPI technique, as we showed here. We expect that other methods of measuring strain with optical fibers, using

distributed acoustic sensing, for example, could also be used with the strain ribbon to measure vertical strains in the vadose zone. It is feasible to measure ε_h using cylindrical strainmeters that are pushed into vertical borings made with a direct-push drilling rig and recovered after testing. This means that it should be straightforward to measure ε_{ZZ} and ε_h.

The delay times of ε_{RR} and $\varepsilon_{\phi\phi}$ differ significantly from the underlying strain, so they would be less useful as surrogates for pressure. However, the relative magnitudes of the horizontal strains will be sensitive to the location and orientation of perturbations in the underlying pressure caused by aquifer heterogeneities. As a result, we expect that these components of the strain tensor will also be useful in characterizing aquifers during periodic well tests.

Although the delay times for ε_{ZZ} and ε_h are similar to the delay times for pressure in the underlying aquifer, the time are by no means the same. This is because the pressure propagates radially at approximately a uniform velocity, whereas the strain in the vadose zone follows a more circuitous route, propagating upward near the well, horizontally at mid distance and downward at a larger distance where the pressure in the underlying aquifer as largely decayed (Figure 4.5). Upward propagation causes the delay times of the strain to be less than the pressure close to the well (r < 3m in Figure 4.6). The strain speeds up and propagates faster than the pressure resulting in delay times that are less than pressure in the mid-distance. These effects occur because the vadose zone is deformed by the aquifer expanding both outward and upward when the pressure in the aquifer is increasing, and contracting inward and downward when the pressure is

decreasing. These effects are manifested in patterns of different strain components that are complex (Figure 4.4), but that can be readily simulated using poroelastic analyses. This suggests that measurements of ε_{zz} and ε_h in the vadose zone during periodic well tests can be using directly with the analytical solutions of Streltsova or Rasmussen to provide an approximate estimate of D_h, and then numerical inversion of poroelastic simulations can be used to refine those estimates and potentially identify heterogeneities or other features not included in the analytical solutions.

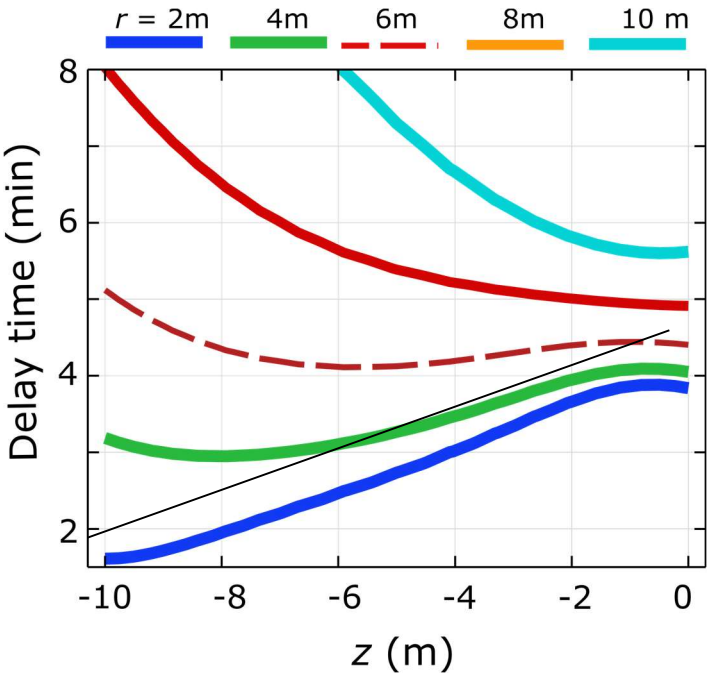

Figure 4.8. Delay of strain as function of depth along vertical lines at different radial distances (legend). Positive slope indicates strain advancing upward, negative indicates strain advancing downward. Phase velocity of the strain at r = 2m is 2 m/min, and phase velocity at r = 14m is –0.6 m/min.

Installation Procedure and Sinusoidal Pumping System

The data outlined above indicate that the installation procedure developed for this research was successful in the saprolite soils at the field site in Pendleton South Carolina. The strain ribbon was installed and verified using known point load applied at the surface of the ribbon and vertical strain was measured during these loading tests.

Numerous ribbons were attempted to be installed during the field installation portion of this research. Some ribbons were subsequently broken during installation or shortly after because of damage sustained to the optical fiber itself. Through the processes of developing and installing the strain ribbon, the technique presented in this research was the most successful and practical for coupling the strain ribbon to this saprolite formation. The polyethylene sleeve diameter was slightly larger than the borehole diameter to ensure full contact between the borehole walls and the sleeve. If the polyethylene sleeve diameter was less than the borehole, the strain ribbon might not adequately couple to the formation and not function as expected. Additionally, the polyethylene sleeve was pressurized with air prior to filling with sand to prevent bridging and ensure proper coupling.

A system was also developed which allowed a 4-inch, 0.5 horsepower well pump to be controlled sinusoidally. The pump's power was connected to a variable frequency drive which varied the amount power supplied to the pump. By varying the power to the pump, it was possible to control the flow rate. The VFD was able take the input of a sinusoidal function generator and convert that to a voltage provided to the pump.

Through this technique, different periods and different amplitudes of flow rate were achieved during the testing period.

Other Applications

It should be noted however that the strain lag time observed and used in this experiment is restricted to measurements located close to the pumping well. The results may be different, especially at different depths, for strain measured at greater radial distances from the well.

A method has yet to be investigated on using the vertical amplitude attenuation of strain to estimate the physical properties of the vadose zone. These properties would also be affected by other inputs on the system such as but not limited to pore pressure, soil type, barometric pressure, and temperature.

CHAPTER FIVE: CONCLUSION

The objective of this project was to evaluate the feasibility of measuring and interpreting the vertical strain in the vadose zone generated during a sinusoidal rate pumping test to estimate aquifer properties Eight sinusoidal-rate well tests were performed using different amplitudes and periods at a field site underlain by saturated saprolite in Pendleton, SC, and a constant-rate pumping test was also performed as a baseline. Pressure in the aquifer was measured at three piezometers and strain was measured along optical fiber sensors distributed vertically in the vadose zone (Figure 2.9 and Figure 2.10). Strain was measured using a novel optical method called Coherence-length gated Microwave Photonics Interferometry (CMPI).

The pressure and the vertical strain varied with the same period as the pumping rate, and the delay times between the pumping rate and the pressure and strain increased with distance from the well (Figure 3.17 through Figure 3.19 and Figure 3.23; Table 3.5 and Table 3.6). The horizontal phase velocity (ratio of radial distance/lag time) of the pressure and the strain at similar radial distances both decreased from 1.3 m/min to 0.6 m/min as the pumping period increased from 15 to 60 minutes. The ξ term (product of the horizontal phase velocity and the square root of the period) is approximately $\xi_p \approx \xi_\varepsilon \approx 5.0$ m/min$^{1/2}$ across all periods for both pressure at r = 6.7 m and strain at r = 4.4 m. The ξ for pressure at two other monitoring wells at further radial distances is slightly less, $3.1 < \xi < 4.7$ m/min$^{1/2}$ (Table 3.5 and Table 3.6).

The periodic characteristics of vertical strain at the selected measurement location in the vadose zone are similar to the characteristics of pressure in the aquifer. The

hydraulic diffusivity of a uniform, confined aquifer is proportional to ξ^2, so the hydraulic diffusivity determined using pressure in the aquifer is similar to that estimated using strain in the vadose zone (Table 4.1). Hydraulic diffusivity was also calculated using the constant-rate pumping test, and Student t-tests were used to compare the different values. The results indicate that there is no statistical difference between the hydraulic diffusivities measured by analyzing pressure in the aquifer and strain in the vadose zone (Table 4.2).

The field data suggest that it may be feasible to use calculations developed for pressure in an aquifer to estimate aquifer properties using strain measured in the vadose zone, but field measurements of strain were only available at one location (r = 4.4m) so the field data were unable to evaluate how widely the relationship between pressure and strain might hold. Simulations of pressure and strain were conducted using a poroelastic analysis to evaluate this issue. The simulations predict an upward phase velocity of the strain (Figure 4.8), and the lag times of the strain and pressure are nearly identical at r = 4.4m (Figure 4.6). Both of these predictions are consistent with the field data, which gives some confidence that the simulations generally represent field conditions. The lag time of the strain varies both vertically and radially in the vadose zone (Figure 4.7). The lag times of the strain differ from those of the underlying pressure, but the two differ by less than 20 percent and in two zones the lag times are identical for the conditions of the field site (Figure 4.6).

These findings indicate that hydraulic diffusivity estimated using the lag times for pressure in a uniform confined aquifer would be within 40 percent of values estimated

using lag times and radial distance of strain in the vadose zone. This would serve as a valuable initial estimate of aquifer properties in many applications. Numerical inversion of strains simulated in the vadose zone provide an important path forward to further refine estimates of aquifer properties.

This result is significant because deploying strain sensors at shallow depths will require less drilling than installing monitoring wells. As a result, several shallow strain sensors could be deployed instead of one deep monitoring well, refining the spatial resolution during aquifer characterization. This could improve the definition of aquifer heterogeneities, which play important roles in a wide range of operations involving resource recovery, storage of wastes, and environmental remediation. The CMPI technology used to measure strains for this research has particularly high spatial and strain resolution, which was important for obtaining the strain data. CMPI technology is not currently commercially available, but a wide variety of other optical fiber strain sensors are available, and optical fiber strain sensing technology is evolving quickly, so it is reasonable to expect that the technology needed to make strain measurements like the ones described here will be available. The strain ribbon approach used to couple the optical fiber strain sensor to the formation (Figure 2.4) should be readily extended to other optical fiber sensing methods. Alternative approaches are under development that use strain sensing instruments that can be deployed temporarily and then retrieved and reused, and they will provide another option for measuring strain signals during well tests.

REFERENCES

Bibliography

Agnew, D. C. 2007. "Earth Tides." In *Treatise on Geophysics*, 163-195: Elsevier B.V.

Black, J. and K. Kipp. 1981. "Determination of Hydrogeological Parameters using Sinusoidal Pressure Tests: A Theoretical Appraisal." *Water Resources Research* 17 (3): 686-692.

Bredehoeft, J. D. 1967. "Response of Well-Aquifer Systems to Earth Tides." *Journal of Geophysical Research (1896-1977)* 72 (12): 3075-3087.

Butler, J 1997. *The Design, Performance, and Analysis of Slug Tests*.

Butler, J and J. Healey. 1998. "Relationship between Pumping-Test and Slug-Test Parameters: Scale Effect Or Artifact?" *Ground Water*.

Cardiff, M. and W. Barrash. 2015. "Analytical and Semi-Analytical Tools for the Design of Oscillatory Pumping Tests." *Groundwater* 53 (6): 896-907.

Cartwright, D. E. and R. J. Tayler. 1971. "New Computations of the Tide-Generating Potential." *Geophysical Journal International* 23 (1): 45-73.

Cleveland, T., R. Bravo, and J. Rogers. 1992. "Storage Coefficients and Vertical Hydraulic Conductivities in Aquitards using Extensometer and Hydrograph Data." *Ground Water* 30 (5): 701-708.

Cooper, H. H., J.D. Bredehoeft, I.S. Papadopulos, and R. R. Bennett. 1965. "The Response of Well-Aquifer Systems to Seismic Waves." *Journal of Geophysical Research (1896-1977)* 70 (16): 3915-3926.

Cooper, Hilton H., J.D. Bredehoeft, and I.S. Papadopulos. 1967. "Response of a Finite-Diameter Well to an Instantaneous Charge of Water." *Water Resources Research* 3 (1): 263-269.

Cutillo, P.A. and J.D. Bredehoeft. 2011. "Estimating Aquifer Properties from the Water Level Response to Earth Tides." *Groundwater* 49 (4): 600-610

Davis, S., F. Peterson, and A. Halderman. 1969. "Measurements of Small Surface Displacements Induced by Fluid Flow." *Water Resources Research* 5 (1): 129-138.

Dietz, D.N. 1943. "De Toepassing Van Invloedsfuncties Bij Het Berekenen Van De Verlaging Van Het Groundwater Ten Gevolge Van Wateronttrekking." *Water 27 (6): 51* 57.

Ferris, J. 1952. "Cyclic Fluctuations of Water Level as a Basis for Determining Aquifer Transmissibility."

Ferris, J., D. Knowles, R. Brown, and R. Stallman. 1962. "Theory of Aquifer Tests." .

Fokker, P.A., E.S. Borello, F. Verga, and D. Viberti. 2018. "Harmonic Pulse Testing for Well Performance Monitoring." *Journal of Petroleum Science and Engineering* 162: 446-459.

Hantush, M.S. 1959. "Analysis of Data from Pumping Wells Near a River." *Journal of Geophysical Research (1896-1977)* 64 (11): 1921-1932.

Horne, R.N. and A.J. Rosa. 1997. "Reservoir Description by Well Test Analysis using Cyclic Flow Rate Variation." *SPE Formation Evaluation* 12 (4): 247-254.

Hsieh, P. and J. Bredehoeft. 1987. "Determination of Aquifer Transmissivity From Earth Tide Analysis." *Water Resources Research* 23 (10): 1824-1832.

Hua, L., Y. Song, B. Cheng, W. Zhu, Q. Zhang, and H. Xiao. 2017. "Distributed Optical Fiber Sensing Based on Coherence-Length Gated Microwave Photonics Interferometry.".

Hua, L., X. Zhu, S. DeWolf, J. Lei, Q. Zhang, L. Murdoch, and H. Xiao. 2020. "Phase Demodulation by Frequency Chirping in Coherence Microwave Photonic Interferometry." *IEEE Journal of Selected Topics in Quantum Electronics* 27 (2): 1-9.

Jacob, C. E. 1947. "Drawdown Test to Determine Effective Radius of Artesian Well." *Transactions of the American Society of Civil Engineers* 112: 1047-1067.

Jacob, C. E. 1940. "On the Flow of Water in an Elastic Artesian Aquifer." *Eos, Transactions American Geophysical Union* 21 (2): 574-586.

Johnson, C. R., R. A. Greenkorn, and E. G. Woods. 1966. "Pulse-Testing: A New Method for Describing Reservoir Flow Properties between Wells." *Journal of Petroleum Technology* 18 (12): 1599-1604.

Kantha, L. 2006. "Time to Replace the Saffir-Simpson Hurricane Scale?" *Eos, Transactions American Geophysical Union* 87 (1): 3-6.

Kasich, J., M. Taylor, and C. Butler. 2018. *Technical Guidance Manual for Hydrogeologic Investigations and Ground Water Monitoring: Pumping and Slug Tests*.

Kruseman, G.P. and N. de Ridder. 1994. *Analysis and Evaluation of Pumping Test Data*. International Institute for Land Reclamation and Improvement : ILRI Publication. 2. ed., (completely rev.), reprinted ed. Vol. 47. Wageningen: ILRI.

Kudryavtsev, S. M. 2004. "Improved Harmonic Development of the Earth Tide-Generating Potential." *Journal of Geodesy* 77 (12): 829-838.

Kuo, C. H. 1972. "Determination of Reservoir Properties from Sinusoidal and Multirate Flow Tests in One Or More Wells." *Society of Petroleum Engineers Journal* 12 (06): 499-507. doi:10.2118/3632-PA.

Malama, B., K.L. Kuhlman, R. Brauchler, and P. Bayer. 2016. "Modeling Cross-Hole Slug Tests in an Unconfined Aquifer." *Journal of Hydrology* 540: 784-796.

Mehnert, E., A. J. Valocchi, M. Heidari, S. G. Kapoor, and P. Kumar. 1999. "Estimating Transmissivity from the Water Level Fluctuations of a Sinusoidally Forced Well." *Ground Water* 37 (6): 855-860.

Melchior, P. J. and M. Toba. 1978. *The Tides of the Planet Earth* Elsevier Science & Technology.

Merritt, M. 2004. *Estimating Hydraulic Properties of the Floridan Aquifer System by Analysis of Earth-Tide, Ocean-Tide, and Barometric Effects, Collier and Hendry Counties, Florida*.

Murdoch, L.C., C.E. Freeman, L.N. Germanovich, C. Thrash, and S. DeWolf. 2015. "Using in Situ Vertical Displacements to Characterize Changes in Moisture Load." *Water Resources Research* 51 (8): 5998-6016.

Murdoch, L.C., J.R. Richardson, C. Fairbanks, S.C. Malin, and Q.Tan. 2006. "Forms and Sand Transport in Shallow Hydraulic Fractures in Residual Soil." *Canadian Geotechnical Journal* 43 (10): 1061-1073.

Neuman, S.P. 1974. "Effect of Partial Penetration on Flow in Unconfined Aquifers Considering Delayed Gravity Response." *Water Resources Research* 10 (2): 303-312.

NOAA. "Where is the Highest Tide?", https://oceanservice.noaa.gov/facts/highesttide.html.

Rasmussen, T., K. Haborak, and M. Young. 2003a. "Estimating Aquifer Hydraulic Properties using Sinusoidal Pumping at the Savannah River Site, South Carolina, USA." *Hydrogeology Journal* 11 (4): 466-482.

Rasmussen, T., K. Haborak, and M. Young. 2003b. "Estimating Aquifer Hydraulic Properties using Sinusoidal Pumping at the Savannah River Site, South Carolina, USA." *Hydrogeology Journal* 11 (4): 466-482.

Riley, F. 1987. "Developments in Borehole Extensometry." *International Journal of Rock Mechanics and Mining Sciences & Geomechanics Abstracts* 24 (5): 169-186.

Robson, S. G. and E. R. Banta. 1970. "Determination of Specific Storage." *Ground Water* 28: 686-674.

Rojstaczer, S. 1988a. "Determination of Fluid Flow Properties from the Response of Water Levels in Wells to Atmospheric Loading." *Water Resources Research* 24 (11): 1927-1938.

Rojstaczer, S. 1988b. "Intermediate Period Response of Water Levels in Wells to Crustal Strain: Sensitivity and Noise Level." *Journal of Geophysical Research: Solid Earth* 93 (B11): 13619-13634.

Rojstaczer, S. and D. Carr Agnew. 1989. "The Influence of Formation Material Properties on the Response of Water Levels in Wells to Earth Tides and Atmospheric Loading." *Journal of Geophysical Research* 94 (B9): 12403-12411.

Rotzoll, K., A. El-Kadi, and S. B. Gingerich. 2008. "Analysis of an Unconfined Aquifer Subject to Asynchronous Dual-Tide Propagation." *Ground Water* 46 (2): 239-250.

Soil Survey Staff. *Web Soil Survey* Natural Resources Conservation Service, United States Department of Agriculture.

Sun, A.Y., J. Lu, and S. Hovorka. 2015. "A Harmonic Pulse Testing Method for Leakage Detection in Deep Subsurface Storage Formations." *Water Resources Research* 51 (6): 4263-4281.

Van Der Kamp, G. and J. E. Gale. 1983. "Theory of Earth Tide and Barometric Effects in Porous Formations with Compressible Grains." *Water Resources Research* 19 (2): 538-544.

Vandenberg, A. 1976. *Tables and Type Curves for Analysis of Pump Tests in Leaky Parallel-Channel Aquifers.* Ottawa: Environment Canada, Inland Waters Directorate, Water Resources Branch.

Vandenberg, A. 1977. "Type Curves for Analysis of Pump Tests in Leaky Strip Aquifers." *Journal of Hydrology* 33 (1): 15-26.

Wang, H.F. 2000. *Theory of Linear Poroelasticity with Applications to Geomechanics and Hydrogeology* Princeton University Press.